AD-A217 882

Annual Technical Report #2
November 1, 1988 - November 1, 1989

ANALYSIS OF FLOW-,
THERMAL-, AND STRUCTURAL-INTERACTION
OF
HYPERSONIC STRUCTURES
SUBJECTED TO SEVERE AERODYNAMIC
HEATING

Contract #F49620-C-88-0001

Air Force Office of Scientific Research
Building 410
Bolling Air Force Base, DC 20332-6448

TR-89-15

DTIC
ELECTE
FEB 07 1990
S B D

THE COMPUTATIONAL MECHANICS CO., INC.
3701 North Lamar, Suite 201
Austin, Texas 78705
(512) 467-0618

THE COMPUTATIONAL MECHANICS COMPANY, INC.

90 02 06 121

UNCLASSIFIED
SECURITY CLASSIFICATION OF THIS PAGE

REPORT DOCUMENTATION PAGE

Form Approved
OMB No. 0704-0188

1a. REPORT SECURITY CLASSIFICATION	1b. RESTRICTIVE MARKINGS
UNCLASSIFIED	

2a. SECURITY CLASSIFICATION AUTHORITY	3. DISTRIBUTION / AVAILABILITY OF REPORT
2b. DECLASSIFICATION / DOWNGRADING SCHEDULE	Unlimited

4. PERFORMING ORGANIZATION REPORT NUMBER(S)	5. MONITORING ORGANIZATION REPORT NUMBER(S)
	AFOSR·TR· 90-0050

6a. NAME OF PERFORMING ORGANIZATION	6b. OFFICE SYMBOL (If applicable)	7a. NAME OF MONITORING ORGANIZATION
The Computational Mechanics Company, Inc.		AFOSR

6c. ADDRESS (City, State, and ZIP Code)	7b. ADDRESS (City, State, and ZIP Code)
3701 North Lamar, Suite 201 Austin, Texas 78705	AFOSR/NA Bldg 410 Bolling AFB DC 20332-6448

8a. NAME OF FUNDING/SPONSORING ORGANIZATION USAF, AFSC, Air Force Ofc of Scientific Research	8b. OFFICE SYMBOL (If applicable) NA	9. PROCUREMENT INSTRUMENT IDENTIFICATION NUMBER F49620-88-C-0001

8c. ADDRESS (City, State, and ZIP Code)	10. SOURCE OF FUNDING NUMBERS			
AFOSR/NA Bldg 410 Bolling AFB DC 20332-6448	PROGRAM ELEMENT NO. 61102F	PROJECT NO. 2302	TASK NO. B1	WORK UNIT ACCESSION NO.

11. TITLE (Include Security Classification)
Analysis of Flow-, Thermal-, and Structural-Interaction of Hypersonic Structures (U) Subjected to Severe Aerodynamic Heating

12. PERSONAL AUTHOR(S)

13a. TYPE OF REPORT	13b. TIME COVERED	14. DATE OF REPORT (Year, Month, Day)	15. PAGE COUNT
Annual/Final Report	FROM 11-1-88 TO 10-31-89	89-Nov-30	105

16. SUPPLEMENTARY NOTATION
UNCLASSIFIED

17. COSATI CODES			18. SUBJECT TERMS (Continue on reverse if necessary and identify by block number)
FIELD	GROUP	SUB-GROUP	Hypersonic flight, viscous compressible flow, adaptive methods, damage modeling, implicit/explicit solvers, large deformations.

19. ABSTRACT (Continue on reverse if necessary and identify by block number)

Over the past two years a unique collection of algorithms have been developed for the analysis of hypersonic structures subjected to severe aerodynamic heating. These algorithms employ adaptive computational methods to resolve many of the complex structural and flow features such as nonelastic, large, time-dependent structural deformations, shock interaction boundary layers and shock interactions. Local error estimates were used to evaluate the quality of the computed solutions and subsequently optimize the structure of the grids to deliver a specified level of accuracy with a minimum of computational effort. In addition, implicit/explicit solution algorithms for the fluid modeling were employed which exploit the speed and simplicity of explicit methods and the stability of implicit methods. Zoning techniques for automatically selecting the implicit and explicit zones were studied with optimization of the computational effort as the central goal. The modeling of the structural problems incorporated a version of the Bodner-Partom constitutive model for time-dependent viscoplastic materials. During the course of this study this model was extended to include a damage parameter which was treated as an additional internal state variable. A number of validation cases were run to test the various components of the package and prepare for the experimental verification which was planned for year three.

20. DISTRIBUTION / AVAILABILITY OF ABSTRACT	21. ABSTRACT SECURITY CLASSIFICATION
☒ UNCLASSIFIED/UNLIMITED ☐ SAME AS RPT. ☐ DTIC USERS	UNCLASSIFIED

22a. NAME OF RESPONSIBLE INDIVIDUAL Dr. Spencer T. Wu	22b. TELEPHONE (Include Area Code) (202)767-6962	22c. OFFICE SYMBOL NA

DD Form 1473, JUN 86   Previous editions are obsolete.   SECURITY CLASSIFICATION OF THIS PAGE

UNCLASSIFIED

Contents

1 Introduction

An effort aimed at improving the quality of the numerical analysis of complex flow-thermal-structural interactions in hypersonic flight was motivated by a recent surge of interest in developing new supersonic and hypersonic vehicles (as in the National Aerospace Plane (NASP)). Such structures, in particular their leading edges and points of shock impingement, are exposed to hostile aero-thermomechanical loads with resulting elevated temperatures. Even when equipped with active cooling systems, they can reach temperatures close to the melting point. For a designer, these structures present a significant challenge because of the inherent nonlinearities in all aspects of the multidisiplinary analysis. Some of the critical computational issues, identified in Ref. [8], include the difficulties associated with: (1) analyzing the viscous, compressible flow and predicting the high local aerodynamic heating, (2) modeling and analyzing of multimode unsteady heat transfer in a high temperature convectively-cooled structure, and (3) simulating the transient, nonlinear thermal-structural response to rapid temperature changes.

The general objective of this project was to make further progress toward a realistic analysis and design of hypersonic structures. The effort was threefold:

- identification of the major physical phenomena involved in flow-thermal-structural interactions in hypersonic flight.

- development of computational methods and techniques necessary for reliable modeling and analysis of these phenomena, and

- solution of examples of hypersonic structures subjected to severe aerothermal loads due to fluid-thermal-structural interactions.

In the course of this project significant progress has been made in all these areas and the results are presented in this report. A general summary of the research progress is summarized in Section 2. A theoretical formulation and finite element approach for the solution of transient thermal problem is presented in Section 3. This section is followed by a finite element formulation of the thermo-viscoplastic structural analysis with large displacements (Section 4). In Section 5 a derivation and finite element formulation of a new implicit/explicit Taylor-Galerkin method for the solution of compressible flow and the prediction of aerothermal loads is presented. In Section 6 several validation and test examples for thermo-structural and flow analyses are solved. Finally, in Section 7, a more realistic thermo-viscoplastic analysis of a segment of the scramjet strut is presented. This section is followed by conclusions and final remarks.

2 Summary of Research Progress

The work in the project has focused on the physical phenomena, mathematical formulations and computational methods needed to solve fluid-thermal-structural interactions in hypersonic flight. Toward this end, unique computational capabilities and finite element software have been developed.

The flow-thermal-structure (FTS) interaction problem considered here is shown in Figs. 1 and 2. Figure 2a shows a low temperature, undeformed elastic structure subjected to a low-level, uniform, aerodynamic heating. In this state, there is little FTS interaction. In contrast, Fig. 2b shows a structure that is subjected to intense localized heating characteristic of shock interactions. There is a local, growing region of very high temperatures and plastically deforming material. As the plastic region grows, the surface deforms into the flow producing flow recirculation. The flow recirculation intensifies local heating, skin friction, and surface pressure. As the heating increases, the temperature continues to grow and can eventually reach the melting temperature.

Toward a realistic analysis of the above FTS interaction problem the following objectives have been accomplished:

1. Basic phenomena essential in the analysis of these problems have been identified. For these phenomena, mathematical models have been formulated, assuming that:

   (a) The unsteady heat transfer problem is described by conservation of energy neglecting mechanical coupling terms. This assumption is known to be reasonable for the materials, deformation rates and applied heat loads encountered in hypersonic structures. Nonlinear heat transfer due to temperature dependent material properties such as specific heat and thermal conductivity are included as well as surface radiation.

   (b) The structural problem is assumed to be quasi-static and viscoplastic with large-deformation kinematics. The application of a viscoplastic constitutive model is necessary because of the extremely high temperatures enocuntered in hypersonic structures. The particular constitutive theory applied is known as the Bodner-Partom unified viscoplastic theory [4]. This theory has been validated for high-temperature alloys under the NASA HOST program [5,6]. An extension of this theory for nonlinear, large displacement kinematics was necessary in order to capture beam-column effects occurring due to localized heating (see Section 7).

   (c) The external flow problem is governed by the Navier-Stokes equations for a compressible, viscous flow of a calorically perfect gas. This assumption is legitimate for supersonic and hypersonic flows where the Mach number is less than approx-

imately eight. For higher Mach numbers, when the gas temperature is 2500 K or higher, the specific heat becomes temperature and pressure dependent and the air becomes chemically reactive.

2. Computational methods and finite element software have been developed for the analysis of flow-thermal-structural interaction problems described by appropriate mathematical models, in particular:

   (a) A family of finite element heat transfer programs has been placed into operation. These programs solve nonlinear, steady or transient heat transfer problems, taking into account:

   - conduction with temperature-dependent properties
   - surface convection
   - convective cooling (active cooling systems)
   - radiation

   (b) A two-dimensional finite element thermo-viscoplastic structural analysis program has been developed. The program is coupled with the thermal analysis software and performs a nonlinear, transient solution of structural deformation problems, taking into account:

   - visco-elastoplastic material models with temperature-dependent properties
   - large displacement kinematics (to capture beam-column effects due to localized heating)
   - development of continuum damage in the material (to predict structural failure)

   The above viscoplastic problems result in a set of nonlinear, " stiff" evolution equations. In order to provide a reliable, efficient solution for these problems, the finite element software was equipped with an error estimator and an adaptive time stepping procedure which enables precise control of the solution error.

   (c) A new, implicit/explicit method for the compressible Navier-Stokes equations was formulated and implemented in the adaptive finite element program. The method was developed for the prediction of aerothermal loads on hypersonic structures. The development of a new implicit/explicit method was motivated by our numerical experiments and the experience of other researchers that:

   - Explicit solvers are inefficient in the solution of viscous supersonic flows due to time step stability limitations and slow convergence of the heating rates.
   - Fully implicit solvers, while being more stable and reliable than explicit algorithms, require large computational times due to expensive element matrix evaluations and solution of linear system of equations.

3

The new implicit/explicit method developed in the project adaptively selects implicit and explicit computational subdomains to provide stability of the implicit methods while at the same time minimizing the cost of the computations.

(d) Numerical solutions of a variety of problems have been performed. These problems include:

- relatively simple test problems, designed to verify methods and procedures and compare results with existing experimental evidence and analytical solutions, and

- more realistic interaction problems, simulating the behavior of aerospace structures under severe aerothermal loads in hypersonic flight.

It should be noted that the major effort in the first two years of the project was oriented toward identification of physical phenomena in hypersonic interactions, development of corresponding mathematical models, and computational procedures and their numerical verification. Thus, the number of realistic examples solved in this phase is rather small. More extensive computations, combined with experimental verification, was planned for the third year of the project.

Papers and Presentations

The research performed in the project and the corresponding results were presented at the AIAA/ASME/ASCE/AMS 30th Structures, Structural Dynamics and Materials Conference in Mobile, Alabama in April 1989 (Ref. [33]). The corresponding paper was accepted for publication in the AIAA Journal in 1989, Ref. [35]. Further papers and presentations are in preparation.

3 Thermal Analysis of Hypersonic Structures

Convectively cooled structures are strong candidates for use as hypersonic flight vehicles. For hypersonic flight, some leading edges and panels require active cooling systems to keep the structural temperature within acceptable ranges. The internal flow in the coolant passage pla. a predominant role in the thermal response of a hypersonic structure subject to external heating. A cross-section of a typical convectively cooled structure is shown in Fig. 3. An aerodynamic skin and coolant passage with an internal heat exchanger protect the primary structure from the aerodynamic heating. The thin, typically metallic, aerodynamic skin transfers the energy from the aerodynamic heating to a low temperature coolant flow through the heat exchanger fins that connect the aerodynamic skin to the primary structure. In a

typical engine structure, the coolant is cold hydrogen that later is used as the propulsion system fuel.

Heat transfer in the aerodynamic skin consists of conduction combined with surface radiation. Heat transfer between the aerodynamic skin, the heat exchanger surfaces and the primary structure is by conduction at the solid–fluid interface. The dominant mode of heat transfer in the coolant flow is forced convection.

An accurate representation of the heat transfer in the coolant passage is the critical step in the heat transfer analysis. There are two basic representations that can be employed. The first, denoted here as the engineering model, is based upon a number of assumptions that greatly simplify the problem into a single energy equation with a specified mass flow rate. Detailed computations of the fluid velocity components and temperature is not required. The second representation idealizes the coolant flow as a continuum model, and the partial differential equations describing conservation of mass, momentum and energy are solved simultaneously to obtain fluid velocity and temperature distributions. This latter model is the most accurate, but it is also considerably more expensive than the engineering model. As a first step towards understanding flow-thermal-structural interactions characteristic of hypersonic structures the engineering heat transfer model is employed.

3.1   Engineering Model for Coolant Passages

The basic features of the engineering model can be developed from the idealization shown in Fig. 4. A segment of the coolant passage of width w is shown; for simplicity, only the upper one-half of the coolant passage with the aerodynamic skin is shown. The engineering formulation (Ref. [34]) is based on the following assumptions:

1. The thermal energy state of the fluid is characterized by the fluid bulk temperature T_F which varies only in the flow direction, i.e. $T_F(x,t)$.

2. The flow is represented by the mass flow rate $\dot{m}$ in the coolant passage specified by $\dot{m} = \rho_F A_F V_F$ where ρ_F is the coolant density, A_F is the cross-sectional area of the coolant passage, and V_F is the coolant mean flow velocity.

3. A convection coefficient h is defined such that the heat flux $\dot{q}_F$ transferred between the structure and the coolant may be expressed as

$$\dot{q} = h(T_S - T_F)$$

where $T_S(x,t)$ denotes the structural temperature at the fluid–solid interface.

5

4. The convection coefficient h may be expressed as a function of the fluid bulk temperature alone by using the analytical/empirical equation for the Nusselt number,

$$Nu = \frac{hD}{k_F}$$

where D is the hydraulic diameter of the coolant passage, and k_F is the thermal conductivity of the fluid coolant. The convection coefficient as well as the solid and fluid thermal parameters may, in general, be temperature dependent.

With these assumptions, energy balances on the aerodynamic skin and coolant give the governing conservation equations.

Fluid:

$$-\frac{\partial}{\partial x}(k_F A_F \frac{\partial T_F}{\partial x}) + \dot{m}c_F \frac{\partial T_F}{\partial x} - wh(T_S - T_F) + \rho_F c_F A_F \frac{\partial T_F}{\partial t} = 0 \qquad (3.1)$$

Solid:

$$-\frac{\partial}{\partial x}(k_S A_S \frac{\partial T_S}{\partial x}) + wh(T_S - T_F) + \sigma \epsilon T^4 + \rho_S c_S A_S \frac{\partial T_S}{\partial t} = \dot{q} \qquad (3.2)$$

where the subscripts F and S denote the fluid and solid, respectively. In these equations, c denotes specific heat, σ is the Stefan-Boltzmann constant, and ϵ is the surface emissivity. Because of the temperature dependence of the thermal parameters and the radiation term, Eqs. (3.1) and (3.2) constitute a nonlinear set of partial differential equations.

The heat exchanger fins are not included explicitly in this model. However, the heat transfer between the heat exchanger fins can approximately be taken into consideration though the use of an effective width w which represents the area over which the convective heat exchange occurs.

3.2 Finite Element Formulation

A typical finite element representing Eqs. (3.1) and (3.2) is characterized by fluid and fluid-solid interface nodes. The element shown in Fig. 5 has two fluid nodes (I and J), and two fluid–solid interface nodes. Within the element, the fluid and solid temperatures are express as

$$T_F = [N(x)]\{T_F\}$$

$$T_S = [N(x)]\{T_S\} \qquad (3.3)$$

where $[N(x)]$ are the element interpolation functions. Following usual finite element procedures (Ref. [34]), the discritized equations for an element of length L may be derived in the

6

form

$$\begin{bmatrix} C_F & 0 \\ 0 & C_S \end{bmatrix} \left\{ \begin{array}{c} \dot{T}_F \\ \dot{T}_S \end{array} \right\} + \begin{bmatrix} K_v + K_h + K_F & -K_h \\ -K_h & K_S + K_R \end{bmatrix} \left\{ \begin{array}{c} T_F \\ T_S \end{array} \right\} = \left\{ \begin{array}{c} 0 \\ Q \end{array} \right\} \qquad (3.4)$$

where the element capacitance matrices are given by

$$[C_F] = \int_0^L \rho_F c_F A_F \{N\}[N] dx$$

$$[C_S] = \int_0^L \rho_S c_S A_S \{N\}[N] dx \qquad (3.5)$$

and the element conductance matrices are

$$[K_v] = \int_0^L \dot{m} c_F \{N\} [\frac{dN}{dx}] dx$$

$$[K_h] = \int_0^L w h \{N\}[N] dx$$

$$[K_F] = \int_0^L k_F A_F \left\{ \frac{dN}{dx} \right\} \left[\frac{dN}{dx} \right] dx \qquad (3.6)$$

$$[K_S] = \int_0^L k_S A_S \left\{ \frac{dN}{dx} \right\} \left[\frac{dN}{dx} \right] dx$$

$$[K_R]\{T_S\} = \int_0^L \sigma \epsilon T^4 \{N\} dx$$

The element equations given in Eqs. (3.4) show that the coolant passage model can be regarded as an assembly of elements where each element represents a single heat transfer mode. Thus we can represent the coolant passage in terms of two convective elements: (1) a mass-transport element (Fig. 6a). and (2) a surface convection element (Fig. 6b). The mass transport element represents the downstream convective heat transfer due to mass flow: it has a capacitance matrix $[C_F]$ as well as conductance matrices $[K_v]$ and $[K_F]$. The surface convection element represents the convection heat exchange between the coolant fluid and the solid: it does not have a capacitance matrix, but it has a conductance matrix $[K_h]$ linking the solid and fluid nodes. These coolant passage elements are assembled into the finite element thermal model for the complete convectively cooled structure that has conduction elements. radiation elements. and surface elements for convection to a specified convective exchange temperature.

The unsteady thermal analysis is nonlinear because of the temperature dependent thermal properties and surface radiation. The equations are solved by time marching with the Crank-Nicolson algorithm: at each time step, the nonlinear algebraic equations are solved using Newton-Raphson iteration.

7

4 Thermo–Viscoplastic Structural Analysis

In this section we will present a new, extended formulation of the thermo–viscoplastic finite element structural analysis. Extensions of the theory compared with our previous reports include:

- Generalization of the formulation for the case of large displacements.

- Incorporation of a model of material damage in the constitutive equations.

The extension of the theory to the case of large displacements was motivated by the analysis of a convectively cooled structure presented in Refs. [33,35]. In this analysis, which simulated the failure of heat exchanger fins, the aerodynamic skin experienced relatively large displacements. Modeling of these displacements and the occurrence of a nonlinear beam–column type effect motivated our effort to extend the theory to large deformations.

The particular version of the large deformation theory applied here can be classified as a large displacement–small strain theory. The limitation to small strains results primarily from the fact that the elasto–viscoplastic Bodner-Partom constitutive equations were not devised and validated for stretch levels exceeding a few percent (say five percent). Thus it is reasonable to limit our theory and applications to small strains.

The incorporation of a *material damage model in the constitutive equations* allows for a more complete analysis of the structure and prediction of structural failure due to extensive loads and/or multiple load cycles. The model presented here is based on the work of Bodner and Chan (Ref. [4]) and is consistent with the Bodner-Partom model of elasto–viscoplasticity.

4.1 Large Displacement–Small Strain Kinematics

4.1.1 Strain and Stress Measures

In this section we present the basic kinematic relations for the theory of large deformations and the implications of the restriction to the small strain case.

We are interested in the deformation of a metrical continuum, which at a certain initial time $t = 0$ occupies an initial configuration B_0, which is formally identified with the reference configuration B_R. The reference configuration is parametrized by the reference Cartesian coordinate system $\{X_K\}$ with base $I_K, K = 1, 2$ (see Fig. 7).

The reference coordinates X_I identify particles of a continuum in the sense that by particle X we mean the particle, which in the reference configuration has a position defined by vector X.

At an arbitrary time $t > 0$ the continuum occupies a deformed configuration B_t, with new positions of particles referred to the Cartesian coordinate system $\{x_k\}$ with base i_k. $k = 1, 2$. It is convenient, without restricting the generality of the description, to identify coordinate systems $\{x_k\}$ and $\{X_K\}$ (see Fig. 7). The notion of systems $\{X_k\}$ and $\{x_k\}$ represents a typical notation convention of large deformation kinematics (see references [15.23.36] in which *uppercase symbols and indices refer to the reference configuration, while lowercase symbols and indices refer to the current configuration.*

Moreover, in general curvilinear coordinate systems, superscripts denote contravariant components and subscripts denote covariant components of vectors or tensors. However, in our case both coordinate systems $\{X_I\}$ and $\{x_i\}$ are Cartesian, so there is no difference between covariant and contravariant coordinates, and thus only subscripts will be used throughout this work.

Motion of the continuum is described by the relation

$$x_i = x_i(X_I, t) \qquad t \geq 0 \tag{4.1}$$

and the information about local deformation in the neighborhood of a particle X is presented by the deformation gradient tensor F with components:

$$F_{iJ} = x_{i,J}$$

where a comma denotes partial differentation.

To indicate clearly implications of the restriction to small strain analysis, it is useful to apply the polar decomposition theorem (see e.g., references [15.23.36]), according to which the deformation gradient tensor F can be decomposed as:

$$F = RU$$

where U is the right stretch tensor (symmetric, positive definite) and R is a rotation tensor.

The above equation implies that the general deformation can be viewed as a two–stage process

$$F = F^{(2)}F^{(1)}$$

with the first stage being stretch (generally arbitrarily large), and the second stage being the rigid rotation. Within our theory we will limit the analysis to the case when $F^{(1)} = U$ represents infinitesimal deformation, while the rigid rotation $F^{(2)} = R$ is arbitrarily large. From the above we conclude, by standard arguments of the infinitesimal theory, that at the first stage the stress and strain measures corresponding to the large deformation theory and the infinitesimal theory can be identified

$$E_{IJ} = e_{ij} = \epsilon_{ij}$$

$$T_{IJ} = t_{ij} = \sigma_{ij}$$

$$\tag{4.2}$$

9

In the above, E_{IJ} and e_{ij} are the components of the Green and Cauchy strain tensor, respectively, T_{IJ} and t_{ij} are the components of the second Piola-Kirchhoff and Cauchy stress tensors, respectively, and $\epsilon_{ij}, \sigma_{ij}$ are generic symbols of strain and stress in the infinitesimal theory.

Equation (4.2) suggests that at the first stage of deformation the constitutive equations can equivalently be applied to the components T_{IJ}, E_{IJ} as well as to t_{ij}, e_{ij}.

With regard to the second stage of deformation $F^{(2)} = R$, it can be easily verified that it changes components t_{ij} and e_{ij}, but components T_{IJ} and E_{IJ} are invariant under rotation and they still represent the infinitesimal stretch of the first stage $F^{(1)} = U$ (but now material fibers are rotated). Thus, for the combined deformation $F = F^{(2)} F^{(1)}$, we can use the elasto–viscoplastic constitutive equations expressed in terms of T_{IJ}, E_{IJ}. This will guarantee satisfaction of the observer independence condition, while still allowing for the application of the small strain constitutive equations.

Note, however, that for this total deformation the components of the strain tensor must be expressed by the fully nonlinear formula

$$E_{ij} = \frac{1}{2}(u_{i,J} + u_{j,I} + u_{k,I}\, u_{k,J}) \qquad i = I, j = J \tag{4.3}$$

One of the consequences of the small strain assumption is that

$$\det U \approx 1 \tag{4.4}$$

which, by properties of the rotation tensor, gives

$$\det F = \det R \, \det U \approx 1 \tag{4.5}$$

4.1.2 Interpretation of Strain and Stress Measures

The important issue in practical computations is the physical interpretaion of strain and stress measures. Although the reference measures T_{IJ} and E_{IJ} have, in general, no straightforward physical meaning, it can be shown that in our case they actually have a clear interpretation.

From the equation (4.2) valid for the stage $F^{(1)} = U$ (infinitesimal) and the invariance of tensor E under rotation $F^{(2)} = R$ we can easily conclude that components E_{IJ} retain a typical interpretation of the infinitesimal theory. In particular, E_{II} represents the relative stretch of material fibers which were originally parallel to axis X_I :

$$E_{II} = \frac{l_I - L_I}{L_I}$$

10

while E_{IJ}, with $I \neq J$, represents half of the change of the angle between such fibers. Note however, that these fibers undergo a large rotation (see Fig. 7). To present an interpretation of the components of the Second Piola-Kirchhoff stress tensor T_{IJ}, let us introduce the convected coordinate system $\{\theta_I\}$, which at the initial time $t = 0$ is identified with the reference system $\{X_I\}$, and at further stages of motion deforms with the body, so that coordinates of material particles in this system remain unchanged

$$\theta_I(X,t) = \theta_I(X,0) = X_I(X)$$

The convected coordinate system is, in general, curvilinear and its basis vectors are denoted by g_I, $I = 1,2$. The components t_{ij} of a Cauchy or "real" stress tensor in the Cartesian coordinate system $\{x_i\}$ are expressed via its components t_{ij} in $\{\theta_I\}$ by the transformation law (since $\{\theta_I\}$ is curvilinear, we will temporarily distinguish covariant and contravariant components of tensors):

$$
\begin{aligned}
t_{ij} &= t^{ij} = \frac{\partial x_i}{\partial \theta_I}\frac{\partial x_j}{\partial \theta_J}t^{IJ} \\
&= \frac{\partial x_i}{\partial X_I}\frac{\partial x_j}{\partial X_J}t^{IJ}
\end{aligned}
\tag{4.6}
$$

where differentiation $\partial x_i/\partial X_I$ is understood with reference to relation (4.1).

On the other hand, the relation between Cauchy and the second Piola-Kirchhoff stress tensors is by definition

$$t_{ij} = t^{ij} = (\det F)^{-1}\frac{\partial x_i}{\partial X_I}\frac{\partial x_i}{\partial X_j}T^{IJ} \tag{4.7}$$

By comparison of formulas (4.6) and (4.7), and recalling equation (4.5) we obtain the simple relation

$$T^{IJ} = t^{IJ}.$$

If we recall that the system $\{X_I\}$ is orthonormal we can also write:

$$T_{IJ} = t^{IJ}.$$

This means that in the case under consideration the components of the second Piola-Kirchhoff stress tensor can be interpreted as the components of the Cauchy stress tensor ("real" stress) presented in the base of the convected coordinate system $\{\theta_K\}$ (see Fig. 7).

4.2 Elasto–Viscoplastic Constitutive Model With Damage and Temperature Effects

We now describe the Bodner-Partom constitutive equations used in the thermo–viscoplastic analysis. The version of the equations presented describes nonelastic behavior of materials including

11

- viscoplastic effects,

- temperature–dependent properties,

- development of internal damage in the material

When combined with the strain and stress measures introduced in the previous section, these equations are applicable in the large displacement–small strain theory.

It is important to note that while we will be using large deformation strain and stress measures E_{IJ} and T_{IJ} in the following developments, the form of constitutive equations is exactly the same as in infinitesimal theory, and it is not applicable at large stretch levels. Although one can formally perform computations at large strain levels, the results would most probably be inadequate for modeling real physical phenomena.

The elastic–viscoplastic analysis with temperature effects is based on decomposition of strain rates

$$\dot{E}_{IJ} = E_{IJ}^{(e)} + E_{IJ}^{(n)} \tag{4.8}$$

where superscripts (e) and (n) denote elastic and nonelastic strain components, respectively. The total strain rates are expressed in terms of displacement rates as

$$\dot{E}_{IJ} = \frac{1}{2}(\dot{u}_{i,J} + \dot{u}_{j,I} + \dot{u}_{k,I}u_{k,J} + u_{k,I}\dot{u}_{k,J}) \qquad i = J, j = J$$

and the constitutive relations for the elastic part are

$$\dot{T}_{IJ} = \mathcal{C}_{IJKL}\dot{E}_{KL} - \mathcal{C}_{IJKL}\mathcal{L}_{KL}\dot{T} \tag{4.9}$$

where $\mathcal{C}$ is the Hooke's tensor of elasticity parameters, $\mathcal{L}$ is a tensor of thermal expansion and $\dot{T}$ represents the rate of the change in temperature. Both $\mathcal{C}$ and $\mathcal{L}$ are temperature dependent.

A nonelastic deformation is governed by the flow rule:

$$\dot{E}_{IJ}^{(n)} = f_{IJ}(T_{IJ}, Z_k, \omega_k)$$

$$\dot{Z}_i = g_i(T_{IJ}, Z_k)$$

$$\dot{\omega}_i = h_i(T_{IJ}, \omega_i)$$

where f_{IJ}, g_i and h_i are constitutive functions, Z_i are internal state variables, and W_i are damage variables. These functions and state variables characterize the viscoplastic response of the material with continuum damage effects.

12

In the particular version of the Bodner-Partom theory applied in this work, the nonelastic flow rule is of the form:

$$\dot{E}_{IJ}^{(n)} = \lambda S_{IJ} \quad , \quad \lambda > 0$$

$$E_{KK}^{(n)} = 0$$

where S_{IJ} are the deviatoric components of a stress tensor

$$S_{IJ} = T_{IJ} - \frac{1}{3}T_{IJ}\delta_{IJ}$$

The current value of parameter λ is given by

$$\lambda^2 = \frac{1}{J_2}D_0^2 \exp\left[-\left(\frac{Z^2(1-\omega^2)}{3J_2}\right)^n\right]$$

where J_2 is the second invariant of a deviatoric stress tensor

$$J_2 = \frac{1}{2}S_{IJ}S_{IJ}$$

D_0 is a limiting strain rate in shear, n is a material constant and Z and ω are state variables which evolve during deformation. In particular, Z is the hardness variable, which represents viscoplastic hardening (or softening) of a material. The new variable ω not present in the previous versions of the Bodner-Partom equations, is the damage variable. This variable represents weakening of the material due to nucleation and propagation of microscopic voids and cracks in the material. The variable ω evolves from 0 to 1, where a value $\omega = 1$ represents total loss of the strength of the material.

In the framework of materials science the value of ω is usually interpreted as ratio of the area of voids to the total area of a certain cross section of a sample:

$$\omega = \frac{A_{\text{void}}}{A}$$

The state variables Z and ω evolve according to the specific equations of the viscoplastic theory:

1. Evolution equations of hardness variable

The internal state variable Z consists of isotropic and directional components.

$$Z = Z^I + Z^D$$

The evolution equation proposed for the isotropic hardening component (Refs. [33,35]) is

$$\dot{Z}^I(t) = m_1[Z_1 - Z_I(t)]\dot{W}_p(t) - A_1 Z_1\left[\frac{Z^I(t) - Z_2}{Z_1}\right]^{r_1} \tag{4.10}$$

13

with the initial condition, $Z^I(0) = Z_0$. In the first term, Z_1 is the limiting (saturation) value of Z^I, m_1 is the hardening rate, and the plastic work rate is

$$\dot{W}_p = T_{IJ}\dot{E}^{(p)}_{IJ}$$

which is taken as the measure of hardening. Z_2 is the minimum value of Z^I at a given temperature, and A_1 and r_1 are temperature dependent material constants. The evolution form of the directional hardening component (Refs. [33,35]) is defined as

$$Z^D(t) = \beta_{IJ}(t)u_{IJ}(t)$$

where u_{IJ} are the direction cosines of the current stress state.

$$u_{IJ}(t) = T_{IJ}(t)/[T_{KL}T_{KL}]^{\frac{1}{2}} \qquad (4.11)$$

The evolution equation for $\beta_{IJ}(t)$ has the same general form as that for isotropic hardening but has tensorial character.

$$\dot{\beta}_{IJ} = m_2[Z_3 u_{IJ}(t) - \beta_{IJ}(t)]\dot{W}_p(t)$$

$$- A_2 Z_1 \left\{ \frac{[\beta_{KL}(t)\beta_{KL}(t)]^{\frac{1}{2}}}{Z_1} \right\}^{r_2} v_{IJ}(t)$$

where

$$v_{IJ}(t) = \beta_{IJ}(t)/[\beta_{KL}(t)\beta_{KL}(t)]^{\frac{1}{2}}$$

and

$$\beta_{IJ}(0) = 0$$

As in Eq. (4.10), m^2 is the hardening rate. A_2 and r_2 are temperature dependent material constants.

2. Evolution of damage

The damage parameter consists, in general, of isotropic and directional components.

$$\omega = \omega^I + \omega^D$$

The evolution of isotropic damage proposed in reference [4] is of the form

$$\dot{\omega}^I = \frac{P}{H} \left\{ \left[ln\left(\frac{1}{\omega^I}\right) \right]^{\frac{p+1}{p}} \right\} \omega^I Q \qquad (4.12)$$

In the above p and H are material constants (temperature dependent), Q is the stress intensity function, given by

$$Q = \left[A\sigma^+_{max} + B\sqrt{3J_2} + C I^+_1 \right]^\nu$$

14

where σ_{max}^+ is the maximum principal tensile stress, I_1^+ is the first stress invariant (nonnegative) and J_2 is the previously introduced second invariant of deviatoric stress.

A, B, D, and ν are material constants. A, B, C must satisfy the condition

$$A + B + C = 1$$

Clearly, the actual proportion of these constants selects the factor for stress state which is most important in the development of internal damage.

The initial condition for isotropic damage is $\omega^I(0) = 0$. In practical analyses the coefficient ν is of the order 10 (compare ref.[4]). Thus, when SI units are used in the analysis, the factor Q as well as the constant H reach extremely high values, beyond the limit of real number capacity on some computers. Thus, for numerical analysis, equation (4.12) was recast in the equivalent, but more convenient form:

$$\dot{\omega}^I = \dot{p} \left\{ \left[ln \left(\frac{1}{\omega^I} \right) \right]^{\frac{p+1}{p}} \right\} \left(\frac{\hat{Q}}{\hat{H}} \right)^\nu$$

where:

$$\hat{Q} = Q^{\frac{1}{\nu}} = A\sigma_{max}^+ + B\sqrt{3J_2} + CI_1^+$$

$$\hat{H} = (H \tfrac{1}{sec})^{\frac{1}{\nu}}$$

$$\dot{p} = p \cdot \tfrac{1}{sec}$$

The additional advantage of this formulation is that both $\hat{Q}$ and $\hat{H}$ are in the stress units (MP_a) instead of somewhat cumbersome $(MP_a)^\nu$. The directional damage is defined in a manner very similar to directional hardening, namely

$$\omega^D = \omega_{IJ}^D u_{IJ}$$

where u_{IJ} are directional cosines defined in equation (4.11) and the components of a tensor ω^D evolve according to equation

$$\dot{\omega}_{IJ}^D = \frac{q}{M} \left\{ \left[ln \left(\frac{1}{\omega^D} \right) \right]^{\frac{q+1}{q}} \right\} \omega^D Q u_{IJ}$$

where q and M are material constants. The initial condition is

$$\omega_{IJ}^D(0) = 0$$

Note that there are several problems with practical application of directional damage, reliability of the above model and conducting experiments relevant for the evolution of necessary

15

parameters. Even the extensive experiments presented in references [4,5,6] did not provide all the necessary data and, hence, the damage model was limited to the isotropic damage. Therefore, our numerical implementation and test computations were also limited to the isotropic damage.

4.3 Equations of Equilibrium and Boundary Conditions

The rate version of the equations of equilibrium formulated in the reference configuration is:

$$\text{Div } (\dot{\hat{T}}) + \dot{b}_o = 0 \tag{4.13}$$

where $\hat{T}$ is the first Piola Kirchhoff stress tensor. b_o is the body force per unit volume in the reference configuration. and a dot denotes time derivative.

After substituting the relation between the first and second Piola-Kirchhoff tensors the above equation becomes

$$\text{Div } (\dot{FT}) + \dot{b}_o = 0 \tag{4.14}$$

or in component form

$$(x_{i,K} T_{KJ})_{,J} + \dot{b}_{oi} = 0$$

The typical boundary conditions are prescribed rates of displacements:

$$\dot{u} = \dot{\overline{u}}(t) \qquad \text{in} \quad \partial\Omega_{R1} \times [0, T]$$

and prescribed rates of boundary tractions

$$\dot{T}N = \dot{t}_0(t) \qquad \text{on} \quad \partial\Omega_{R2} \times [0, T]$$

or in terms of the second Piola-Kirchhoff tensor

$$(\dot{FT})N = \dot{t}_0(t) \qquad \text{on} \quad \partial\Omega_{R2} \times [0, T] \tag{4.15}$$

In the above Ω_R is the domain corresponding to the reference configuration and N is the outward normal to $\partial\Omega_R$.

4.4 Weak Formulation

In order to obtain a weak formulation of the viscoplastic evolution problem let us introduce the space of test functions:

$$V = \left\{ v \in [W^{m,p}(\Omega_R)]^2, v = 0 \text{ a.e. on } \partial\Omega_{R1} \right\}$$

16

and the space of trial functions (displacement rates):

$$U = \{\dot{u} \in [W^{m,p}(\Omega_R)]^2, \dot{u} = \dot{\bar{u}} \text{ a.e. on } \partial\Omega_{R1}\}$$

where Ω_R is the domain occupied by the reference configuration and $W^{m,p}(\Omega_R)$ is the Sobolev space, where specific values of m and p depend upon the particular forms of constitutive equations.

Multiplying the equilibrium equation (4.14) by a test function and integrating over Ω_R we obtain the weak form of the rate equilibrium equations:

$$-\int_{\Omega_R} \text{Div}\,(\boldsymbol{FT})\cdot v dX = \int_{\Omega_R} \dot{\boldsymbol{b}}\cdot v dx \qquad \forall v \in V$$

The application of the divergence theorem to the left-hand side yields:

$$\int_{\Omega_R}(\boldsymbol{FT})\cdot(\boldsymbol{\nabla}v)dX = \int_{\Omega_R}\dot{\boldsymbol{b}}_0\cdot v dX + \int_{\partial\Omega_R}(\boldsymbol{FT})\boldsymbol{N}\cdot v dS$$

and, after evaluation of the time derivative on the left-hand side, we obtain:

$$\int_{\Omega_R}(\dot{\boldsymbol{F}}\boldsymbol{T})\cdot(\boldsymbol{\nabla}v)dX + \int_{\Omega_R}\dot{\boldsymbol{T}}\cdot(\boldsymbol{F}^T\boldsymbol{\nabla}v)dX = \int_{\Omega_R}\dot{\boldsymbol{b}}_{\circ}\cdot v dX + \int_{\partial\Omega_R}(\boldsymbol{FT})\boldsymbol{N}\cdot v dS$$

Now it is easy to show, using basic relations presented in references [15,23,36], that:

$$\dot{\boldsymbol{F}} = (\boldsymbol{I} + \boldsymbol{\nabla}u)^{\cdot} = \boldsymbol{\nabla}\dot{u}$$

and by symmetry of the stress tensor $\boldsymbol{T}$

$$\dot{\boldsymbol{T}}\cdot(\boldsymbol{F}^T\boldsymbol{\nabla}v) = \dot{\boldsymbol{T}}\cdot\delta E(\boldsymbol{u},v)$$

where E is the Green strain tensor introduced in Section 3.1.

Moreover, we have from equation (4.15)

$$(\boldsymbol{FT})\boldsymbol{N} = \dot{t}_{\circ} \qquad \text{on } \partial\Omega_{R2}$$

If we recall the decomposition of strain rates (4.8) and the elastic constitutive equations (4.9), then we arrive at the weak formulation of the evolution problem:

Find a displacement rate field $t \to \dot{u}(\boldsymbol{x},t) \in U$ such that

$$\int_{\Omega_R} \boldsymbol{\nabla}\dot{u}\boldsymbol{T}\cdot\boldsymbol{\nabla}v\,dX + \int_{\Omega_R}\mathcal{C}\dot{E}\cdot\delta E(\boldsymbol{u},v)\,dX$$

$$= \int_{\Omega_R}\mathcal{C}\dot{E}^{(n)}\cdot\delta E(\boldsymbol{u},v)\,dX + \int_{\Omega_R}\mathcal{C}\dot{E}^{(t)}\cdot\delta E(\boldsymbol{u},v)\,dX \qquad (4.16)$$

$$+ \int_{\Omega_R}\dot{\boldsymbol{b}}_{\circ}\cdot v\,dX + \int_{\partial\Omega_R}\dot{t}_{\circ}\cdot v\,dS \qquad \forall v \in V$$

17

With the index notation. this equation takes the form:

$$\int_{\Omega_R} \dot{u}_{i,K} T_{KJ} v_{i,J} \, dX + \int_{\Omega_R} C_{IJKL} \dot{E}_{KL} \delta E_{IJ} \, dX$$

$$\int_{\Omega_R} C_{IJKL} \dot{E}_{KL}^{(n)} \delta E_{IJ} \, dX \int_{\Omega_R} C_{IJKL} \dot{E}_{KL}^{(t)} \delta E_{IJ} \, dX \qquad (4.17)$$

$$+ \int_{\Omega_R} \dot{b}_{oi} v_i \, dX + \int_{\partial\Omega_R} \dot{t}_{oi} v_i \, dS \qquad \forall v_i \in V$$

Note that for the large displacement–small strains theory we have det $F \approx 1$. so that body forces and surface tractions can be referred to the area in the current configuration:

$$b_o = b \quad \text{in } \Omega$$

$$t_o = t \quad \text{on } \partial\Omega$$

4.5 Finite Element Formulation

A finite element approximation of a problem (4.16) is obtained by introducing

$$u_i^h(X) = \sum_{\Delta=1}^{N} u_{i\Delta} \Psi_\Delta(X)$$

$$v_i^h(X) = \sum_{\Delta=1}^{N} v_{i\Delta} \Psi_\Delta(X) \qquad (4.18)$$

$$\dot{u}_i^h(X) = \sum_{\Delta=1}^{N} \dot{u}_{i\Delta} \Psi_\Delta(X)$$

where N is the number of nodes. Ψ_Δ is a shape function associated with node Δ and $u_{i\Delta}$ is the value of u_i^h at node Δ (in the following capital Greek symbols will be reserved for denumerating nodes).

The substitution of formulas (4.18) into (4.17) leads to the following matrix equation

$$(S + K)\dot{U} = F^{(n)} + F^{(t)} + F^{(l)} \qquad (4.19)$$

The nonlinear stiffness matrix in each element can be calculated as:

$${}^e K = \int_{{}^e\Omega} G^T C G \, dX$$

where C is the previously introduced elasticity matrix and G is the nonlinear geometric matrix. with elements defined as

$$G_{IJk\Delta} = \frac{\partial E_{IJ}}{\partial u_{k\Delta}} = \frac{\partial \dot{E}_{IJ}}{\partial \dot{u}_{k\Delta}}$$

18

The occurence of the matrix S in the above equation results from the presence of the deformation gradient F in the rate form of large deformation equilibrium equation (4.14). The elements of this matrix are calculated for each element as:

$$^eS_{i\Delta j\Lambda} = \int_{^e\Omega} \Psi_{\Delta,K} \Psi_{\Lambda,L} T_{KL} \delta_{ij} dX$$

and represent additional stiffness due to rotation of the existing current stress state.

The right–hand side vectors represent loads due to the rate of plastic strains, temperature and mechanical loads, respectively. These vectors are defined by

$$^eF^{(n)} = \int_{^e\Omega} G^T C \dot{E}^{(n)} dX$$

$$^eF^{(t)} = \int_{^e\Omega} G^T \dot{E}^{(t)} dX$$

$$^eF^{(l)} = \int_{^e\Omega} \Phi^T b_o dX + \int_{\partial^e\Omega} \Phi^T t_o dS$$

Note that it is convenient to represent and calculate the nonlinear geometric matrix as:

$$G = \mathcal{G}Q$$

or in component form

$$G_{IJK\Delta} = \frac{\partial E_{IJ}}{\partial u_{m,N}} \frac{\partial u_{m,N}}{\partial u_{k\Delta}}$$

In the above, $\mathcal{G}$ is a purely symbolic geometric matrix obtained by differentiation of the nonlinear kinetic formula (4.3), while Q is the discretization matrix with elements defined by

$$Q_{mNk\Delta} = \delta_{km} \Psi_{\Delta,N}$$

4.6 Viscoplastic Solution Method

The general structure of the finite element formulation (4.19) is very similar to that obtained in the infinitesimal theory (see Refs. [33,35]), the difference being the occurrence of the additional matrix S and the dependence of matrix K on the current deformation. Thus the general computational procedure remains practically unchanged after the extension to the large displacement theory.

Also, the inclusion of a damage model in the constitutive equations did not change the general structure of the program, but did require additional evolution of the damage parameters.

With these modifications, the new algorithm proceeds through the following steps:

19

1. At time t, initialize u_i, T_{IJ}, Z_i, and ω_i for each element.

2. Calculate $\dot{E}_{IJ}^{(n)} = f_{ij}(T_{IJ}, Z_k, \omega_k)$ for each element.

3. Assemble and solve $(S + K)\dot{U} = \dot{F}$.

4. Calculate $\dot{E}_{IJ}$ for each element. $\dot{E} = G\dot{U}$.

5. Calculate $\dot{T}_{IJ}$ for each element $\dot{T} = C(\dot{E} - \dot{E}^{(n)}) - C\alpha\dot{T}$.

6. Calculate $\dot{Z}_i$ for each element $\dot{Z}_i = g_i(T_{IK}, Z_i)$.

7. Calculate $\dot{\omega}_i$ for each element $\dot{\omega}_i = h_i(T_{IK}, \omega_i)$.

8. Integrate u_i, $\dot{E}_{IJ}^{(n)}$, $\dot{T}_{IJ}$, $\dot{Z}_i$, $\dot{\omega}_i$ forward for each element to get values at $t + \Delta t$.

9. If $t + \Delta t_s < t_{\text{final}}$ go to 2. otherwise stop.

In the case of the predictor–corrector method, the above sequence is performed at both the predictor and corrector stages and the final values are obtained using averaged rates.

The general approach for this scheme, combined with the adaptive time stepping, is presented in Fig. 8. Note that in the case of large rotations the mechanical deformation can affect the solution of the thermal problem, thus providing two–way coupling instead of the one–way coupling considered so far. Analysis of such cases will be discussed subsequently in the context of a fully coupled fluid-thermal-structural analyses.

It is also important to note that, due to the application of a rate formulation, extension of the analysis to large displacements did not cause any significant increase in the computational time; in particular, no additional iteration loops were necessary. The only additional cost was a slightly more complicated evaluation of the stiffness matrix and load vectors.

5 Implicit/Explicit Method for Compressible Viscous Flow

Finite element analysis of compressible flows is a relatively new development, but significant progress has been made in recent years. Computational techniques have been developed for inviscid and viscous flows. Currently there exists a variety of successful explicit algorithms, the most popular being explicit versions of the Taylor-Galerkin schemes [9,12,13,27,28,29,31] and Runge-Kutta methods [30,31]. Unfortunately, as indicated by our numerical experiments and the experience of other researchers, explicit algorithms are not very effective in

the analysis of viscous flows and in the prediction of aerothermal loads (pressure, skin friction, and heat flux). In these problems, due to stability limitations on the time step, they converge very slow. As a result current research in this area is focused primarily on implicit schemes, or more recently implicit/explicit schemes. The latter approach appears to be the most attractive one, as it combines the robust, unconditionally stable implicit schemes with the relatively cheap explicit schemes, to achieve maximum effectiveness at minimum computational cost.

In this section a finite element formulation of an adaptive implicit/explicit Taylor-Galerkin method for compressible viscous flow is presented. The derivation will follow several logical steps. First, a general family of implicit Taylor-Galerkin algorithms will be formulated. Depending on the selection of implicitness parameters, the fully explicit scheme or a variety of implicit schemes can be obtained within this family. Secondly, a formulation of an implicit/explicit scheme will be presented. This scheme combines implicit and explicit methods in different subdomains of the domain Ω. Finally, different criteria for an adaptive selection of implicit and explicit zones will be presented. Several numerical tests and validation problems will be discussed in Section 6.3.

5.1 A General Family of Implicit Taylor-Galerkin Methods

In this section a general family of implicit Taylor-Galerkin methods will be derived. This family is based on a combination of second-order Taylor series expansions in time with a Galerkin approximation in space (one-, two-, or three-dimensional). Several implicitness parameters will be introduced, so that, depending on the particular choice, a fully explicit scheme or a variety of implicit schemes can be recovered. The family derived here includes, as special cases, most of Taylor-Galerkin type algorithms presented in the literature.

5.1.1 Basic Derivation

Navier-Stokes Equations

The compressible viscous flow of a calorically perfect gas is governed by the Navier-Stokes equation in the form:

$$\dot{u} + F_{i,i} = F^V_{i,i} \qquad (5.1)$$

where u is the vector of conservation variables, F_i are inviscid (convective) flux vectors, and F^V_i are viscous flux vectors. Indices i in the above formula refer to axes of a Cartesian coordinate system, a comma denotes partial differentiation and the summation convention is applied. The components of vectors u, F_i, and F^V_i are given in two-dimensional case by:

$$u = \{\rho, \rho v_1, \rho v_2, \rho e\}^T = \{\rho, m_1, m_2, E\}^T$$

21

$$F_i = \begin{bmatrix} \rho v_i \\ \rho v_1 v_i & + & p\delta_{1i} \\ \rho v_2 v_i & + & p\delta_{2i} \\ (E + p)v_i \end{bmatrix} \tag{5.2}$$

$$\tag{5.3}$$

$$F_i^V = \begin{bmatrix} 0 \\ \sigma_{1i} \\ \sigma_{2i} \\ v_m \sigma_{mi} & + & q_i \end{bmatrix} \tag{5.4}$$

where ρ is the fluid density, p is the pressure, v_i are velocity components, ϵ is a total energy per unit mass, σ_{ij} are stress components, and q_i are components of a heat flux vector.

It should be noted that inviscid fluxes are functions of the conservation variables only:

$$F_i = F_i(u)$$

so that inviscid Jacobians are defined by:

$$A_i = \frac{\partial F_i}{\partial u}$$

Viscous fluxes depend on both conservation variables and their gradients:

$$F_i^V = F_i^V(u, u_{,j})$$

and the corresponding Jacobians are defined by

$$P_i = \frac{\partial F_i^V}{\partial u}$$

$$R_{ij} = \frac{\partial F_i^V}{\partial u_{,j}}$$

Second–Order Taylor Expansion in Time

Assume that the solution u^n is given at the time moment t^n and the solution at time t^{n+1} is to be calculated. Formally, the values of the solution at moments t^n and t^{n-1} can be expressed by the second-order Taylor expansion around an arbitrary moment $t^{n+\alpha}$ (see Fig. 9), where α is the implicitness parameter with values between zero and one:

$$u^{n+1} = u^{n+\alpha} + (1 - \alpha)\Delta t \dot{u}^{n+\alpha} + (1 - \alpha)^2 \frac{\Delta t^2}{2} \ddot{u}^{n+\alpha} + o(\Delta t^3)$$

$$u^n = u^{n+\alpha} - \alpha\Delta t \dot{u}^{n+\alpha} + \alpha^2 \frac{\Delta t^2}{2} \ddot{u}^{n+\alpha} + o(\Delta t^3)$$

22

By subtracting these two formulas one obtains a formula for the increment of the solution between steps n and $n+1$:

$$\Delta u = u^{n+1} - u^n = \Delta t \dot{u}^{n+\alpha} + (1 - 2\alpha)\frac{\Delta t^2}{2}\ddot{u}^{n+\alpha} + o(\Delta t^3) \tag{5.5}$$

Now it is easy to observe that:

$$\ddot{u}^{n+\alpha} = \ddot{u}^{n+\beta} + o((\alpha - \beta)\Delta t)$$

so that—still preserving second-order accuracy—a second implicitness parameter can be introduced into equation (5.5):

$$\Delta u = \Delta t \dot{u}^{n+\alpha} + (1 - 2\alpha)\frac{\Delta t^2}{2}\ddot{u}^{n+\beta} + o(\Delta t^3) \tag{5.6}$$

The next step of the derivation is to express the quantities evaluated at time moments $t^{n+\alpha}$ and $t^{n+\beta}$ by quantities evaluated at the basic steps t^n and t^{n+1}. It is easy to show, using a Taylor series expansion, that:

$$\dot{u}^{n+\alpha} = \dot{u}^n + \alpha \Delta \dot{u} + o(\Delta t^2)$$

$$\ddot{u}^{n+\beta} = \ddot{u}^n + \beta \Delta \ddot{u} + o(\Delta t^2)$$

Substituting these formulas into equation (5.6) yields a two-parameter expansion:

$$\Delta u = \Delta t(\dot{u}^n + \alpha \Delta \dot{u}) + (1 - 2\alpha)\frac{\Delta t^2}{2}(\ddot{u}^n + \beta \Delta \ddot{u}) + o(\Delta t^3) \tag{5.7}$$

Now, following the original idea of Lax and Wendroff, the original equation (5.1) will be substituted to equation (5.7) to replace time derivatives by space derivatives. This substitution yields a formula for the first derivatives:

$$\dot{u} = F_{i,i}^V - F_{i,i} \tag{5.8}$$

and for the second order derivatives, after substitution of the inviscid and viscous Jacobians:

$$\ddot{u} = \left[R_{ij}\left(F_{k,k}^V - F_{k,k} \right)_{,j} + P_i\left(F_{k,k}^V - F_{k,k} \right) \right]_{,i} - \left[A_i\left(F_{k,k}^V - F_{k,k} \right) \right]_{,i} \tag{5.9}$$

It can be observed that the consecutive terms in the equation (5.9) involve spacial derivatives up to the fourth order. Limiting this formula to terms with second-order derivatives, which can be effectively handled by C^0 continuous finite elements, yields an approximation:

$$\ddot{u} = \left(A_i F_{k,k} \right)_{,i} + o(\mu, k) \tag{5.10}$$

23

where $o(\mu, k)$ represents symbolically a quantity of the order of viscosity parameters in the Navier-Stokes equations. Substitution of formulas (5.8) and (5.10) into the incremental equations (5.7) gives the implicit nonlinear formula:

$$\Delta u = \Delta t \left[\left(F_{i,i}^{V n} - F_{i,i}^{n} \right) + \alpha \left(\Delta F_{i,i}^{V} - \Delta F_{i,i} \right) \right]$$

$$+ (1 - 2\alpha)\frac{\Delta t^2}{2} \left[(A_i F_{k,k})_{,i} + \beta \Delta (A_i F_{k,k})_{,i} \right] + o(\Delta t^3) + o(\mu, k)o(\Delta t^2) \tag{5.11}$$

It can be noted that this expansion is second-order accurate for the Euler equations. but only first-order accurate for viscous problems. In the latter case. for the sake of maximum generality, a third implicitness parameter can be introduced by observing that $\Delta F_i^V = o(\mu, k)o(\Delta t)$, so that the second term on the right-hand side of equation (5.11) becomes

$$\alpha \Delta F_{i,i}^{V} - \alpha \Delta F_{i,i}^{V} = \gamma \Delta F_{i,i} - \alpha \Delta F_{i,i} + (\alpha - \gamma)o(\mu, k)o(\Delta t)$$

This substitution preserves the first-order accuracy of the scheme.

Linearization

Equation (5.7) represents a nonlinear formula for increments of the solution u at one time step. This formula is nonlinear due to nonlinear dependence of the fluxes and Jacobians on the solution u. It can be shown. however. that this equation can be effectively linearized while preserving the required accuracy. In particular. by the definition of the inviscid and viscous Jacobians one can write:

$$\Delta F_i = A_i^n \Delta u + o(\Delta t^2)$$

$$\Delta F_i^V = P_i^n \Delta u + R_{ij}^n \Delta u_{,j} + o(\Delta t^2)$$

so that linearization of these terms preserves second-order accuracy of equation (5.7). Note that if the dependence of viscous fluxes on the solution u is neglected. then

$$\Delta F_i^V = R_{ij} \Delta u_{,j} + o(\Delta t)$$

and equation (5.7) is only first-order accurate.

The second-order term in the equation (5.7) is also nonlinear with respect to u. due to dependence of A_i on the solution. Since. however. this term is multiplied by Δt^2. it actually suffices to observe that $\Delta A_i = o(\Delta t)$ and use an approximate expansion:

$$\Delta (A_i F_{k,k})_{,i} = (A_i^n A_k^n \Delta u_{,k})_{,i} + o(\Delta t)$$

in order to preserve the second-order accuracy of the basic formula (5.7).

24

After substitution of these linearized terms into the equation (5.7) and regrouping, a general linear implicit incremental formula is obtained:

$$
\begin{aligned}
\boldsymbol{\Delta u} \; + \; & \alpha \Delta t \left(A_i^n \boldsymbol{\Delta u} \right)_{,i} - \gamma \Delta t \left[\left(R_{ij}^n \boldsymbol{\Delta u}_{,j} \right)_{,i} + \left(P_i^n \boldsymbol{\Delta u} \right)_{,i} \right] + \\
- \; & (1 - 2\alpha)\beta \frac{\Delta t^2}{2} \left(A_i^n A_j^n \boldsymbol{\Delta u}_{,j} \right)_{,i} \\
= \; & \Delta t \left(F_{i,i}^{Vn} - F_{i,i}^n \right) + (1 - 2\alpha)\frac{\Delta t^2}{2} \left(A_i^n F_{k,k}^n \right)_{,i}
\end{aligned}
\tag{5.12}
$$

The above equation is combined with the appropriate boundary conditions to form a bound-ary-value problem over the domain Ω. The particular forms of boundary conditions and their finite element implementations are discussed in Section 5.4. The incremental solutions at consecutive time steps are accumulated to formulate a solution of the time–dependent problem. If one prefers to do so, the above equation can easily be recast in a form in which the new solution u^{n+1} is calculated instead of the increment $\boldsymbol{\Delta u}$.

Remarks Concerning Eq. (5.12)

1. Formula (5.12) is a linear equation for the increment $\boldsymbol{\Delta u}$. The formulation is in general implicit, except when $\alpha = \beta = \gamma = 0$, in which case the explicit scheme is recovered. The interpretation of different implicitness parameters is as follows:

   α — represents implicitness of the advective terms.

   β — represents implicitness of the viscous terms.

   γ — represents implicitness of the second order terms.

2. The scheme is generally first–order accurate in time for the Navier-Stokes equations. but it is second–order accurate for:

   — Euler equations
   — Navier-Stokes equations with $\alpha = \gamma = .5$ (Crank-Nicholson scheme)

   In order to distinguish scheme (5.12) from the purely first–order methods. it will be referred to as an (incomplete) second–order scheme.

3. If all the terms with coefficient $(1 - 2\alpha)$ are eliminated in equation (5.12), then the purely first–order scheme is obtained.

4. The above scheme includes as special cases most of the other finite element schemes based on a second–order Taylor series expansion in time, in particular:

- $\alpha = 0$, $\beta = 0$, $\gamma = 0$ corresponds to the popular explicit Taylor-Galerkin method.

- $\alpha = 0$, $\beta \neq 0$ with no viscosity terms corresponds to the so-called weakly implicit method applied to the Euler equations by Demkowicz, Rachowicz, and Oden [11] and others,

- $\alpha = 0$, $\beta = 1$, $\gamma = 1$ corresponds to an implicit scheme used by Hassan, Morgan, and Peraire [17].

Moreover, a variety of second-order algorithms developed by Donea [9] and Donea, Giuliani, Laval, and Quartapelle [12] can be obtained within this family (with the exception of the third-order schemes developed by Donea, Quartapelle and Selmin [13] for convection problems).

Similarly, several corresponding finite difference algorithms can also be identified. In particular a family of implicit schemes developed for the Euler equations by Lerat [21].

5.1.2 Linear Stability Analysis

It is of interest to analyze stability, dissipation, and dispersion properties of the various schemes obtained within the family derived in the previous section. Such an analysis was performed for a simplified, one-dimensional linear advection-diffusion equation of the form:

$$\dot{u} + a u_{,x} + b u_{,xx} = 0 \qquad \text{in } [0, L] \times [0, T]$$

with periodic boundary conditions:

$$u(0, t) = u(L, t)$$
$$u_{,x}(0, t) = u_{,x}(L, t)$$

For this equation, incremental equation corresponding to the formula (5.12) was formulated and a discrete finite element scheme was derived, assuming:

- a uniform mesh of spacing $h = L/N$, where N is the total number of elements

- a lumped mass matrix

The lumped mass matrix was considered here because—as results from arguments which will be presented in Section 5.4—it significantly improves the computational efficiency of mixed implicit/explicit schemes. Application of a standard von Neumann stability analysis to the

26

resulting scheme, yields a formula for an amplification coefficient for mode $m(m = 0, \ldots, N)$ in the form:

$$C_m = \frac{\left[1 + ((1 - \gamma)\dfrac{CFL}{Re} + (1 - 2\alpha)(1 - \beta)CFL^2)(\cos \beta_m - 1)\right] + i[(1 - \alpha)CFL \sin \beta_m]}{\left[1 + \left(-\gamma\dfrac{CFL}{Re} + (1 - 2\alpha)(1 - \beta)CFL\right)(\cos \beta_m - 1)\right] + i[-\alpha CFL \sin \beta_m]}$$

(5.13)

where CFL is a Courant-Friedrich-Levy number for this problem:

$$CFL = \frac{a\Delta t}{h}$$

Re is a mesh Reynolds number:

$$Re = \frac{ah}{b}$$

β_m is defined in terms of a wave number k_m as:

$$\beta_m = k_m h = \pi \frac{mh}{L}$$

and $i = \sqrt{-1}$.

The above formula was used to analyze the dissipation and dispersion properties for various combinations of implicitness parameters. Some results of the stability analysis are summarized below. For simplicity, the figures presented will refer only to pure advection problems $(1/Re = 0)$.

1. Fully explicit scheme: $\alpha = 0$, $\beta = 0$, $\gamma = 0$.

   The results of stability analysis for this scheme are graphically presented in Fig. 10. The figure presents modules of the amplication factor C for increasing values of the CFL number (which corresponds to an increasing time step). Actually, the figure is a graph, with values of the amplification factors for different modes spanning the area between a horizontal line $|C| = 1$ (mode $m = 0$), and curve A (mode $m = N$). The scheme is stable for given time step if the graph for this step is below the horizontal line $|C| = 1$, otherwise the scheme is unstable.

   As expected, the explicit scheme is conditionally stable with the stability limit for pure advection being $CFL \leq 1$.

2. Weakly implicit scheme: $\alpha = 0$, $\beta = .5$, $\gamma = .5$.

   The stability and dissipation analysis for this scheme is presented in Fig. 11. The scheme is unconditionally stable, with dissipation properties diminishing with an increasing time step. Thus it can be expected that this scheme may be oscillatory at large time steps.

27

3. Weakly implicit scheme: $\alpha = 0$, $\beta = 1$, $\gamma = 1$.

   The stability and dissipation analysis for this scheme is presented in Fig. 12. The scheme is unconditionally stable, with dissipation properties for higher modes increasing with an increasing time step.

4. Crank-Nicholson scheme: $\alpha = .5$, $\beta = .5$, $\gamma = .5$.

   This scheme is unconditionally stable (See Fig. 13), with no dissipation for pure advection problems (for a regular one-dimensional mesh). Thus it can be expected to be oscillatory for advection-dominated problems. However, since this scheme is actually second-order accurate for the Navier-Stokes equations, it can be very effective within boundary layer subregions.

Before other schemes are discussed, it should be noted that for the schemes discussed so far, the implicitness parameter α was equal to zero. The following two cases will have $\alpha \neq 0$.

5. Implicit scheme: $\alpha = 1$, $\beta = 0$, $\gamma = 0$.

   The stability and dissipation analysis for this scheme is presented in Fig. 14. Surprisingly, implicit treatment of the convection terms spoils the stability and this scheme is unconditionally unstable for pure advection problems.

6. Fully implicit scheme: $\alpha = 1$, $\beta = 1$, $\gamma = 1$.

   Contradictory to what would be intuitively expected, this fully implicit scheme is not the most stable. As can be seen in Fig. 15, this scheme is stable for large time steps and unstable for small time steps. This surprising result is actually confirmed in a numerical solution of the Navier-Stokes equations.

The above few examples outline the nature of dependence of the stability and dissipation properties of second-order schemes on the selection of the implicitness parameters. The behavior of schemes corresponding to intermediate values of these parameters can be interpolated from the above results or precisely analyzed using the formula (5.13).

A similar stability analysis can be performed for the first-order scheme, which is obtained by dropping terms with multiplier $(1 - 2\alpha)$. In this case, the coefficient β disappears from equations and properties of the scheme depend on the values of α and γ. The general result of the stability analysis is that:

- For $\alpha \leq .5$ and $\gamma \leq .5$ the scheme is conditionally stable for advection-diffusion problems. For pure advection problems, the scheme is unconditionally unstable.

28

- For $.5 \leq \alpha \leq 1$ and $.5 \leq \gamma \leq 1$ the scheme is unconditionally stable. The dissipation and dispersion properties for $\alpha = 1$, $\gamma = 1$ are quite similar to the properties of the second order scheme with $\alpha = 0$, $\beta = 1$, $\gamma = 1$.

It is of interest to note that the effect of an implicit treatment of the convective terms changes dramatically depending on the order of the scheme. While in the first-order scheme it is necessary for unconditional stability, in the second-order scheme it actually destroys stability.

The results of the above stability analysis, although based on the simplified, one-dimensional equation, are very well confirmed in the solution of the Navier-Stokes equations in multidimensional domains.

5.2   Weak Formulation

In order to obtain a weak, variational formulation of the incremental equation (5.12), the spaces of trial and test functions were introduced:

$$U = \left\{ \boldsymbol{u} = (u_1, u_2 \ldots u_M) \ s.t. \ u_i \in H^1(\Omega) \text{ and } u_i = \hat{u}_i \text{ on } \Gamma_{Di} \right\}$$

$$V = \left\{ \boldsymbol{v} = (v_1, v_2 \ldots v_M) \ s.t. \ v_i \in H^2(\Omega) \text{ and } v_i = 0 \text{ on } \Gamma_{Di} \right\}$$

where M is the number of conservation variables, $H^1(\Omega)$ is the Hilbert space, and Γ_{Di} is the boundary with specified Direchlet boundary conditions for variable u_i. Note that the notion of Dirichlet boundary conditions is rather symbolic here, since the actual boundary conditions are often imposed on characteristic variables rather than conservation variables u_i (see Section 5.4).

After multiplication of the incremental equation (5.11) by an arbitrary test function $\boldsymbol{v}(\boldsymbol{x})$, integrating over the domain Ω and application of the divergence theorem, the following weak formulation of the problem is obtained:

Find $\Delta u \in U s.t. \; \forall \; v \in V$:

$$\int_\Omega \Delta u \cdot v - \alpha \Delta t A_i^n \Delta u \cdot v_{,i} + \gamma \Delta t R_{ij}^n \Delta u_{,j} \cdot v_{,i}$$

$$+ \gamma \Delta t P_i^n \Delta u \cdot v_{,i} + (1 - 2\alpha)\beta \frac{\Delta t^2}{2} A_i^n A_j^n \Delta u_{,j} \cdot v_{,i} d\Omega$$

$$+ \int_{\partial\Omega} \alpha \Delta t n_i A_i^n \Delta u \cdot v - \gamma \Delta t n_i R_{ij} \Delta u_{,j} \cdot v$$

$$- \gamma \Delta t n_i P_i \Delta u \cdot v - (1 - 2\alpha)\beta \frac{\Delta t^2}{2} n_i A_i^n A_j^n \Delta u_{,j} \cdot v dS \qquad (5.14)$$

$$= \int_\Omega \Delta t \left(F_i^n - F_i^{Vn} \right) \cdot v_{,i} - (1 - 2\alpha)\frac{\Delta t^2}{2} A_i^n F_{j,j}^n \cdot v_{,i} d\Omega$$

$$+ \int_{\partial\Omega} -\Delta t n_i \left(F_i^n - F_i^{Vn} \right) \cdot v + (1 - 2\alpha)\frac{\Delta t^2}{2} n_i A_i^n F_{j,j}^n \cdot v dS$$

It can be shown. by selection of appropriate test functions, that the solution of this problem is—in the sense of distributions—the solution of the boundary–value problem formulated in Section 5.1.

5.3 Finite Element Approximation

The Galerkin approximation of the variational problem (5.14) is obtained by partitioning the domain Ω into the finite element mesh and introducing an approximation of trial functions and their derivatives:

$$u^h(x.t) = \sum_{I=1}^N U_I \Psi_I(x)$$

$$u_{,i}^h(x.t) = \sum_{I=1}^N U_I \Psi_{I,i}(x)$$

and the same for test functions v. In the above formula N is the number of nodes within the domain Ω and $\Psi_I(x)$ is the shape function associated with node I. After introducing this approximation into the variational statement (5.14) and requiring that it be satisfied for every combination of V_I. the following matrix equation is obtained:

$$(M + K)\Delta U = R$$

where M is the mass matrix. K is the "stiffness" matrix and R is the right–hand side vector. It is convenient to present the above equation in the semi–indexed notation:

$$(M_{IJ} + K_{IJ})\Delta U_J = R_I$$

30

where M_{IJ} and K_{IJ} are small blocks of size $M \times M$ associated with nodes I and J (recall that M is the number of conservation variables).

The particular forms of these matrices corresponding to the variational problem (5.14) is—before application of boundary conditions—the following:

1. Mass matrix

$$M_{IJ} = \int_\Omega I_{M\times M} \Psi_I \Psi_J d\Omega$$

2. Stiffness matrix due to interior integrals:

$$
\begin{aligned}
K_{IJ} &= \int_\Omega -\alpha\Delta t A_i^n \Psi_J \Psi_{I,i} \\
&+ \gamma\Delta t R_{ij}^n \Psi_{J,j} \Psi_{I,i} \\
&+ \gamma\Delta t P_i^n \Psi_J \Psi_{I,i} \\
&+ (1-2\alpha)\beta \frac{\Delta t^2}{2} A_i^n A_j^n \Psi_{J,j} \Psi_{I,i} d\Omega
\end{aligned}
$$

3. Right–hand side due to interior integrals:

$$
\begin{aligned}
R_I &= \int_\Omega \Delta t \left(F_i^n - F_i^{Vn} \right) \Psi_{I,i} \\
&- (1-2\alpha)\frac{\Delta t^2}{2} A_i^n F_{j,j}^n \Psi_{I,i} d\Omega
\end{aligned}
$$

4. Stiffness matrix due to boundary integrals:

$$
\begin{aligned}
K_{IJ} &= \int_{\partial\Omega} \alpha\Delta t A_i n_i \Psi_J \Psi_I + \\
&- \gamma\Delta t R_{ij} n_i \Psi_{J,j} \Psi_I + \\
&- \gamma\Delta t P_i n_i \Psi_J \Psi_I + \\
&- (1-2\alpha)\beta \frac{\Delta t^2}{2} n_i A_i A_j \Psi_{J,j} \Psi_I ds
\end{aligned}
$$

5. Right–hand side due to boundary integrals:

$$R_I = \int_{\partial\Omega} -\Delta t F_i^n n_i \Psi_I$$

$$+ \quad \Delta t F_i^{Vn} n_i \Psi_I$$

$$+ \quad (1 - 2\alpha)\frac{\Delta t^2}{2} n_i A_i^n F_{j,j}^n \Psi_I$$

It should be noted that—as a result of the derivation of the algorithm—the elements of the stiffness matrix K are in fact consistent linearizations of corresponding terms on the right-hand side, for example:

$$K_{IJ}^V = (-\gamma)\frac{\partial R_I^V}{\partial U_J}$$

where superscript V denotes terms associated with natural viscosity. This remark is very important for the development of various modifications of the algorithm, because every modification of the right-hand side must be accompanied by a consistent modification to the left-hand side—otherwise the stability of the algorithm is spoiled. For example, if the group approximation of convective fluxes is applied, then the calculation of Jacobians A_i on the left-hand side must correspond to this procedure.

5.4 Artificial Dissipation

In order to suppress spurious oscillations of the solution, a variety of models of artificial dissipation are used. In this work we will assume that the artificial dissipation can be introduced as the additional flux in the Navier-Stokes equations in the form:

$$\dot{u} + F_{i,i} = F_{i,i}^V + F_{i,i}^A$$

where the artificial dissipation flux is the function of the solution vector and its derivatives:

$$F_i^A = F_i^A(u, u_{,j})$$

with corresponding Jacobians defined as:

$$P_i^A \quad = \quad \frac{\partial F_i^A}{\partial u}$$

$$R_{ij}^A \quad = \quad \frac{\partial F_i^A}{\partial u_{,j}}$$

The advantage of this approach is that the artificial dissipation can be treated using exactly the same formulation and procedures as for the natural viscosity. In the implicit algorithm, for the sake of generality, a fourth implicitness parameter γ is introduced for the

32

terms associated with the artificial dissipation. In the calculation of the stiffness matrices. right–hand sides and boundary terms the same formulas are used as for the natural viscosity.

Within the above framework, various models of artificial dissipation can be formulated relatively easy. For example, a straightforward extension of the original Lapidus dissipation [20] to multidimensional cases yields artificial fluxes defined as:

$$F_i^A = k^{ii} u_{,j} \tag{5.15}$$

with

$$k^{ii} = c_k A_e |v_{i,i}|$$

where c_k is a coefficient (usually between zero and one), A_e is the element area. and v_i are the components of velocity vector (no summation on i). The Jacobians P and R can be defined by straightforward differentiation of formula (5.15).

Another generalization of the Lapidus concept was proposed by Löhner and Morgan [22]. Within the framework proposed here, the fluxes corresponding to their model are of the form:

$$F^A = lk\frac{\partial u}{\partial l}$$

or

$$F_i^A = l_i k l_j u_{,j} \tag{5.16}$$

where l is the normalized gradient of the magnitude of velocity:

$$l = \frac{grad|v|}{|grad|v||}$$

and the coefficient k is calculated from the formula:

$$k = c_l A_e (l \cdot grad(v \cdot l))$$

The Jacobians P and R can be defined by differentiation of formula (5.15). If, for simplicity, dependence of k and l on the solution is disregarded, then:

$$\begin{aligned} P_i &= 0 \\ R_{ij} &= k l_i l_j I \end{aligned} \tag{5.17}$$

where I is the identity matrix of dimension M. In the incremental equation (5.12), the above approach leads to an additional term of the form:

$$\Delta t \left[l_i k \frac{\partial u}{\partial l} \right]_{,i}$$

33

which differs slightly from the original formula proposed by Löhner and Morgan (equation (9) in [22]). These two versions are equivalent only for l constant throughout the domain. It can be verified, however, that the directional derivative used in [22] is not in divergence form and thus cannot be directly used in the variational formulation for arbitrary l. It is actually the above term that yields—with no additional assumptions—the diffusion matrix R of the form (5.17).

5.5 Boundary Conditions

Proper formulation and application of boundary conditions is one of the most difficult problems of computational fluid mechanics. While this topic has received considerable attention from the theoretical point of view and within the finite difference method framework (references [14,16,32]). a theoretical background for the treatment of the boundary conditions within the finite element framework, especially in an implicit approach. is not yet complete.

Before discussion of boundary conditions for the implicit Taylor-Galerkin method. it is useful to quote the general result of Strikverda [32], which specifies the number of boundary conditions necessary for well–posedness of the linearized Euler and Navier-Stokes equations. These results are summarized for two–dimensional problems in the table below.

Type of Boundary	Euler (not regularized)	Navier-Stokes
supersonic inflow	4 ess	4 ess
subsonic inflow	3 ess	3 ess + 1 nat
subsonic outflow	1 ess	1 ess + 2 nat
supersonic outflow	0	0 ess + 3 nat
no–flow	1 ess	1 ess + 2 nat
solid wall		
—isothermal	—	3 ess
—heat flux	—	2 ess + 1 nat

In this table "ess" denotes the essential boundary condition and "nat" denotes natural boundary conditions. The essential conditions are to be imposed on the characteristic variables rather than the conservation variables (see Section 5.5.1). It is of importance to note that the numbers presented in the table are true for problems that are not regularized. If—as is the case of virtually all computational techniques—some artificial diffusion is built into the algorithm or added explicitly. natural boundary conditions should be imposed on these terms even for Euler problems. Moreover, since artificial diffusion—in contradiction to

the natural viscosity—affects all the conservation variables. the number of natural boundary conditions for these terms should actually be one more than for the (nonregularized) Navier-Stokes equations.

In the following sections the formulation of the boundary conditions for various boundary types will be discussed. Presentation of the theoretical background will be limited to the necessary minimum and the interested reader is referred to works [14,16,32] and references therein.

5.5.1 Characteristic Decomposition of Boundary Terms

Before the presentation of the various boundary conditions it is useful to recast the boundary integrals in terms of the characteristic variables (Riemann invariants).

In the variational formulation a typical boundary term is of the form:

$$A_i n_i \Delta u \cdot v = A_n \Delta u \cdot v \qquad (5.18)$$

where A_n is a nonsymmetric matrix. The matrix A_n can formally be presented in its own eigenbasis as:

$$A_n = \sum_{\alpha=1}^{M} \lambda_\alpha (b_\alpha \otimes c_\alpha)$$

where b_α and c_α are the left and right eigenvectors. respectively. The eigenvalues λ_α are defined in the two–dimensional case as:

$$\lambda_1 = v_n - c$$
$$\lambda_2 = v_n$$
$$\lambda_3 = v_n$$
$$\lambda_4 = v_n + c$$

where v_n is the velocity normal to the boundary and c is the speed of sound. The expressions for eigenvectors b_α and c_α can be found in references [11,14,32]. Note that a positive value of λ_α means that the corresponding characteristic exits the domain across a given boundary. while negative values of λ_α correspond to signals entering the domain.

The characteristic variable u_α are defined as components of the vector u in the eigenbasis of A_n so that:

$$\Delta u = (\Delta u \cdot b_\alpha) c_\alpha = \Delta u_\alpha c_\alpha$$

$$v = (v \cdot c_\alpha) b_\alpha = v_\alpha b_\alpha$$

With these definitions, the boundary formula (5.18) can be presented in terms of character-istic variables as:

$$A_n \Delta u \cdot v = \sum_{\alpha=1}^{M} \lambda_\alpha v_\alpha \qquad (5.19)$$

The above representation is very useful in the formulation of essential boundary conditions. As a general rule, the characteristic variables corresponding to characteristics entering the domain (negative λ_α) need to be specified as the essential boundary conditions, while the characteristic variables exiting the domain are continued across the boundary from the interior.

5.5.2 Supersonic Inflow

On the supersonic inflow the values of all the characteristic variables (thus also of all the conservation variables) are specified as the upstream values. Formally, this means that:

$$u = \bar{u} \text{ on } \partial \Omega_I$$

or, in the incremental form:

$$\Delta u = \bar{u} - u^n \text{ on } \partial \Omega_I$$

In practical applications these conditions are enforced by the penalty method, which is obtained by adding to the variational formulation a term:

$$\frac{1}{\epsilon} \int_{\partial \Omega_i} [\Delta u - (\bar{u} - u^n)] \cdot v ds$$

where ϵ is a small parameter.

The corresponding stiffness matrices and right-hand sides are of the form:

$$K_{IJ} = \int_{\partial \Omega_I} \frac{1}{\epsilon} I \Psi_I \Psi_J ds$$

$$R_I = \int_{\partial \Omega_I} \frac{1}{\epsilon} (\bar{u} - u^n) \Psi_J ds$$

where I is the identity matrix of the size M. Simple nodewise enforcement of these conditions is obtained by formally replacing the shape functions with Dirac delta functions to obtain:

$$K_{IJ} = \frac{1}{\epsilon} I$$

$$R_I = \frac{1}{\epsilon} (\overline{U}_I - U_I^n)$$

36

5.5.3 Supersonic Outflow

On the supersonic outflow all the characteristic variables are continued from the interior of the domain, so that no essential boundary conditions are imposed. The explicit algorithm application of supersonic outflow boundary conditions is achieved simply by calculation of the boundary integrals. In the implicit algorithm, natural boundary conditions are imposed on viscous and second-order terms.

Natural boundary conditions on viscous terms are imposed by observing that the viscous boundary terms on the left-hand side of the variational equation (5.14) can be interpreted as:

$$K_{IJ}^V \Delta U_J = \int_{\partial \Omega_o} -\gamma \Delta t \left(R_{ij}^n n_i \Psi_{J,j} \Psi_I + P_i n_i \Psi_I \Psi_J \right) \Delta U_J ds$$

$$= \int_{\partial \Omega_o} -\gamma \Delta t \Delta F_n^V \Psi_I ds$$

where the components of ΔF_n^V are:

$$\Delta F_n^V = \{0, \Delta \sigma_{1n}, \Delta \sigma_{2n}, \Delta q_n\}^T$$

In order to formally impose natural boundary conditions the above terms are transferred to the right-hand side with prescribed values of ΔF_n^V, so that the new right-hand side is:

$$\widetilde{R}_I = R_I + \int_{\partial \Omega_o} \gamma \Delta t \overline{\Delta F}_n^V \Psi_I ds$$

Note that since the mass flux due to viscous terms is identically zero, this procedure actually imposes only three natural boundary conditions (in two dimensions).

The choice of the actual conditions is somewhat arbitrary. Currently two options are implemented, namely:

- zero change of flux at the time step (frozen viscous flux):

$$\overline{\Delta F}_n^V = 0$$

- zero total viscous flux, enforced by:

$$\overline{\Delta F}_n^V = 0 - F_n^{V n}$$

Obviously, on an outflow boundary adjacent to a solid wall the viscous fluxes are not zero and the first procedure is more appropriate.

In order to ensure well–posedness of the problem, proper natural boundary conditions should also be imposed on the second–order terms. Analogously, as in the viscous case, second–order terms on the left–hand side of equation (5.14) can be transformed to the form:

$$K_{IJ}^{D} \Delta U_J = \int_{\partial \Omega_o} -(1 - 2\alpha)\beta \frac{\Delta t^2}{2} \Psi_I (A_n \Delta F_{i,j}) ds$$

This term has no simple physical interpretation and therefore the selection of the natural boundary condition to be imposed is somewhat difficult. The procedure adopted by Demkowicz, Rachowicz and Oden [11] is to decompose the above term into components normal and tangential to the boundary and impose boundary conditions only on the normal term (symmetry boundary conditions). In this work a slightly different procedure was applied, according to which the whole term is transferred to the right–hand side with certain prescribed values. This corresponds to imposing natural boundary conditions on

$$A_n \Delta F_{j,j} = A_n A_j \Delta u_{,j}$$

The actual boundary condition applied is to set total value of this term to zero, so that the prescribed value at the time step is:

$$A_n A_j \Delta u_{,j} = 0 - A_n A_j u_{,j}^n \tag{5.20}$$

The intuitive interpretation of this condition can be obtained by observing that for Euler problems the enforced condition is $A_n \dot{u} = 0$, or in terms of characteristic variables:

$$\lambda_\alpha \dot{u}_\alpha b_\alpha = 0 \qquad \alpha = 1 \ldots M$$

Since on the supersonic outflow all the eigenvalues satisfy $\lambda_\alpha > 0$, this condition means that the characteristic variables do not change in time as they cross the boundary. This corresponds quite well to the idea of the continuation from the interior across the far–field boundary.

A somewhat more appealing interpretation can be presented for the simple two–dimensional advection equation:

$$\dot{u} = a_i u_{,i} \qquad i = 1,2$$

for which the characteristics are straight lines defined in space–time by the vector $c = \{a_1, a_2, 1\}$ (see Fig. 16). The natural boundary condition corresponding to (5.20) is:

$$n_i a_i a_j u_{,j} = 0$$

or equivalently:

$$a_n \langle Du, a \rangle = 0$$

38

where $\langle \boldsymbol{Du}, \boldsymbol{a} \rangle$ denotes directional derivative of u in the direction of $\boldsymbol{a}$. This means that on the outflow boundary ($a_n > 0$) u must be constant along advection lines.

On the contour plot this enforces contours of u to be parallel to advection lines on the boundary. It can be observed that the condition applied by Demkowicz, Rachowicz and Oden [11] enforces derivatives of u along the normal to the boundary $\boldsymbol{n}$ to be zero, which corresponds to contour lines normal to the boundary.

5.5.4 Subsonic Inflow and Outflow

On the subsonic inflow or outflow boundary essential boundary conditions are imposed only on the characteristic variables corresponding to negative eigenvalues λ_α. For each of these terms the corresponding condition is:

$$u_\alpha = \bar{u}_\alpha \text{ on } \partial\Omega_{IO}$$

or, in the incremental form:

$$\Delta u_\alpha = \bar{u}_\alpha - u_\alpha^n$$

If the prescribed far–field values of the conservation variables are denoted by $\bar{u}$, then the penalty term enforcing essential boundary conditions on the selected characteristic variables u_α is of the form:

$$K_{IJ} = \frac{1}{\epsilon} \int_{\partial\Omega} (\boldsymbol{c}_\alpha \otimes \boldsymbol{b}_\alpha) \Psi_I \Psi_J ds$$

$$R_J = \frac{1}{\epsilon} \int_{\partial\Omega} [(\bar{\boldsymbol{u}} - \boldsymbol{u}^n) \cdot \boldsymbol{b}_\alpha] \boldsymbol{c}_\alpha \Psi_I ds$$

Nodewise application of these conditions is obtained analogously as for supersonic inflow by replacing the shape functions with Dirac delta functions.

For the characteristic variables with nonnegative eigenvalues the "continuation from the inside" conditions should be applied. Formulating these conditions for selected characteristic variables leads to rather complicated formulas. Thus, for practical applications it is better to observe that, since the penalty procedure actually overrides any other conditions, the continuation condition can be first applied to the whole vector of conservation variables (by the supersonic outflow procedure), and then the above penalty method can be applied to selectively enforce essential boundary conditions.

It should also be noted that all the farfield boundaries are actually artificial and are supposed to represent the cut–off sections of the flowfield where "nothing special happens." Thus, if these boundaries are chosen too close to the complex flow phenomena, ambiguous results can always be expected.

5.5.5 Solid Wall

There are basically two types of solid wall boundaries:

- adiabatic walls with prescribed zero heat flux (M-th component of the viscous flux vector):

$$q_n = F^V_{n(M)} = 0$$

- isothermal walls with specified temperature:

$$T = \overline{T}$$

In addition to the above conditions, zero velocity (zero momentum) conditions are also specified on the solid wall. These conditions are easily enforced by the selective application of the penalty method, similar to the supersonic inflow procedure. The incremental form of the adiabatic condition of zero heat flux is

$$\Delta F^V_{n(M)} = -F^{V_n}_{n(M)} \tag{5.21}$$

This natural boundary condition is applied by formally transferring the viscous terms corresponding to the energy equation from the left–hand side of the variational equation (5.14) to the right–hand side and setting the increment of the heat flux according to (5.21). This type of procedure was already presented for supersonic outflow. It is of interest to note that since the viscous terms do not directly affect mass fluxes and the momentum equations are overridden by the penalty method, in practice all viscous contributions can be skipped on the left–hand side.

On the isothermal wall the additional boundary condition is a prescribed temperature $\overline{T}$ or, equivalently, a prescribed specific energy $\bar{e}$. Since the kinetic energy is zero on the wall, the above condition can be expressed in terms of conservation variables as:

$$\frac{E}{\rho} = \bar{e}$$

In the incremental form this condition is:

$$\frac{1}{\rho}\Delta E - \frac{E}{\rho}\Delta\rho = (\bar{e} - e^n) \tag{5.22}$$

This condition is imposed via the penalty method. It should be noted that there are available a variety of possible forms of the penalty terms, depending on the form of the test term applied to condition (5.22). One possibility, which appears to be the most natural and yields

a symmetric contribution to the stiffness matrix. is obtained by testing equation (5.22) with its own variation:

$$\frac{1}{\epsilon}\left[\left(\frac{1}{\rho}\Delta E - \frac{E}{\rho}\Delta\rho\right) - (\bar{e} - e^n)\right] \cdot \delta\left(\frac{1}{\rho}v_{(M)} - \frac{E}{\rho}v_{(1)}\right)$$

where $v_{(1)}$ denotes a selected component of a test vector: $v_{(1)}$ for density and $v_{(M)}$ for energy.

This approach leads to two penalty conditions affecting both the continuity and energy equations. Therefore it is not in agreement with the physical situation because. while the solid wall can supply heat to maintain a prescribed termperature. it cannot supply mass for this purpose. Due to this reason. another form of the penalty term should be used. which enforces a prescribed temperature by altering the energy equation only:

$$\frac{1}{\epsilon}\left[\left(\frac{1}{\rho}\Delta E - \frac{E}{\rho}\Delta\rho\right) - (\bar{e} - e^n)\right] \cdot v_{(M)}$$

The corresponding terms in the stiffness matrix and the right-hand side are:

$$K_{IJ} = \int_{\partial\Omega_W} k\Psi_I\Psi_J ds$$

$$R_I = \int_{\partial\Omega_W} r\Psi_I ds$$

(5.23)

where the kernel matrices k and r are defined (in two dimensions) as:

$$k = \frac{1}{\epsilon}\begin{bmatrix} 0 & 0 & 0 & 0 \\ 0 & 0 & 0 & 0 \\ 0 & 0 & 0 & 0 \\ -\dfrac{E}{\rho} & 0 & 0 & 1 \end{bmatrix}$$

$$r = \frac{1}{\epsilon}(m_i n_i)\begin{bmatrix} 0 \\ 0 \\ 0 \\ \rho(\bar{e} - e^n) \end{bmatrix}$$

Again. nodewise enforcement of these conditions can be obtained by replacing shape functions with Dirac delta functions.

For the regularized problem some additional artificial terms (fluxes) occur on the solid wall due to second-order terms and explicit artificial dissipation. These fluxes are forced to be zero by means of natural boundary conditions. in the same manner as for the supersonic outflow.

41

5.5.6 No-Flow

The basic condition of the no-flow boundary is that the normal velocity is zero or, equivalently, that the normal momentum is zero:

$$m_i n_i = 0$$

In the incremental form this becomes:

$$\Delta m_i n_i = -m_i^n n_i$$

This condition is easily enforced by the penalty function, with the additional term in the variational formulation:

$$\frac{1}{\epsilon} \int_{\partial \Omega_w} \left(\Delta m_i n_i + m_i^n n_i \right) v_{(1+i)} ds \tag{5.24}$$

where $v_{(1+i)}$ is the test function corresponding to momentum m_i. The resulting stiffness matrices and right-hand sides are of the standard form (5.23), with kernals (in two dimensions):

$$k = \frac{1}{\epsilon} \begin{bmatrix} 0 & 0 & 0 & 0 \\ 0 & n_1 n_1 & n_1 n_2 & 0 \\ 0 & n_2 n_1 & n_2 n_2 & 0 \\ 0 & 0 & 0 & 0 \end{bmatrix}$$

$$r = -\frac{1}{\epsilon}(m_i n_i) \begin{bmatrix} 0 \\ n_1 \\ n_2 \\ 0 \end{bmatrix}$$

For the viscous flow the additional conditions on the no-flow boundary are the two natural boundary conditions:

$$\sigma_{ns} = 0$$
$$q_n = 0$$

where σ_{ns} is the skin friction on the boundary and q_n is the normal heat flux. The application of these natural boundary conditions follows the procedure discussed in preceding subsections.

Similarly, as on the solid wall, all the artificial fluxes are forced to be zero on the no-flow boundary.

5.6 Implicit/Explicit Procedures

The basic idea of implicit/explicit algorithms is simple: combine the two methods to take advantage of superior features of each of them. The major advantage of the explicit method is that element computations are relatively cheap and simple. Unfortunately this method suffers from stability limitations of the time step, which in some problems leads to prohibitively large numbers of time steps.

The implicit algorithm is unconditionally stable and thus allows for an application of larger time steps than explicit method (but there are still some other limitations). Moreover, due to the existence of implicit boundary terms it allows for an easy and straightforward control of natural boundary conditions, in particular the viscous fluxes. An additional advantage is that with larger time steps no explicit artificial dissipation is required. which is very important in the calculation of boundary fluxes. in particular wall heating rates. The major disadvantage is much higher cost of element operations and more complex and expensive solution of the resulting system of equations.

In this section the formulation and numerical implementation of an adaptive implicit/explicit algorithm will be presented. The algorithm will be based on the general family of Taylor-Galerkin methods discussed in the previous sections.

5.6.1 Formulation of Implicit/Explicit Schemes

Assume for now that subregions to be treated with implicit and explicit methods are defined. Then the question arises as to what is a proper procedure for combining implicit/explicit computations. "Proper" here means that it maintains conservative properties of the algorithm and the required order of approximation.

Some of the possible procedures are examined below:

Procedure I

The first possible approach. applied for example by Hassan. Morgan and Peraire [17] is based on the following two steps:

1. Perform the explicit step computations on all nodes in the mesh.

2. Perform the implicit computations in the subregions. where the stability criterion for the explicit scheme: $C \leq 1$, is violated. The solution in remaining nodes is "frozen" at this step.

This simple procedure has one basic disadvantage: it appears to be nonconservative and it may disturb the regularity of the solution in the transition zone. This is caused by the fact that during Step 2 the "frozen" explicit nodes impose the actual Dirichlet boundary condition on the edge of the implicit zone. Prescribing Dirichlet boundary condition for the Navier-Stokes equation means that there must exist an (external) source of fluxes to support the prescribed state of the solution. Since no such external source exists within the computational domain, the solution will not be conservative across the implicit/explicit line. Due to enforcement of the Dirichlet boundary conditions the solution may exhibit a "ramp" or "kink" along this line.

Procedure II

The second procedure considered is based on a division of the computational domain Ω into two subregions $\Omega^{(I)}$ and $\Omega^{(E)}$ (see Fig. 17), such that:

$$\Omega^{(E)} \cap \Omega^{(I)} = 0 \ , \ \ \Omega^{(E)} \cup \Omega^{(I)} = \Omega$$

It is convenient to assume that the interface between the two regions coincides with the element boundaries.

It can be easily observed that the differential equations to be solved on the two subregions are different due to different implicitness parameters applied in each zone: $\alpha^{(I)}, \beta^{(I)}, \gamma^{(I)}$ in the implicit zone and $\alpha^{(E)}, \beta^{(E)}, \gamma^{(E)}$ in the explicit zone (in fact the latter are zero). Therefore, the variational formulation (5.14), based on the assumption of constant implicitness parameters, cannot be applied to the domain Ω. Instead, it can be applied separately to each subdomain with additional continuation conditions across the interface. These conditions represent continuity of the solution and satisfaction of the conservation laws across the interface and are of the form:

$$
\begin{aligned}
u^{(E)} &= u^{(I)} \\
F^{(E)}_i &= F^{(I)}_i \\
A^{(E)}_i &= A^{(I)}_i \\
F^{(E)V} &= F^{(I)V}_n
\end{aligned}
\tag{5.25}
$$

where index n refers to the outward normal for the corresonding region ($n^{(E)} = -n^{(I)}$). The continuity requirement pertains also to the test function, so that $v^{(E)} = v^{(I)} = v$. If the variational statement is formulated for this problem, then in addition to interior integrals for each subdomain and regular boundary integrals, jump integrals across the interface show up

in the formulation. These additional interface terms on the right–hand side are of the form:

$$\int_{\partial\Omega_{IE}} \quad -\Delta t \left[F_n^{(I)n} + F_n^{(E)n} \right] \cdot v + \Delta t \left[F_n^{(I)Vn} + F_n^{(E)Vn} \right] \cdot v$$

$$+ \frac{\Delta t^n}{2} \left[\left(1 - 2\alpha^{(I)} \right) A_n^{(I)} F_{J,J}^{(I)n} + \left(1 - 2\alpha^{(E)} \right) A_n^{(E)} F_{J,J}^{(E)n} \right] \cdot v ds$$

It can be easily shown that the first two terms are zero because of the interface conditions (5.25). On the left–hand side of the variational formulation additional interface terms are of the form:

$$\int_{\partial\Omega_{IE}} \Delta t \left[\alpha^{(I)} A_i^{(I)n} \Delta u^{(I)} n_i^{(I)} + \alpha^{(E)} A_i^{(E)n} \Delta u^{(E)} n_i^{(E)} \right] \cdot v$$

$$- \Delta t \left[\gamma^{(I)} \left(R_{ij}^{(I)} \Delta u_{,j}^{(I)} n_i^{(I)} + P_i^{(I)} \cdot \Delta u^{(I)} n_i^{(I)} \right) + \gamma^{(E)} \left(R_{ij}^{(E)} \Delta u_{,j}^{(E)} n_i^{(E)} + P_{,J}^{(E)} \Delta u^{(E)} n_i^{(E)} \right) \right] \cdot v$$

$$- \frac{\Delta t^2}{2} \left[\left(1 - 2\alpha^{(I)} \right) \beta A_i^{(I)} A_j^{(I)} \Delta u_{,j}^{(I)} n_i^{(I)} + \left(1 - 2\alpha^{(E)} \right) \beta^{(E)} A_i^{(E)} A_j^{(E)} \Delta u_{,j}^{(E)} n_i^{(E)} \right] \cdot v ds$$

or, after reinterpretation of the linearized terms:

$$\int_{\partial\Omega_{IE}} \Delta t \left[\alpha^{(I)} \Delta F_n^{(I)} + \alpha^{(E)} \Delta F_n^{(E)} \right] \cdot v - \Delta T \left[\gamma^{(I)} \Delta F_n^{(I)V} - \gamma^{(E)} \Delta F_n^{(E)V} \right] \cdot v$$

$$- \frac{\Delta t^2}{2} \left[(1 - 2\alpha^{(I)}) \beta^{(I)} A_n^{(I)} \Delta F_{J,J}^{(I)} + (1 - 2\alpha^{(E)}) \beta^{(E)} A_n^{(E)} \Delta F_{J,J}^{E} \right] \cdot v ds$$

In the above formula, natural interface conditions should be imposed on the viscous, second–order and artificial dissipation terms. Unfortunately, basic conditions (5.25) are not directly applicable to the viscous terms because of different coefficients for the implicit and explicit terms. Even more questionable are the relevant natural interface conditions for the terms resulting from the second–order expansion in time. At present, we do not have reasonable propositions of the conditions to be applied. It can be observed, however, that all the terms considered here are at least of the order of Δt^2, so that setting them all to zero preserves the first–order time accuracy of the scheme. This is the approach adopted subsequently in the implementation of this procedure.

Procedure III

The last procedure considered here is based on a generalization of the weak formulation, according to which the implicitness parameters are not constant, but are continuous functions of the position x. For the finite element computations it is convenient to limit the choice of these parameters to the finite element subspace, so that:

$$\alpha(x) = \sum_{I+1}^{N} \alpha_I \Psi_I(x)$$

45

and the same holds for the other implicitness parameters β, γ and δ. With this assumption the weak formulation was derived for the domain Ω. The resulting formula is of the form (5.14) with additional terms on the left-hand side:

$$\int_\Omega \quad - \quad \Delta t \alpha_{,i} A_i^n \Delta u \cdot v$$

$$+ \quad \Delta t \left(\gamma_{,i} R_{ij}^n \Delta u_{,j} + \gamma_{,i} P_i^n \Delta u \right) \cdot v$$

$$- \quad \frac{\Delta t^2}{2} \left[((1 - 2\alpha)\beta)_{,i} \, A_i^n A_j^n \Delta u_{,j} \right] \cdot v d\Omega$$

and on the right-hand side:

$$\int_\Omega \frac{\Delta t^2}{2} \alpha_{,i} A_i^n F_{j,j}^n \cdot v d\Omega$$

From these equations, the formulas for additional contributions to the stiffness matrix and the right-hand side can be easily derived. The artificial dissipation contributions, not presented here, are handled in exactly the same way as the natural viscosity. Note that there are no additional boundary terms resulting from the variable implicitness.

The above approach seems to be the most general and clear, with no ambiguities concerning the interface conditions. To make the practical application cheaper, the implicitness coefficients are held constant in most of the elements, and the additional terms are actually evaluated only in the transition zones.

5.6.2   Selection of Implicit and Explicit Zones

The basic criterion for selection of implicit and explicit zones is simple: for a given time step all nodes which violate the stability criterion for an explicit scheme should be treated with the implicit scheme. According to this criterion, several options for an automatic adaptive selection of implicit/explicit zones were implemented:

1. User-prescribed time step DT:

   Within this option the user prescribes the time step. All nodes satisfying stability criterion for the explicit scheme (with some safety factor) are explicit. This means that all the elements connected to these nodes are treated with the explicit scheme. On all other elements the implicit scheme is applied.

2. Prescribed maximum CFL number:

   In this option the user prescribes the maximum CFL number that can occur for elements in Ω. The time step is automatically selected as the maximum step satisfying

46

this condition. The choice of maximum CFL number may be suggested by the time accuracy arguments or the quality of results (it is known that for Taylor-Galerkin scheme too large a CFL number tends to smear shocks—see Section 6.3).

3. Prescribed percentage of the domain is implicit.

In this version the user specifies the fraction of the domain which is to be treated implicitly. The nodes with the strongest stability limitation (usually the smallest ones) are treated implicitly, the others are explicit. The time step is selected to guarantee stability of the explicit zone.

4. Minimization of the cost of computations.

In this option the time step and the implicit/explicit subzones are selected to minimize the cost of advancing the solution in time (say one time unit). The algorithm is based on the fact that for an increased time step an increasing number of elements must be analyzed with the (expansive) implicit algorithm. The typical situation is presented in Fig. 19, which shows for different time steps the relative number of nodes that must be treated with the implicit scheme (to preserve stability). On the abscissa the Δt_{FE} denotes the longest time step allowable for the fully explicit scheme (with some safety factor). Δt_{FI} denotes the shortest time step requiring a fully implicit procedure. The number of implicit nodes increases as a step function from zero for $\Delta t \leq \Delta t_{FE}$ to one for $\Delta t \geq t_{FI}$. Now assume that the ratio r of the computational cost of processing one implicit node to the cost of processing one explicit node is given (including the time of solving the system of equations). This ratio is, in general, a function of the number of implicit and explicit nodes. Then the reduction of the cost of advancing the solution in time with the implicit/explicit scheme, as compared to the fully explicit scheme, is given by the formula:

$$R = \frac{\Delta t_{FE}}{\Delta t} \left(n^{(E)} + r n^{(I)} \right)$$

Typical plots of the function $R(t)$ are presented in Fig. 19. Shown here are the two cases:

(a) the case of a small difference between fully explicit and fully implicit time steps— an almost uniform mesh

(b) the case of a large difference between fully explicit and fully implicit time steps

Before discussing these plots it should be noted that certain restrictions on the length of the time step should be applied, for example, from the maximum CFL condition. Otherwise the cheapest procedure would always be to reach the final time with one implicit step.

From the plots in Fig. 19 the following observation can be made: for an almost uniform mesh the mixed implicit/explicit procedure does not provide savings of the computational cost—either a fully implicit or fully explicit scheme is the cheapest depending on the time step restriction. On the other hand, for very diverse mesh sizes the mixed procedure provides considerable savings. This means that the effectiveness of the mixed implicit/explicit scheme will be the best for large–scale computations with adaptive meshes, especially problems with very thin boundary layers. Some introductory results are presented in Section 6.3. In the practical implementation of this method, the approximation to the function $R(\Delta t)$ is automatically estimated for a given mesh. Then, the time step corresponding to the smallest $R(\Delta t)$ is selected automatically (subject to some constraints, in particular the CFL_{max} constraint).

In addition to the above few criteria, based purely on a stability analysis, some other criteria for application of implicit schemes can be applied. For example, within boundary layers the implicit scheme may be preferred, because it provides faster convergence of the boundary fluxes and offers direct control of the natural boundary conditions. Many of these issues are yet to be experimented with.

5.6.3 Computational Procedure

In the numerical solution of the Navier-Stokes equations the implicit/explicit procedure is combined with an adaptive finite element mesh refinement scheme, as described in references [28,29]. The range of implicit/explicit zones is redefined after every mesh refinement and—between refinements—after every prescribed number of steps. At every time step the implicit/explicit procedure results in a system of equations:

$$(M + K^{(I)})\Delta U = R \tag{5.26}$$

where the stiffness matrix K has non–zero entries only for degrees of freedom in the implicit zone or for nodes with penalty–enforced boundary conditions. The solution procedure for the above system differs significantly depending whether the consistent or lumped mass matrix is used.

If the mass matrix is lumped (diagonal), then the solution is performed in two steps:

1. calculate the solution for all explicit degrees of freedom by a simple one–pass Jacobi procedure.

2. solve the linear system of equations for the implicit degrees of freedom. Currently the two solvers are available:

48

- direct frontal solver (for testing purposes),

- truncated-restarted GMRES method with block-Jacobi preconditioning and an element-by-element data structure. Other preconditioners are currently being tested.

Note: nodes with out-of-diagonal penalty terms. like for example the ones on the solid wall, are formally classified as implicit and dealt with at this stage.

If the mass matrix is consistent. then in spite of the application of the explicit scheme. the system of equations is implicit (all degrees of freedom are coupled). Thus. the preconditioned GMRES procedure is used for the whole system (5.26).

It can be observed that the implicit/explicit procedure is computationally much more effective if the lumped mass matrix is used. The explicit degrees of freedom are eliminated at very low cost and the same workspace can be used for explicit and implicit computations. The consistent mass matrix introduces full coupling of degrees of freedom within the domain Ω. Although the coupling due to the mass matrix is rather weak and would require just a few iterations. full consistency of the solver requires iterating in the explicit zone as many times as in the implicit zone. This considerably increases the cost of solution of the system of equations. especially if the implicit subzone is relatively small.

5.7 Computation of Aerothermal Loads

An essential task in the numerical analysis of hypersonic fluid-structure interactions is a precise calculation of boundary quantities. in particular fluid pressure. skin friction and heating rates. These quantities contribute to the mechanical and thermal loads exerted by the fluid on the structure.

5.7.1 Boundary Fluxes

Evaluation of aerothermal loads requires the computation of flux across the boundary Γ of the fluid domain Ω. namely:

$$F_n = F_i n_i \qquad i = 1.2 \tag{5.27}$$

where F_n is the flux vector across the boundary. n is the outward normal to the boundary Γ and F_i are flux vectors in directions of the global coordinate axes x_i (see Fig. 5). Each of these vectors can be presented as a composition of inviscid and viscous fluxes.

$$F_i = F_i^C - F_i^V$$

with components of the vectors F_i and $F_{V_i}^V$ given in equation (5.4).

The normal flux can also be decomposed into inviscid and viscous parts:

$$F_n = F_n^C - F_n^V \tag{5.28}$$

which, after application of equation (5.27), are represented as:

$$F_n^C = \left\{ \begin{array}{l} \rho v_n \\ \rho u_1 v_n + p n_1 \\ \rho u_2 v_n + p v_2 \\ (\rho E + p) u_n \end{array} \right\}$$

$$\tag{5.29}$$

$$F_n^V = \left\{ \begin{array}{l} 0 \\ t_1^V \\ t_2^V \\ v_k t_k^V - q_n \end{array} \right\}$$

where v_n denotes normal outward velocity and t_i^V are components of the boundary traction due to viscous forces.

The consecutive components of the normal flux vector F_n can, in general, be interpreted as mass flux, x_1-momentum flux, x_2-momentum flux and total energy flux across the boundary.

On a **solid wall**, which is of primary interest in our analysis, the components of the velocity vector vanish, and the total boundary flux is:

$$F_n \Big|_{\text{solid wall}} = \left\{ \begin{array}{l} 0 \\ p n_1 - t_1^V \\ p n_2 - t_2^V \\ q_n \end{array} \right\} \tag{5.30}$$

In this case the total normal pressure on the wall $\hat{p}$ and the value of the skin friction τ are calculated as projections of the x_1 and x_2-momentum fluxes on vectors n and s, which are normal and tangent to the boundary, respectively:

$$\hat{p} = F_{n(2)} n_1 + F_{n(3)} n_2 = p - \sigma_{nn}^V$$

$$\tau = F_{n(2)} s_1 + F_{n(3)} s_2 = -\sigma_{ns}^V$$

Note that the normal pressure on the wall is, in general, different than the thermodynamic pressure. It can be verified that in laminar, fully developed boundary layers viscous contributions to the normal pressure σ_{nn}^V vanish, but they can be significant in other cases, like the shock–boundary layer interaction.

Regarding practical evaluation of boundary fluxes in the finite element method, there are two basic approaches, namely:

50

- calculation from the definition.

- consistent finite element calculation.

The calculation from the definition is straightforward and reduces to a pointwise application of formula (5.4). The necessary gradients of components of velocity and the temperature are calculated using the finite element shape functions. Since these gradients are discontinuous across element boundaries. the nodal values of boundary fluxes can be obtained by averaging of the values from the adjacent element sides (or by other postprocessing procedures).

The calculation of boundary fluxes from the definition has. for most commonly used linear or bilinear elements. poor accuracy (first order in space). More precise results. corresponding approximately to the application of second order schemes in the finite difference method. can be obtained from a consistent finite element recovery. This method will be presented in the next section.

5.7.2 Consistent Computation of Boundary Fluxes

The basis for a consistent calculation of boundary fluxes is the weak formulation of the Navier-Stokes equations. written in the form:

$$\int_\Omega \dot{u} \cdot v d\Omega - \int_\Omega F_i \cdot v_{,i} d\Omega + \int_{\partial\Omega} F_n \cdot v ds = 0 \qquad \forall \, v \in V \qquad (5.31)$$

where V is the space of test functions (usually a subspace of $H^1(\Omega)$).

Suppose that the domain Ω was discretized with finite elements. the approximate solution of equation (5.31) was obtained and we want to calculate boundary fluxes F_n across a certain section of the boundary Γ_F (see Fig. 6).

The general idea is to reformulate equation (5.31) in the form:

$$\int_{\Gamma_F} F_n \cdot v dS = -\int_\Omega \dot{u} \cdot v d\Omega + \int_\Omega F_i v_{,i} d\Omega - \int_{\partial\Omega - \Gamma_F} F_n \cdot v dS \qquad (5.32)$$

The test functions in this equation are arbitrary linear combinations of nodal shape functions Ψ_I. For the purpose of calculating fluxes on Γ_F it suffices to restrict the domain Ω to the subdomain $\overline{\Omega}$. which is the set of elements covered by shape functions associated with nodes on the boundary Γ_F (hatched areas in Fig. 21). Then the test functions considered are of the form:

$$v(x) = \sum_{I=1}^{N_F} V_I \Psi_I(x) \qquad (5.33)$$

Thus equation (5.32). after using the fact that $v = 0$ for the boundary $\overline{\Gamma}$. takes the form:

$$\int_{\Gamma_F} F_n \cdot v dS = -\int_{\overline{\Omega}} \dot{u} \cdot v d\Omega = \int_{\overline{\Omega}} F_i \cdot v_i d\Omega - \int_{\overline{\Gamma}_0} F_n \cdot v dS \qquad (5.34)$$

51

Introducing the finite element approximation of fluxes along the boundary Γ_F

$$F_n(x) = \sum_{I=1}^{N_F} F_{nI} \Psi_J(x)$$

and requiring that equation (5.34) be satisfied for every test function. leads to the following linear system of equations:

$$M_{IJ} F_{nJ} = R_J$$

In the above. M is the "mass" matrix for the boundary F_F:

$$M_{IJ} = \int_{\Gamma_F} I_{4\times4} \Psi_I \Psi_J dS$$

where $I_{4\times4}$ represents unit matrix of size 4×4. For simplicity. a lumped mass matrix can also be used. The right–hand size vector is calculated according to the formula:

$$R_J = \int_{\overline{\Omega}} -\dot{u}\Psi_J + F_i \Psi_{J,i} d\Omega$$

$$- \int_{\overline{\Gamma}_0} F_n \Psi_J dS$$

Note that it is essential to include in the calculation of the right–hand sides the contribution of boundary terms on $\overline{\Gamma}_0$. If these terms are neglected. then incorrect values of fluxes are calculated near both ends of Γ_F. The necessary fluxes F_n on $\overline{\Gamma}_0$ are calculated in the same way as the fluxes F_i inside $\overline{\Omega}$. namely using definition (5.27) and the gradients calculated from finite element shape functions.

It is important to observe that the application of artificial dissipation models (like Lapidus dissipation) introduces additional terms into the equation (5.31). These terms give rise to artificial boundary fluxes. which have no physical interpretation. Thus. including these terms in computations yields results of no physical meaning. On the other hand. neglecting these terms in heat flux computations violates satisfaction of the weak form of the conservation laws (5.31). so the calculated heat fluxes are **not** consistent with the finite element solution. Therefore. the conclusion is that. for the purpose of a proper evaluation of boundary fluxes. the artificial dissipation should not be used in the vicinity of a solid wall (at least in the present form (5.15) or (5.16)).

6   Selected Validation Examples

In order to better understand phenomena of hypersonic interactions and to validate the methods and software developed in the project. several test problems were solved. The problems

selected were usually rather simple. so that experimental results. analytical solutions, or solutions obtained by other researchers could be identified for comparison. Most of these validation examples were presented in consecutive progress reports and will not be repeated in this report. However. in order to illustrate the correctness of the proposed formulation. methods and software, some of these results will be briefly summarized. Moreover. recent examples of implicit/explicit flow computations will be presented in this section.

6.1 Validation of Thermo–Viscoplastic Analysis

The first simple verification test of the viscoplastic constitutive equations is the simple tension test at elevated temperatures. performed for a superalloy B1900 +Hf under the NASA HOST program [5.6]. As indicated in Fig. 22. at 1800°F the elastic section of a stress–strain curve is very short and the difference between elastic and viscoplastic solutions is very significant. The predictions of the Bodner-Partom unified viscoplastic theory correspond very well to experimental results.

To verify the characteristics of the thermo–viscoplastic constitutive models under more complex load histories. the stress–strain response of a bar due to specified cyclical variations of the strain rate was analyzed. Figure 23 presents a statement of the problem. and Fig. 24 shows the stress–strain response of the bar for different temperatures. Significant points to note are that with increasing temperature. the reduction in elastic modulus and yield stress are correctly represented by the unified viscoplastic theory. The above results compare favorably with experimental observations for nickel superalloy B1900 +Hf.

6.2 Validation of Large Displacement Formulation

The large displacement extension was introduced into the theory and software in order to properly capture the beam–column effect due to localized heating of hypersonic structures. To validate this modification and to verify the adequacy of the finite element model. an elastic beam–column problem was analyzed. The problem statement is presented in Fig. 25. A simply supported beam is subjected to a sudden increase in surface heating on its upper surface. The lower surface of the beam is adiabatic. The heating which is uniform over the upper surface of the beam induces a time–varying temperature variation through the beam depth. For supports fixed against horizontal displacement. the beam experiences an increasing axial compressive force. At the same time. the temperature gradient through the depth induces a thermal moment. and so the beam displaces transversly as a beam–column. The elastic beam–column problem has a closed–form analytical solution that can be used to validate the finite element analysis.

53

The particular data used in this analysis were

$$Q = 6.0 \text{ BTU/s-in}^2$$
$$\rho = 0.283 \text{ lb}_m/\text{in}^3$$
$$c = 0.20 \text{ BTU/lb}_m - R$$
$$k = 4.16 \cdot 10^{-3} \text{ BTU/in-sec} - R$$
$$E = 1.47 \cdot 10^5 \text{MPa}$$
$$\nu = 0.1$$
$$\alpha = 0.8611 \cdot 10^{-5} \, 1/R$$

where Q is the prescribed heat flux. ρ is the density of a material. c is the thermal capacitance. k is the thermal conductivity. E is the elastic modulus. ν is the Poisson's ratio. and α is the thermal expansion coefficient.

The above problem was solved using three different finite element structural models. These models and deformed configurations of the beam at $t = 1.0s$ are shown in Fig. 26.

A comparison of the finite element solutions with the beam–column theory is presented in Fig. 27. Axial force versus transverse deflection predictions for the three finite element solutions are compared with the theory. The results for the most refined mesh validate the finite element large displacement theory. The results also show that the cruder meshes predict too large an axial force with forces becoming higher than the Euler buckling load as the deflection increases (errors in deflection of the beam were relatively small-order of a few percent).

6.3 Validation of Damage Modeling

To gain insight into behavior of a viscoplastic structure with damage represented in the constitutive equations a simple model was analyzed (Fig. 28). The model was subjected to ten consecutive tension–compression cycles of strain for three specified temperature levels. The properties of the material correspond to the superalloy B19000 +Hf as presented in Refs. [5] and [6].

Figure 29 shows stress–strain curves with damage evolution for three temperature levels. At the lower temperature levels and for the prescribed range of strain rates. there is little apparent effect of the damage. but at the higher temperature (1900° C) there is gradual reduction in the yield stress with increasing strain cycles.

6.4 Implicit/Explicit Analysis of Compressible Flow

Several examples of compressible flow were solved using the implicit/explicit algorithm developed in Section 5. The purpose of these analyses was to verify the performance of the scheme as well as to compose explicit and implicit versions of the algorithm and to identify possible indicators for the selection of implicit and explicit subzones.

Several different examples were solved with various selections of parameters. Some of these examples will be presented in this report.

6.4.1 A Shock Tube Problem

A shock tube problem is a good verification example for transient algorithms. A tube of length 50 is divided by a diaphragm into two sections. with fluid at rest at the following values of density and pressure:

$$\begin{aligned} \rho_1 &= 10.0 & p_1 &= 7.1429 \\ \rho_2 &= 1.0 & p_2 &= 0.71429 \end{aligned}$$

After the diaphragm is removed. the transient flow developes with such phenomena as a shock. a contact region and an expansion region.

The above problem was solved with different combinations of parameters and the results were compared with the analytical solution. The comparison of the density distribution after 100 time steps with a CFL = 0.25 (total time 13.16S) for selected combinations of input parameters are presented in Fig. 30. The general conclusion of these (and other) results are:

- with small time steps (CFL < 1) the explicit and implicit algorithms give the same results.

- for small time steps (CFL < 1) artificial dissipation is necessary to suppress oscillations of the solution.

- larger time steps (CFL > 5) combined with artificial dissipation tend to excessively smear discontinuities. and

- for larger time steps (CFL > 5) no explicit artificial dissipation is necessary to suppress excessive oscillations of the solution (except for the diaphragm zone in this example).

6.4.2 Inviscid Compression Corner

Another typical test problem is a steady state solution of a compression corner. The particular flow considered is that of Mach 3 and the ramp angle 16°. The problem was solved using adaptive refinement techniques with fully implicit and explicit versions of the algorithm. The results obtained with both these versions at the same time step (CFL = 0.5) are practically the same. The refined mesh and density contours are presented in Fig. 31. It can be observed that the algorithm developed in this work does not generate any artificial shock reflections on the outflow boundary (typical for many implementations of Taylor-Galerkin or Lax-Wendroff algorithms).

The next figure presented is the solution obtained with implicit algorithm for CFL = 10 with no explicit artificial dissipation. It can be observed that although some oscillation of the solution can be observed, the shock is captured within two elements. This result confirms the fact that, for larger time steps, the algorithmic diffusion due to second-order terms is sufficient to suppress spurious oscillations and there is no need for explicit artificial dissipation.

6.4.3 Boundary Layer Problem

To analyze the behavior of implicit and explicit schemes in the boundary layer the supersonic boundary layer problem shown in Fig. 33 was solved. The problem consists of specifying inflow profiles of conservation variables and computing profiles at downstream locations by solving the Navier-Stokes equations. The data chosen is representative of a supersonic flow, and the temperature profiles (Fig. 34) are reprsentative of flows that induce aerodynamic heating. As indicated by the computations presented in previous reports, the artificial dissipation has to be "turned off" in the boundary layer in order for heating rates to be predicted properly. Recently this problem was solved with the implicit algorithm at different time steps. The general conclusion is that within the boundary layer the heating rates with large time steps (CFL numbers up to 500) are virtually the same as for small time steps.

6.4.4 Flat Plate Problem

The problems presented so far were solved using the fully explicit or fully implicit version of the algorithm. As a test problem for the implicit/explicit procedures, a classical flat plate problem solved originally by Carter was analyzed. The problem statement for this problem is presented in Fig. 35, the density contours corresponding to the steady state solution are presented in Fig. 36, and the nondimensional heating rates on the wall calculated as $q^* = q/\rho_\infty c_\infty^3$ are presented in Fig. 37.

In the solution of the problem the implicit/explicit algorithm was used. The selection of implicit and explicit zones was based on the minimization of the cost of computations with the limitation on the time step: CFL < 5.0. The safety coefficient for the explicit method was equal 0.7. For the mesh presented in Fig. 36, the automatically selected nondimensional time step was equal 4.17073, which corresponds to CFL = 1.95. The number of explicit elements was equal 1327 and the number of implicit elements was equal 90. For these parameters the cost of advancing the solution in time was 1.6 times cheaper than with the fully explicit scheme and about ten times cheaper than the fully implicit scheme.

The above analysis, although performed with a very conservative restriction on the time step, confirms the effectiveness of adaptive implicit/explicit scheme in the solution of Navier-Stokes problems. Further experiments are necessary to refine the criteria for implicit/explicit calculations and further increase the effectiveness of this approach.

The flat plate example was solved primarily to test the implicit/explicit procedure with no special emphasis placed on obtaining the best quality results. It can be seen, however, that for the present mesh the general flow phenomena and boundary conditions are properly resolved. In particular, the fine mesh near the tip of the plate satisfactorily captures the singular character of the solution. However, a few critical remarks about these results are appropriate here:

- The automatic mesh refinement procedure based on the density error estimate does not sufficiently refine the boundary layer region. More general error estimators, including velocity gradients, have recently been implemented to resolve this problem.

- The heating rate plot shows some disturbance in the smoothness of the graph at points of changing element size. This is due to the application of artificial dissipation throughout the whole computational domain. Since the significance of the artificial dissipation—as compared with natural dissipation—depends on the mesh size, the rapidly varying element size results in a disturbance of the heating rates. As indicated in the previous section, a proper computation of the heating requires the "turning of" the artificial dissipation in the boundary layer (or extremely small elements).

It should be emphasized at this point, from an examination of the right-hand side of the variational formulation (5.14), *that a steady state solution for a given time step does not depend on the implicitness or explicitness of the solution algorithm* (for unconditionally stable versions of the implicit scheme). The only exceptions are boundaries with prescribed natural boundary conditions, where the implicit algorithm provides direct control of the fluxes.

57

7 Thermo-Viscoplastic Analysis of a Convectively Cooled Structure

A more realistic two-dimensional model of a convectively cooled hypersonic structure is shown in Fig. 38. The model represents a segment of a convectively cooled structure such as a wall of a scramjet engine fuel injection strut. The finite element thermal model (Fig. 38) includes: (1) conduction heat transfer in the aerodynamic skin, heat exchanger fins and a primary structure. (2) convective heat transfer between the walls of the coolant passage and coolant. (3) mass transport convection in the coolant which has an unknown bulk temperature, and (4) surface radiation on the aerodynamic skin. The aerodynamic skin is uniformly convectively heated over its length, and superimposed on the uniform heating is a local, intense heating simulating a transient shock. The transient heating is induced by the time-dependent convection coefficient shown in Fig. 38.

In the plane strain structural finite element model, the primary structure and aerodynamic skin have unit thickness, but the heat exchanger fins in the coolant passage are approximately represented by a single fin with the total thickness of 0.060. The wall segment has fixed displacement boundary conditions at the left and right ends. The aerodynamic skin, exchanger fins and primary structure are also loaded by internal pressure (7.0 MPa = 1000 psi) in the coolant passage which is relatively large compared to external aerodynamic pressure (0.35 MPa = 50 psi).

The model was analyzed first for steady aerodynamic heating and internal pressure operating conditions. Then the sudden localized aerodynamic heating was applied. Thus, the steady temperatures and stresses serve as initial conditions for the transient thermo-viscoplastic ana. sis.

The viscoplastic solution was computed with the variable time step algorithm. A total of 265 steps were required to compute the response for a total time duration of 1.2 s.

The thermal response of the wall segment is shown in Fig. 39. Figure 39b shows the time history of the temperature at a point on the aerodynamic skin directly under the transient heating: Fig. 39a shows contours of temperatures at $t = 0.5s$ when temperatures are maximum. The temperature history is qualitatively similar to the results obtained in the one-dimensional model showing the rapid skin temperature rise and fall with the simulated shock heating. The temperature contours show relatively steep thermal gradients induced by the local heating, and that the coolant substantially limits the extent of the induced high temperatures. Thus the high temperatures are confined to the aerodynamic skin, and the primary structure experiences only small temperature changes. The temperature gradients in the skin particularly at the coolant-skin interface are not predicted with high accuracy because of the engineering model of the coolant heat transfer. However, local temperature

58

levels in the skin are reasonably accurate since the net energy transfer to the coolant is modeled satisfactorily.

Histories of the horizontal stress component σ_x at two points through the skin thickness are shown in Fig. 40. The stress histories follow the temperature, and under the intense local heating stresses are very similar to the results obtained from the one-dimensional model. At this location the skin yields through most of its thickness. After the heating ceases there is a rapid decay of stress, and under the intense local heating there are residual tensile stresses. Figure 41 shows the time history of the vertical component of stress σ_y in the heat exchanger fins. High tensile stresses are induced with significant local yielding which is followed by residual compressive stresses. The crude finite element model of the fins only approximates these stresses, but the high tensile stresses can potentially cause a bond failure at the heat exchanger/skin joint. The consequences of such a failure are studied in the next example.

The viscoplastic stress histories are compared with stresses predicted assuming an elastic behavior in Figs. 42 and 43. The elastic computations were made with temperature-dependent elastic properties. The loss of stiffness due to the elevated temperatures for $0.1f < t < 0.5s$ accounts for the stress "rolling-over" with an appearance of yielding. Generally, the elastic stresses are too high and, of course, since yielding does not occur residual stresses are not predicted. Maximum deformations (not shown) predicted by the elastic analysis and viscoplastic analysis are about the same, approximately 0.001 in.

The two-dimensional character of the stress components σ_x and σ_y are shown in Figs 44 and 45, respectively. The stress distributions are shown at three times $t = 0.05s$, $0.5s$, $1.2s$ in the response. The stresses at $t = 1.2s$ are the residual stresses. Figure 46 shows contours of the principal plastic strains at $t = 0.5s$. The contours show the relatively localized nature of the high stress gradients as well as the tensile and compressive regions. The significant residual stresses suggest the possibility of cumulative damage under repeated load cycles. This possibility needs further investigation.

Convectively Cooled Structure With Damage

The preceding analysis showed high tensile stresses in the heat exchanger fins and suggested the possibility of an aerodynamically skin/heat exchanger bond failure. To simulate such a possibility, the analysis was repeated but with the fins given greatly reduced material properties for a width of 0.30 in. under the high localized heating. Two results of this analysis are shown in Figs 47 and 48.

Since the fins can no longer support tensile stress, the internal coolant pressure and the beam–column effect causes substantial local deformation of the aerodynamic skin. Figure 47 shows the deformed structure at $t = 0.5s$. Compared are the solutions obtained with small

deformation and large deformation theory. Deformations are shown to scale. and the figure shows that the large displacement formulation predicts larger displacements. This comparison is made quantatively in Fig. 48. Viscoplastic displacement histories are compared on the aerodynamic skin for: (1) fins without debonding, (2) fins with debonding as predicted by the infinitesimal formulation. and (3) fins with debonding as predicted by the large displacement formulation. The results clearly show that the large displacement formulation is required.

8 Conclusions

In the course of this project considerable progress was made towards the understanding of complex phenomena of flow–thermal and structural interactions in hypersonic flight and towards reliable methods of numerical modeling of these phenomena. The result of the project is a unique computational capability for modeling hypersonic flow, prediction of aerothermal loads and a thermo–viscoplastic analysis of the structural response.

The numerical analysis of all three components of the interaction problem (flow. thermal. and structural) is based on the finite element method, thus providing full compatibility and coupling of these analyses. To guarantee efficient computations and reliable results. the software is equipped with adaptive mesh refinement, adaptive time step selection. and adaptive implicit/explicit procedures. based on relevant error and cost estimates.

An analysis of a two–dimensional model of a realistic convectively cooled structure provided more detailed understanding of the thermal–structural behavior. The coolant flow dominates the thermal response providing a relatively short thermal transient. Under intense heating, significant local plasticity occurs in the aerodynamic skin. but the primary structure remains undamaged. Heat exchanger fins experience high tensile stresses and both the aerodynamic skin and heat exchanger fins have significant residual stresses. An analysis of an aerodynamic skin/heat exchanger fin bond failure showed that the aerodynamic skin would experience significant local plastic deformation due to combined coolant pressure and beam–column effect in the skin. The local deformation is pronounced enough to disturb the external aerodynamic flow and introduce a complex flow-thermal-structural interaction.

The analysis of convectively cooled hypersonic structurs under intense local heating shows the important role that such analyses can make in understanding complex transient inelastic structural behavior at elevated temperatures.

Further progress in the realistic modeling of hypersonic flow–thermal and structural interactions will involve both theoretical. numerical, and experimental analyses. Some of the issues to be resolved are:

1. An experimental verification of thermo–viscoplastic structural analyses. Although the viscoplastic Bodner-Partom equations compare very favorably with experiments for simple stress states, extensive experimental verification is necessary to confirm their adequacy in complex stress states due to localized heating.

2. Further refinement of computational techniques towards maximum efficiency and reliability is needed. The hypersonic interaction problems are—due to combined fluid-thermal-structural analyses and due to their inherent transient nature—computationally very expensive. Further progress toward computational efficiency is necessayr to make realistic three–dimensional analyses feasible.

3. Fast and reliable techniques for coupling of structural deformations with the flow analysis are needed. The issues include moving boundaries, transfer of aerothermal loads, matching of time scales, etc.

4. Constitutive models for describing high–temperature behavior of nonmetallic materials should be developed and implemented. For metallic materials, constitutive relations valid in temperatures near the melting point should be developed.

5. Models and computational techniques for surface reactions, burn-through and other failure phenomena need to be developed and implemented.

6. Extensive numerical analyses and experimental verifications are necessary to enhance the understanding of phenomena of hypersonic interactions and verify the reliability of theoretical models and computational techniques.

Resolution of several of these issues, in particular an experimental verification of thermo–viscoplastic numerical analyses, were planned for the third year of this effort.

9   References

1. Bass. J. M.. "Numerical Implementation of Constitutive Models in Rate–Dependent Plasticity." *Ph.D. Dissertation*. The University of Texas. Austin. 1985.

2. Bass. J. M.. and Oden. J. T.. "Adaptive Finite Element Methods for a Class of Evolution Problems in Viscoplasticity." *Int. J. Eng. Sci.*. Vol. 25. No. 6. pp. 623–653. 1987.

3. Bass. J. M.. and Oden. J. T.. "Numerical Solution of the Evolution Equations of Damage and Rate–Dependent Plasticity," *Int. J. Engng. Sci.*. Vol. 26. No. 7. pp. 713–740. 1988.

4. Bodner, S. R., and Chan, K. S., "Modeling of Continuum Damage for Application in Elastic-Viscoplastic Constitutive Equations," **Engineering Fracture Mechanics.** Vol. 25, Nos. 5-6, pp. 705-712, 1986.

5. Chan, K. S., Lindholm, U. S., Bodner, S. R., Hill, J. R., Weber, R. M., and Meyer, T. G., "Constitutive Modeling for Isotropic Materials (HOST)," Third Annual Status Report, Southwest Research Institute, San Antonio, Texas, NASA CR-179522, August, 1986.

6. Chan, K. S., Lindholm, U. S., and Bodner, S. R., "Constitutive Modeling for Isotropic Materials (HOST), Final Report, Southwest Research Institute, San Antonio, Texas, NASA CR-182132, June, 1988.

7. Chang, H. T., and Allen, D. H., "Analysis of Viscoplastic Plates Subjected to Rapid External Heating," AIAA/ASME/ASCE/AHS 29th Structures, Structural Dynamics and Materials Conference, Williamsburg, Virginia, AIAA Paper 88-2422, April 18-20, 1988.

8. Dechaumphai, P., Thornton, E. A., and Wieting, A. R., "Flow-Thermal-Structural Study of Aerodynamically Heated Leading Edges," AIAA/ASME/ASCE/AHS 29th Structures, Structural Dynamics and Materials Conference, Williamsburg, Virginia, AIAA Paper 88-2245, April 18-20, 1988.

9. Donea, J., "A Taylor-Galerkin Method for Convective Transport Problems," *Int. J. Num. Meth. Engng.*, **20**, pp. 101-119, 1984.

10. Dechaumphai, P., Wieting, A. R., and Thornton, E. A., "Thermal-Structural Performances of an Actively Cooled Leading Edge Subjected to Type IV Shock Wave Interference Heating," Third National Aerospace Plane Symposium, Paper No. 24, June 2-4, 1987.

11. Demkowicz, L., Rachowicz, W., and Oden, J. T., "A New Approach for Solving Navier-Stokes Equations Based on Adaptive Methods and Operator-Splitting," Final Report, Contract NAS 2-13000, NASA Ames Research Center, 1989.

12. Donea, J., Giuliani, S., Laval, H., and Quartapelle, L., "Time-Accurate Solution of Advection-Diffusion Problems by Finite Elements," *Comp. Meth. Appl. Mech. Engng.*, **45**, pp. 123-145, 1989.

13. Donea, J., Quartapelle, J., and Selmin, V., "An Analysis of Time Discretization of the Finite Element Solution of Hyperbolic Problems," *J. Comp. Phys.*, **70**, pp. 463-499, 1987.

14. Dutt, P., "Stable Boundary Conditions and Difference Schemes for Navier-Stokes Equations," *SIAM J. Numer. Anal.*, **25**, 2, pp. 245-267, 1988.

15. Gurtin, M. E., "An Introduction to Continuum Mechanics," Academic Press, 1981.

16. Gustaffson, B., and Sudström, A., "Incompletely Parabolic Problems in Fluid Dynamics," *SIAM J. Appl. Math.*, **35**, 2, pp. 343-357, 1978.

17. Hassan, O., Morgan, K., and Peraire, J., "An Adaptive Implicit/Explicit Finite Element Scheme for Compressible Viscous High Speed Flows," AIAA 27th Aerospace Sciences Meeting, Reno, Nevada, January 9-12, 1989.

18. Huebner, K. H., and Thornton, E. A., **The Finite Element Method for Engineers.** Second Edition. John Wiley and Sons, 1982.

19. Kumar, V., Morjaria, M., and Mukherjee, S., "Numerical Integration of Some Constitutive Models of Inelastic Deformation," *J. Engineering Materials and Technology.* Vol. 102. pp. 92-96, Jan. 1980.

20. Lapidus, A., "A Detached Shock Calculation by Second-Order Finite Differences," *J. Comp. Phys.*, **2**. pp. 154-177, 1967.

21. Lerat, A., "Implicit Methods of Second-Order Accuracy for the Euler Equations," *AIAA Journal.* **23**. 1. pp. 33-40. 1985.

22. Löhner, R., Morgan, K., and Peraire, J., "A Simple Extension to Multidimensional Problems of the Artificial Viscosity Due to Lapidus," *Com. Appl. Num. Meths.*. **1**. pp. 141-147. 1985.

23. Malvern, L. E., "Introduction to the Mechanics of a Continuous Medium," Prentice-Hall. 1969.

24. MARC General Purpose Finite Element Program. MARC Corporation. Palo Alto. CA.

25. Melis, M. W., and Gladden, H. J., "Thermostructural Analysis With Experimental Verification in a High Heat Flux Facility of a Simulated Cowl Lip," AIAA/ ASME/ASCE/ AHS 29th Structures. Structural Dynamics and Materials Conference. Williamsburg. Virginia. AIAA 88-2222. April 18-20. 1988.

26. Miller, A. K. (editor), *Unified Constitutive Equations for Creep and Plasticity.* Elsevier Applied Science Publishers. 1987.

27. Morgan, K., and Peraire, J., "Finite Element Methods for Compressible Flows," von Karman Institute for Fluid Dynamics Lecture Series. 1987-04. 1987.

28. Oden, J. T., Strouboulis, T., and Devloo, P., "Adaptive Finite Element Methods for the Analysis of Inviscid Compressible Flow," *Comp. Meth. Appl. Mech. Engng.*, **59**, pp. 327–362, 1986.

29. Oden, J. T., Strouboulis, T., and Devloo, P., "Adaptive Finite Element Methods for High-Speed Compressible Flows," *Int. J. Num. Meth. Engng.*, **7**, pp. 1211–1228, 1987.

30. Ramakrishnan, R., Thornton, E. A., and Weiting, A. R., "An Adaptive Finite Element Procedure for Compressible Flows With Strong Viscous–Inviscid Interactions," AIAA Thermophysics, Plasmadynamics and Lasers Conference, San Antonio, Texas, June 27–29, 1988.

31. Ramakrishnan, R., Bey, K. S., and Thornton, E. A., "An Adaptive Quadrilateral and Triangular Finite Element Scheme for Compressible Flows, AIAA 26th Aerospace Meeting, Reno, Nevada, Jan. 11–14, 1988.

32. Strikwerda, J. C., "Initial Boundary Value Problems for Incompletely Parabolic Systems," *Ph.D. Thesis*, Dept. of Math., Stanford University, Stanford, CA, 1976.

33. Thornton, E. A., Oden, J. T., Tworzydlo, W. W., and Youn, S. K., "Thermo-Viscoplastic Analysis of Hypersonic Structures Subjected to Severe Aerodynamic Heating," AIAA/ASME/ASCE/AHS 30th Structures, Structural Dynamics and Materials Conference, Mobile, Alabama, April 3–5, 1989.

34. Thornton, E. A., and Wieting, A. R., "Finite Element Methodology for Transient Conduction/Forced Convection Thermal Analysis," *Progress in Astronautics and Aeronautics: Heat Transfer, Thermal Control and Heat Pipes*, Vol. 70, Edited by Walter B. Olstad, AIAA, New York, pp. 77–103.

35. Thornton, E. A., Oden, J. T., Tworzydlo, W. W., and Youn, S. K., "Thermo-Viscoplastic Analysis of Hypersonic Structures Subjected to Severe Aerodynamic Heating," accepted for publication in AIAA Journal in 1989.

36. Truesdell, C., and Noll, W., "The Nonlinear Field Theories of Mechanics," *Handbuch der Physik*, **3**, Berlin, Springer-Verlag, 1965.

37. Wieting, A. R., and Holden, M. S., "Experimental Study of Shock Wave Interference Heating on a Cylindrical Leading Edge," AIAA 22nd Thermophysics Conference, AIAA Paper 87-1511, Honolulu, Hawaii, June 8–10, 1987.
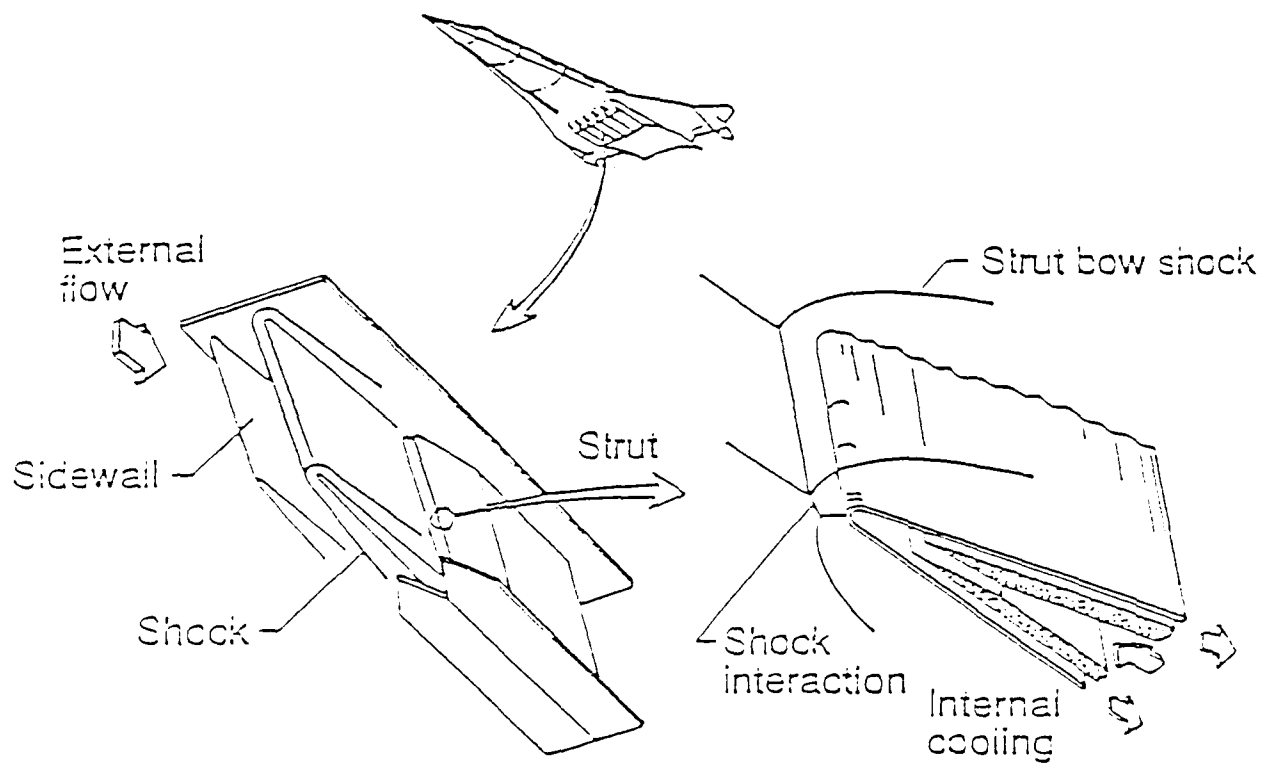
Figure 1: Fluid-thermal-structural interactions on an aerospace plane scramjet engine leading edge.
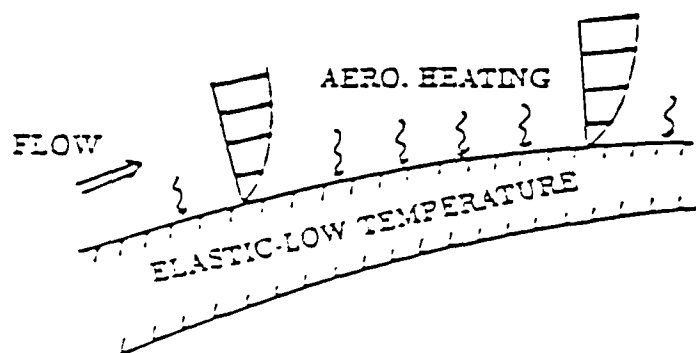
a) Aerodynamic Heating on Undeformed Structure
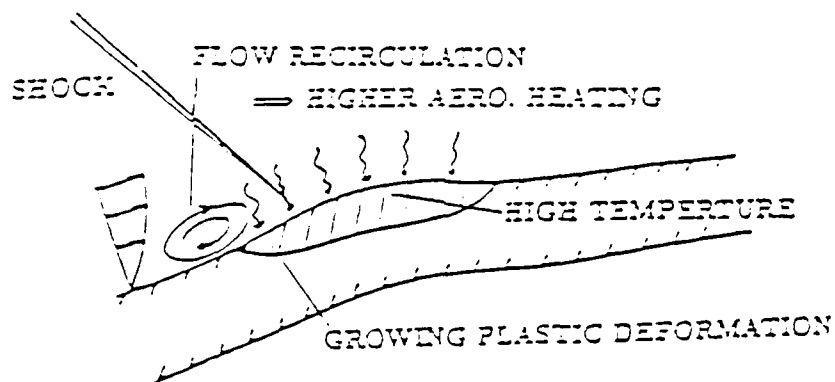
b) Plastic Deformation Induced by High Aerodynamic Heating on Deformed Structure

Figure 2: FTS interactions in hypersonic flight.
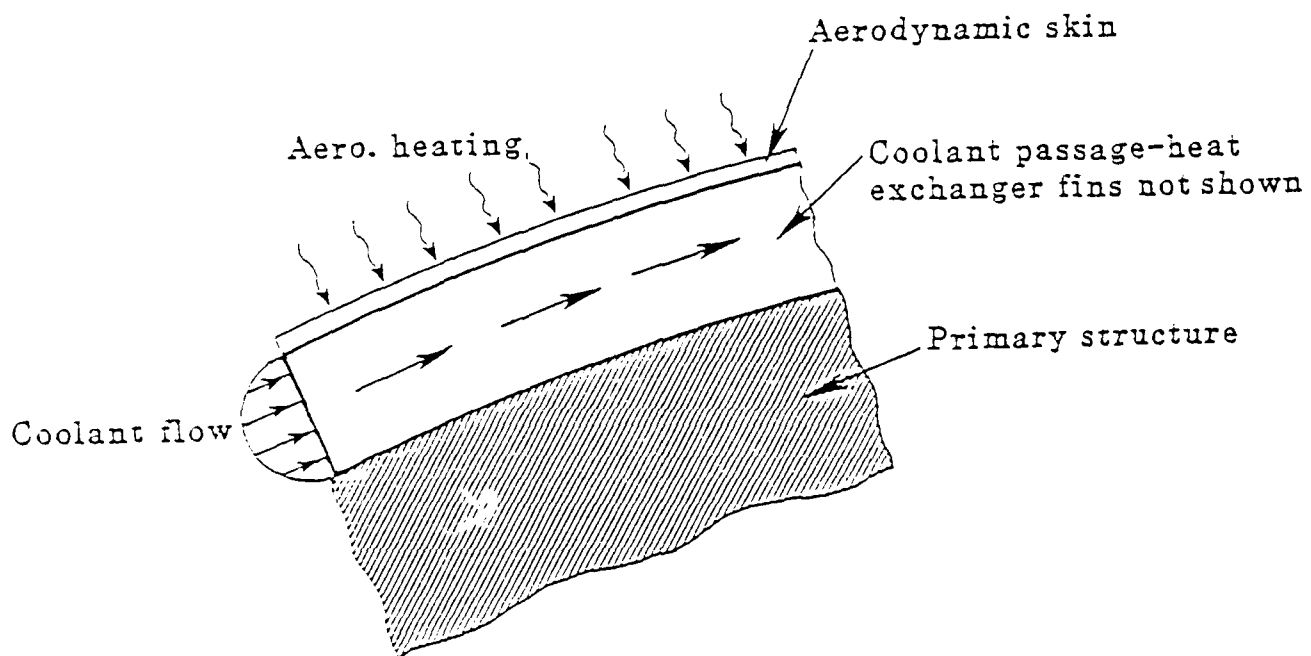
Figure 3: Convectively cooled structure.
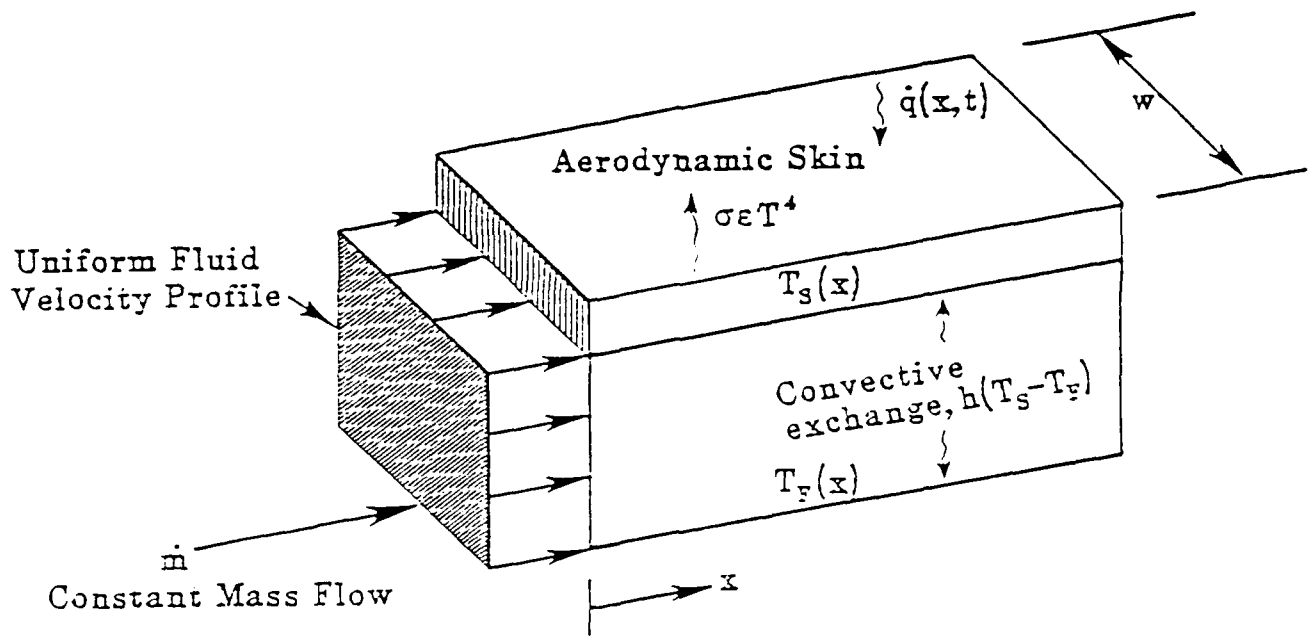
Figure 4: Engineering model of coolant passage heat transfer.
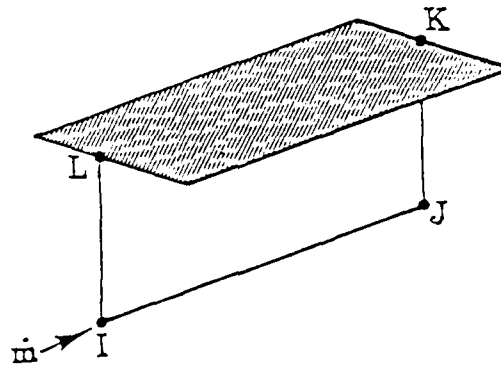
Figure 5: Finite element model of coolant passage.
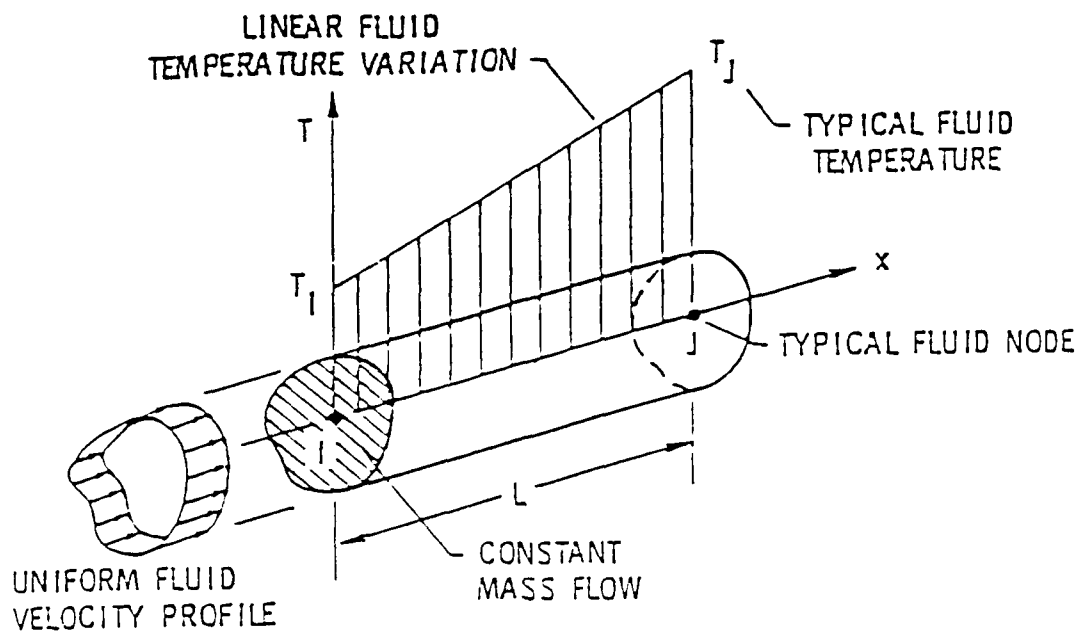
a) mass transport element
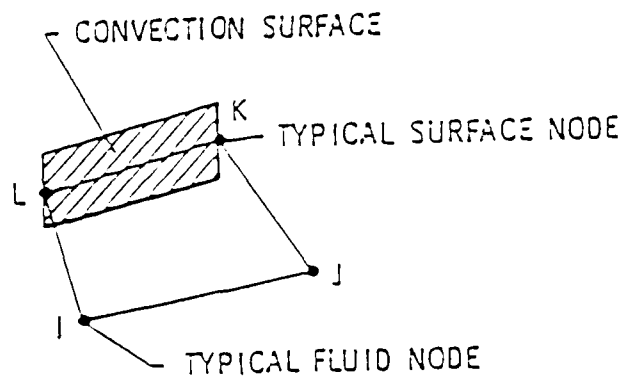
(b) surface convection element

Figure 6: Coolant passage convective elements.

69
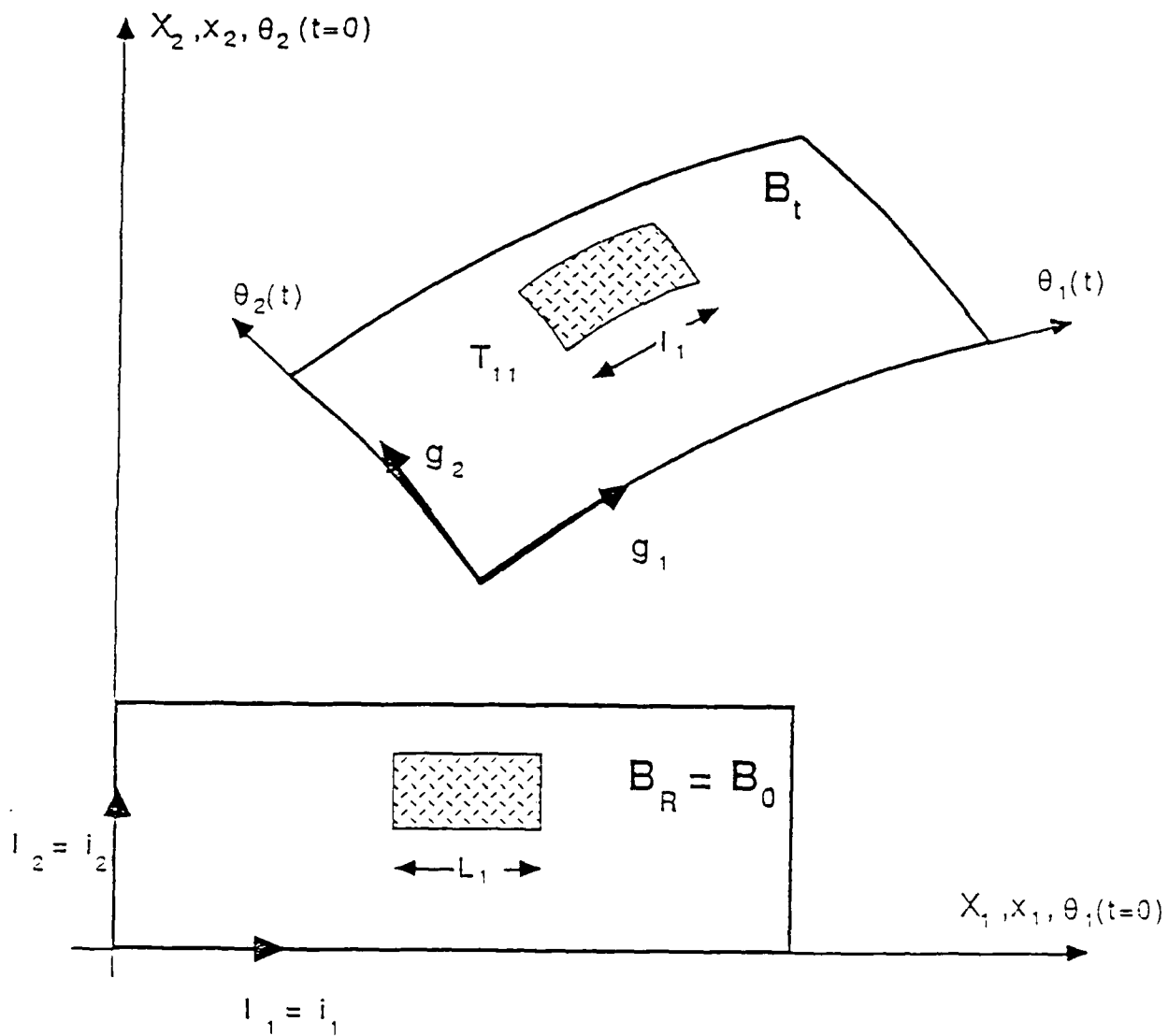
Figure 7: Large deformation of a deformable continuum.

70
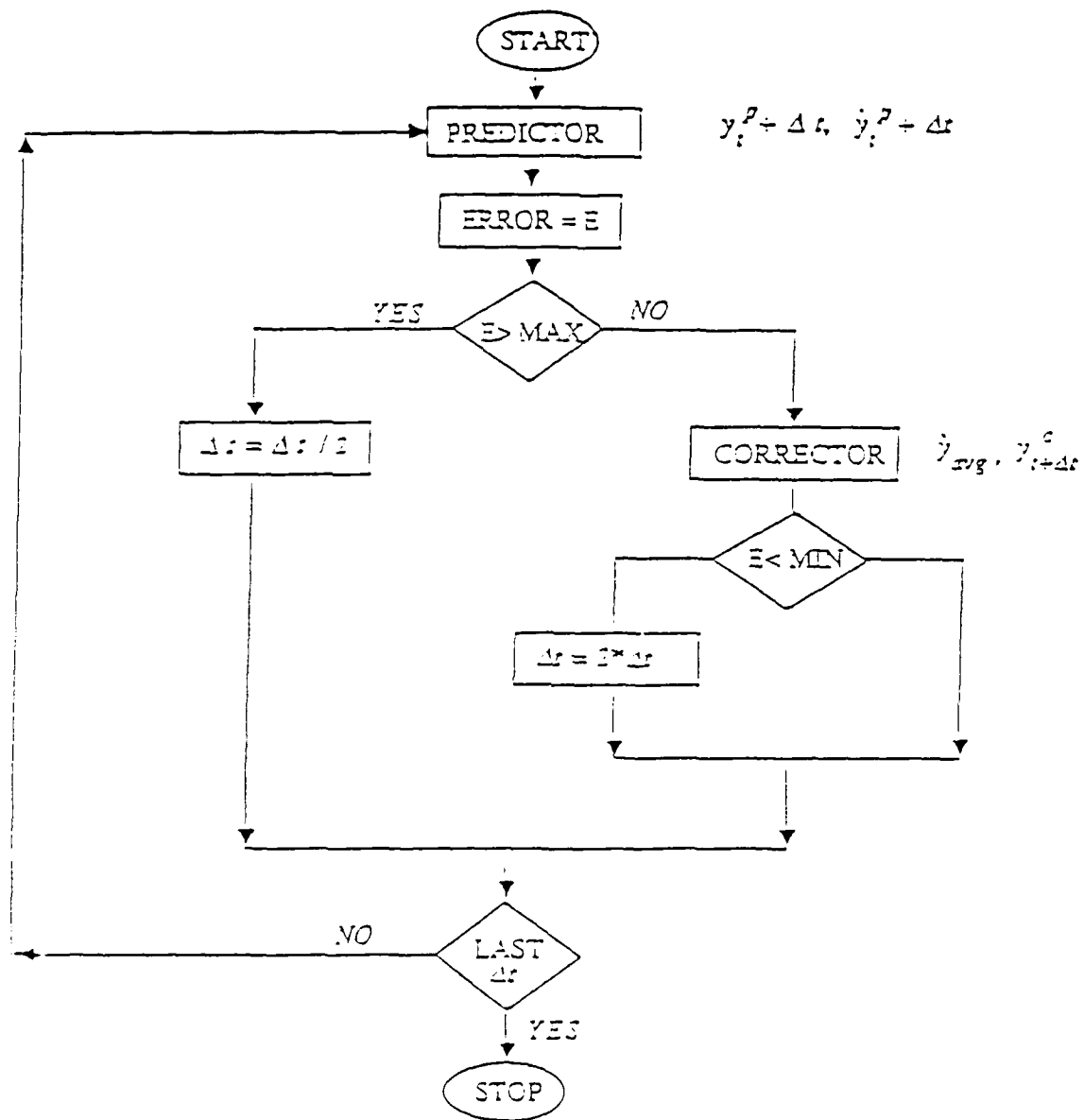
Figure 8: General scheme of predictor-corrector method with adaptive time step.
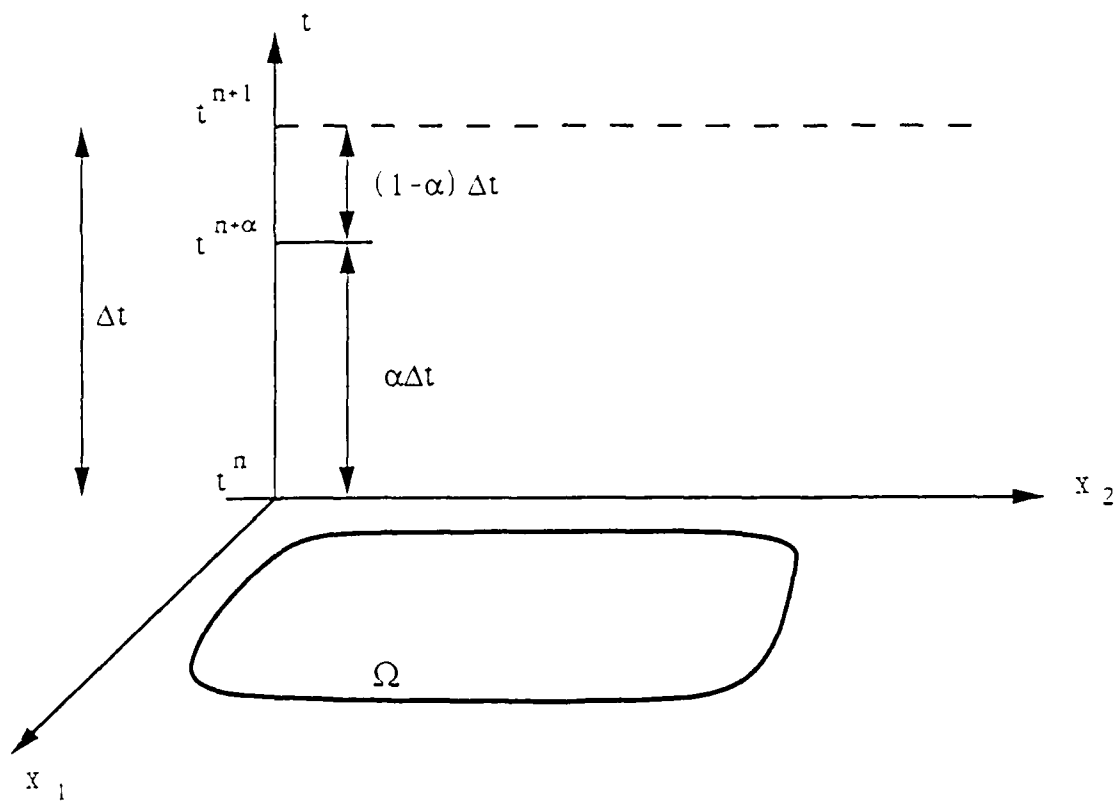
Figure 9: General Taylor series expansion in time.
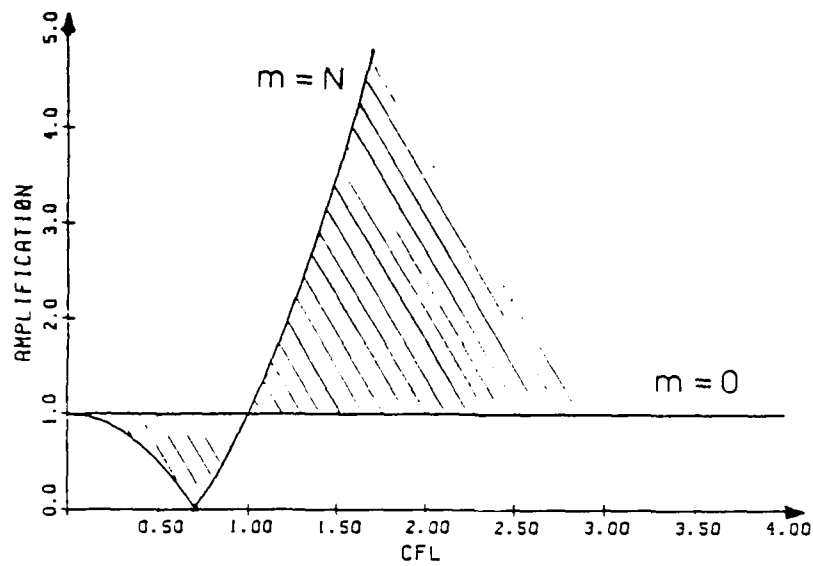
Figure 10: Stability analysis for fully explicit second-order scheme.
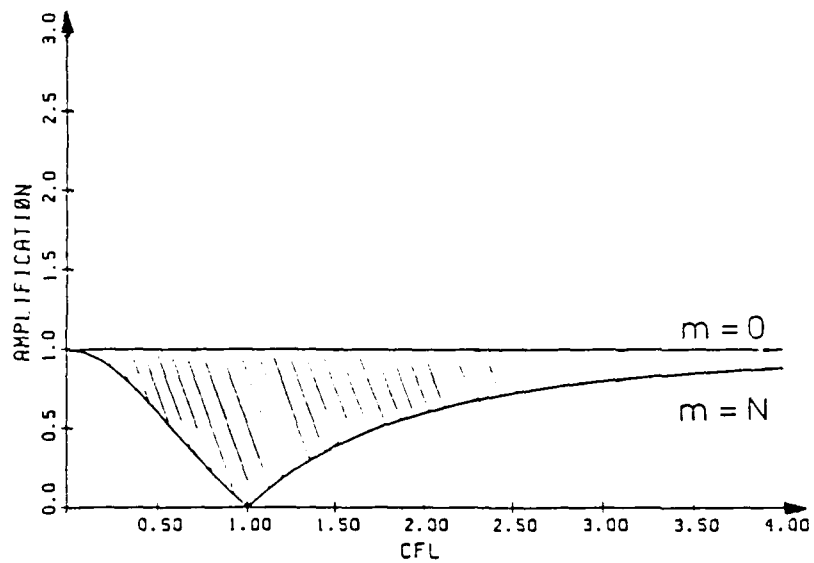
Figure 11: Stability analysis for weakly implicit scheme: $\alpha = 0$, $\beta = .5$, $\gamma = .5$.
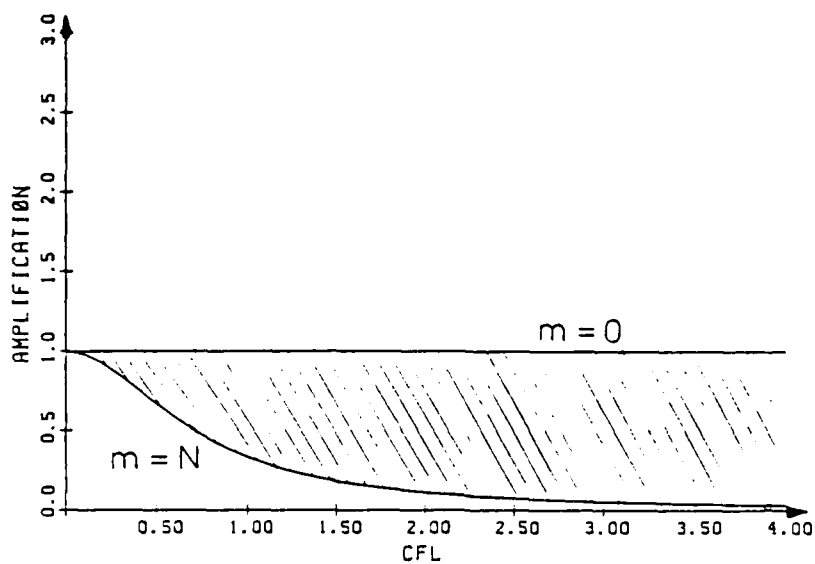
Figure 12: Stability analysis for weakly implicit scheme: $\alpha = 0$. $\beta = 1$. $\gamma = 1$.
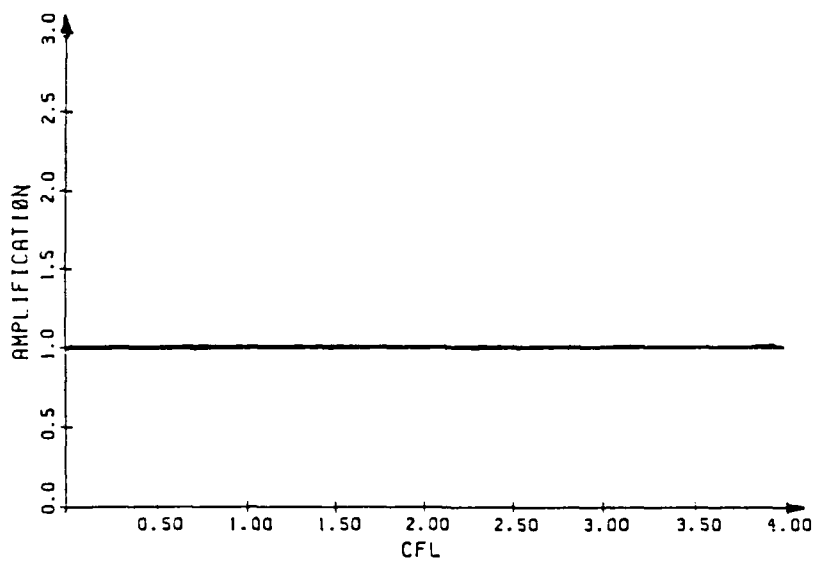
Figure 13: Stability analysis for Crank-Nicholson scheme: $\alpha = .5$. $\beta = .5$. $\gamma = .5$.

74
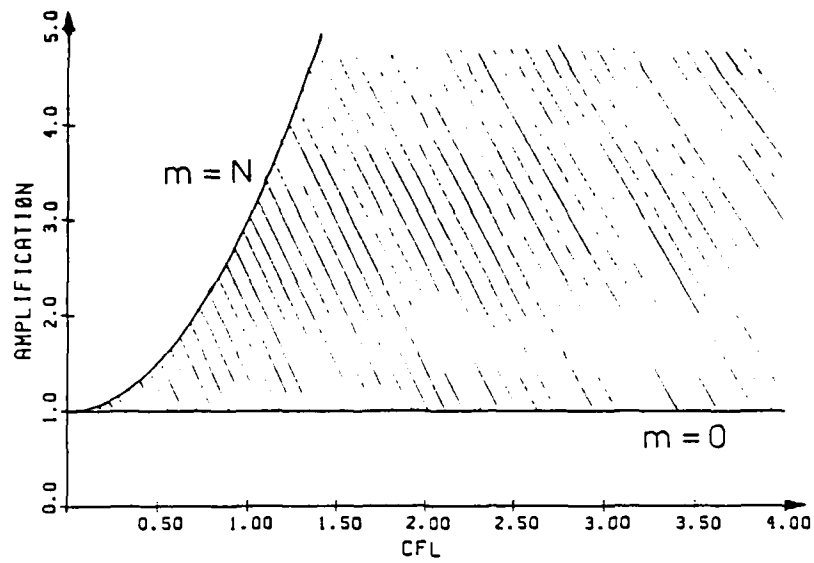
Figure 14: Stability analysis for implicit scheme: $\alpha = 1$, $\beta = 0$, $\gamma = 0$.
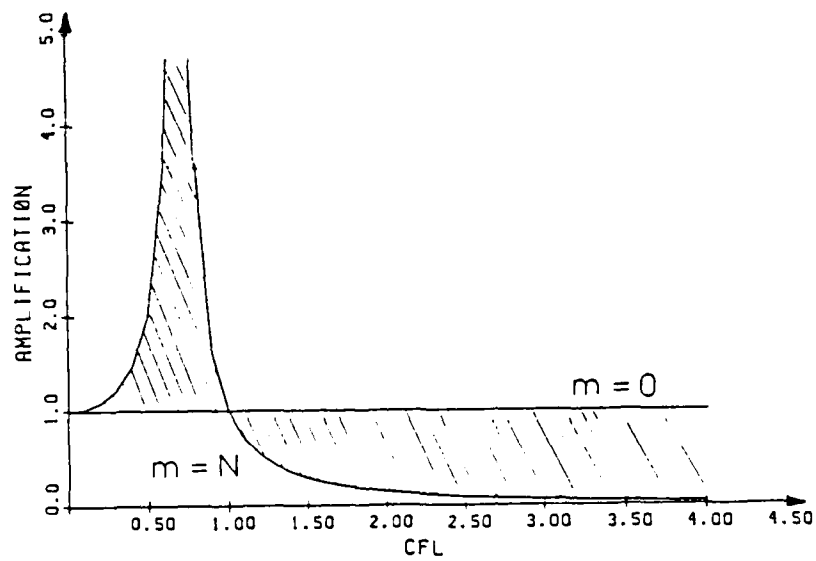
Figure 15: Stability analysis for fully implicit scheme: $\alpha = 1$, $\beta = 1$, $\gamma = 1$.
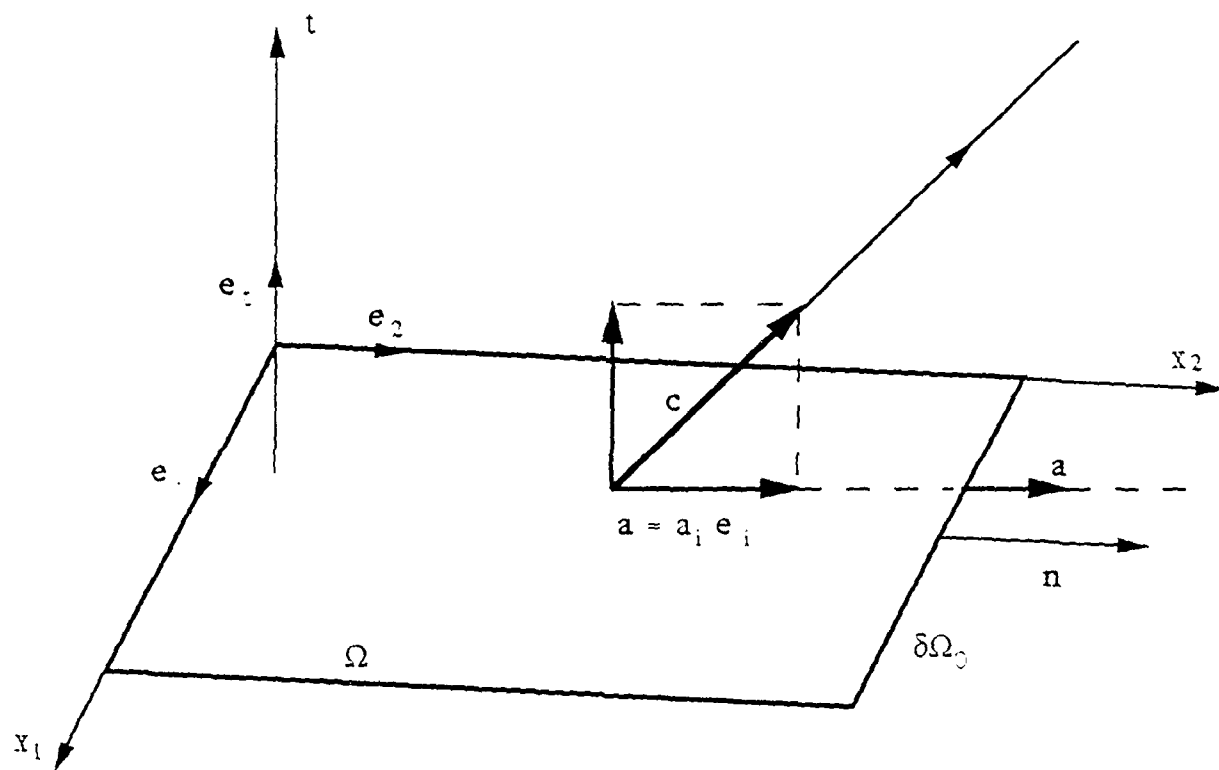
Figure 16: Interpretation of the outflow boundary condition.

76
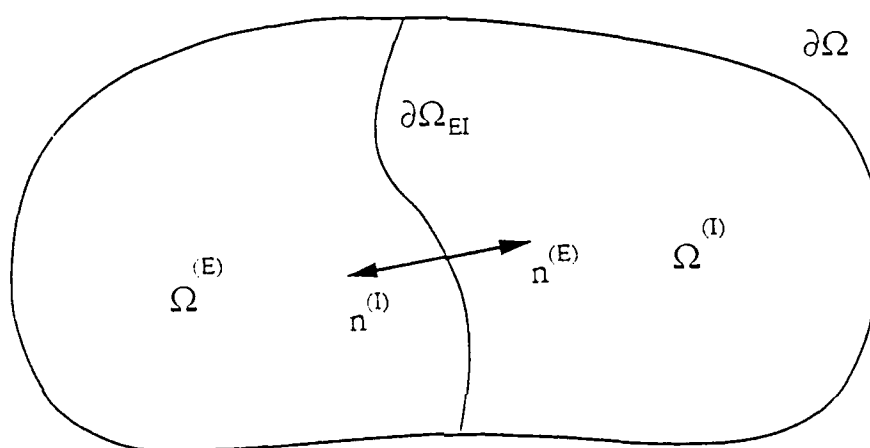
Figure 17: Implicit/explicit zones.
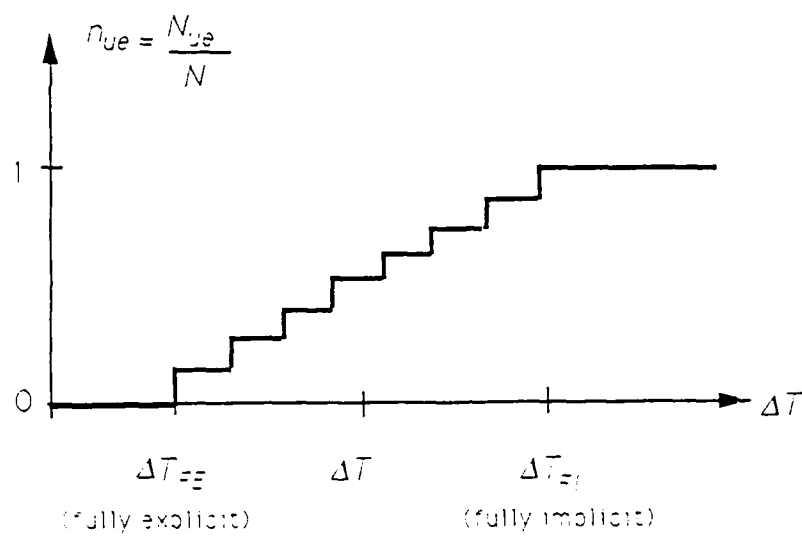
Figure 18: Relative number of implicit elements for increasing time step.
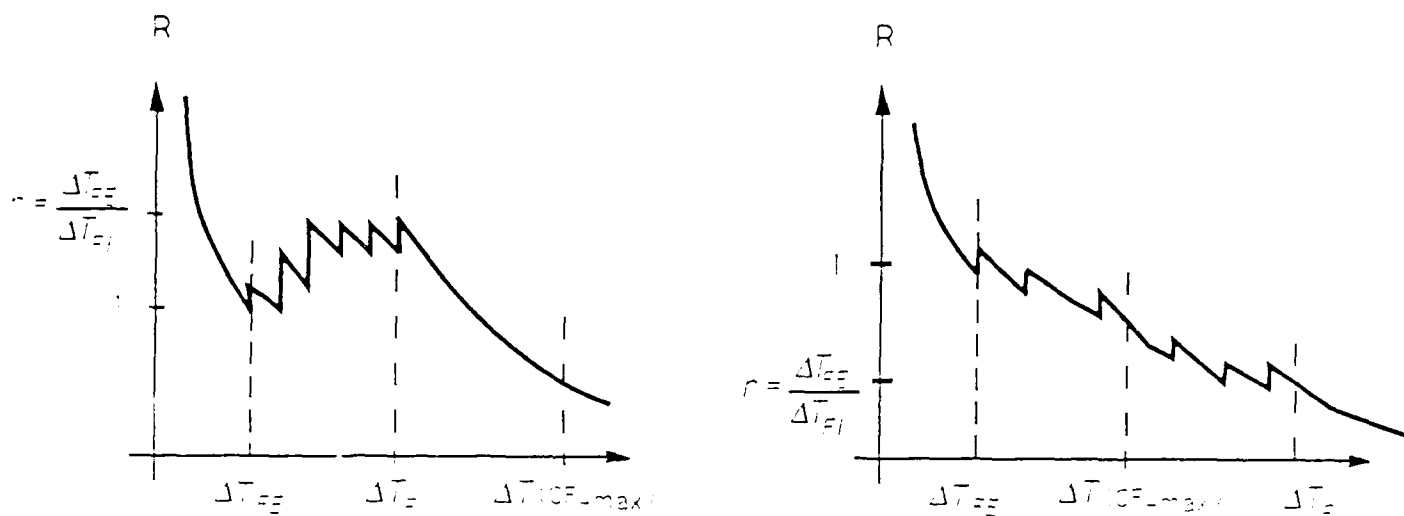
Figure 19: Reduction of the cost of computations due to implicit/explicit procedure.
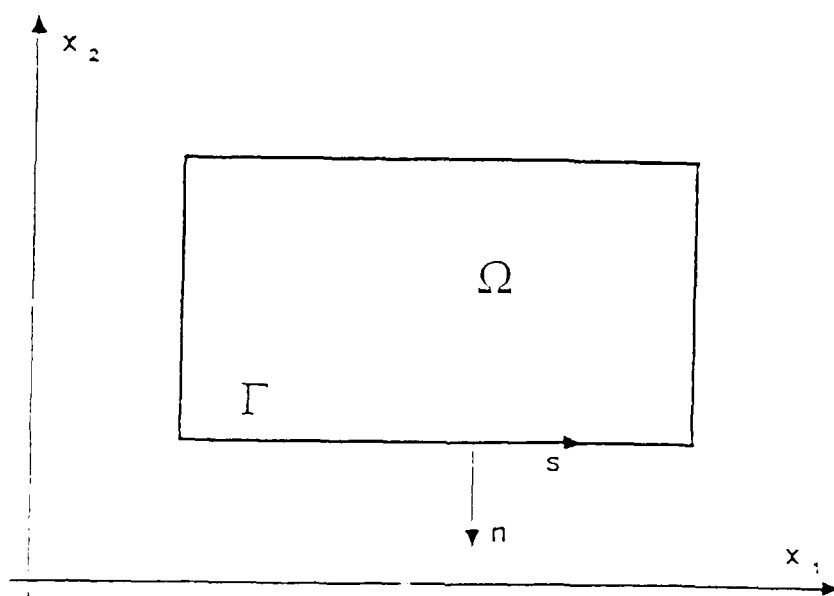
Figure 20: Domain for computation of boundary fluxes.

79
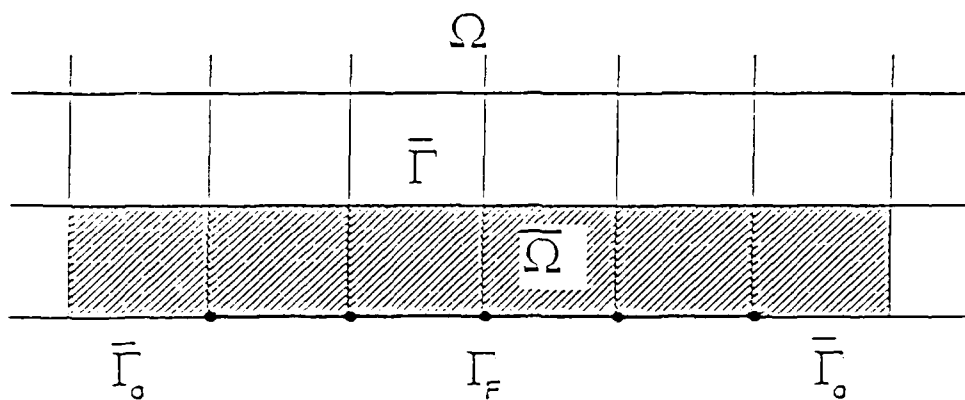
Figure 21: Subdomain for consistent computation of boundary fluxes.
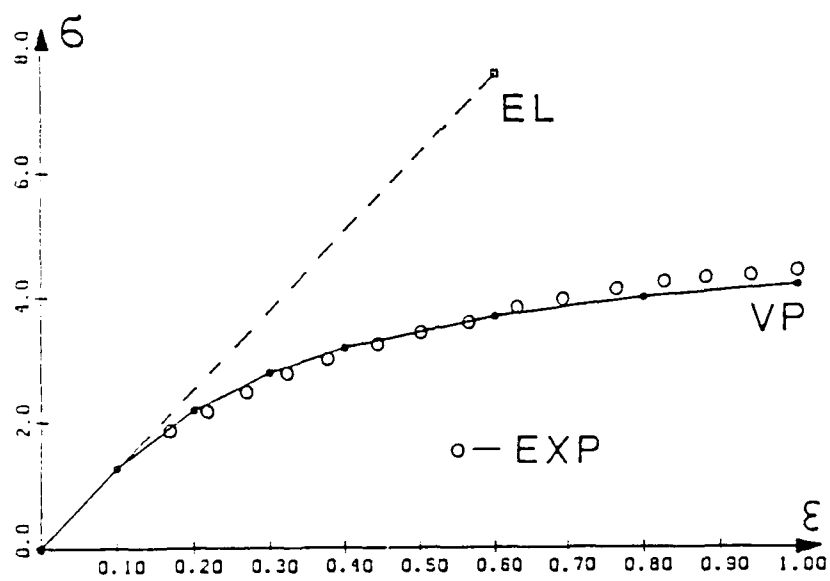
Figure 22: One-dimensional tension test.
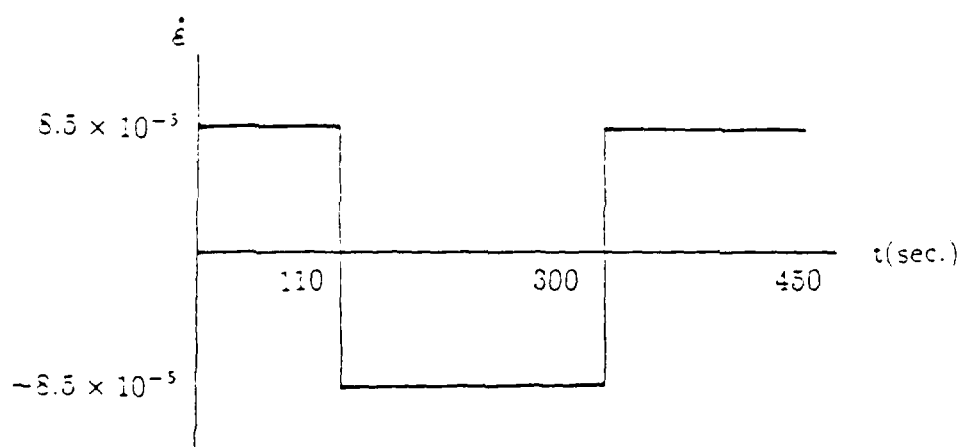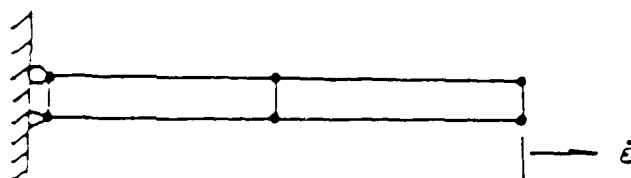
Figure 23: Bar subjected to specified strain history—problem statement.
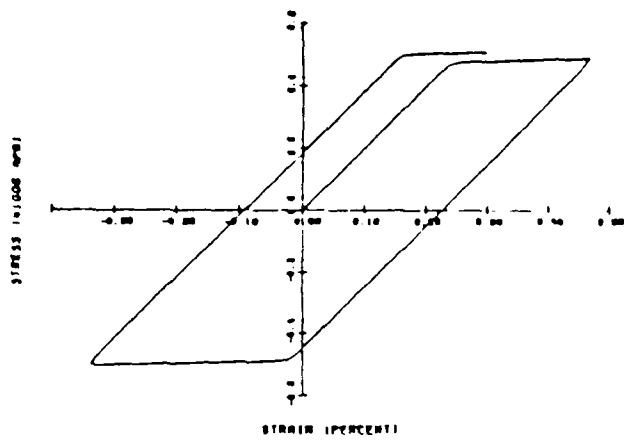
a) Stress-strain, T = 530 R
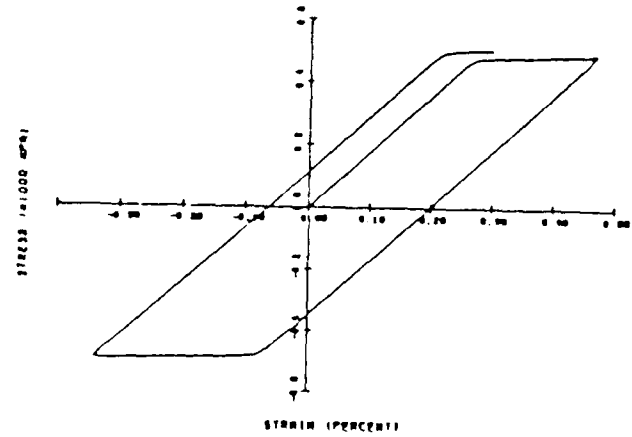
b) Stress-strain, T = 1500 R
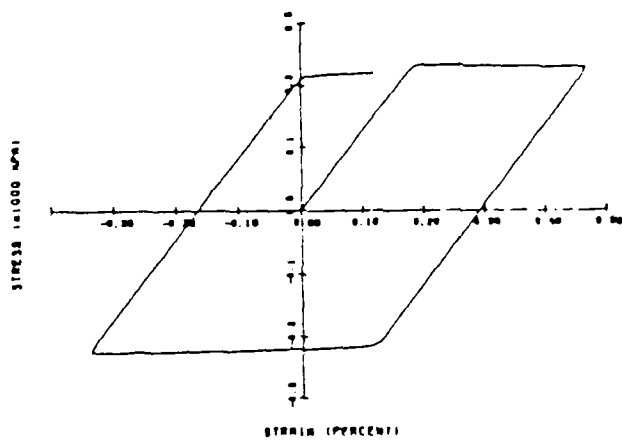
c) Stress-strain, T = 2250 R
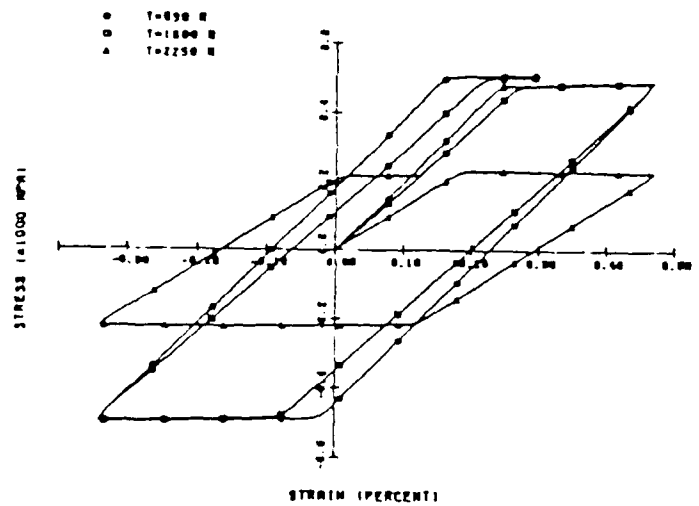
d) Comparative Stress-strain Curves

Figure 24: Bar subjected to specified strain history.

(a) Mechanical model.

$q_n = 0$
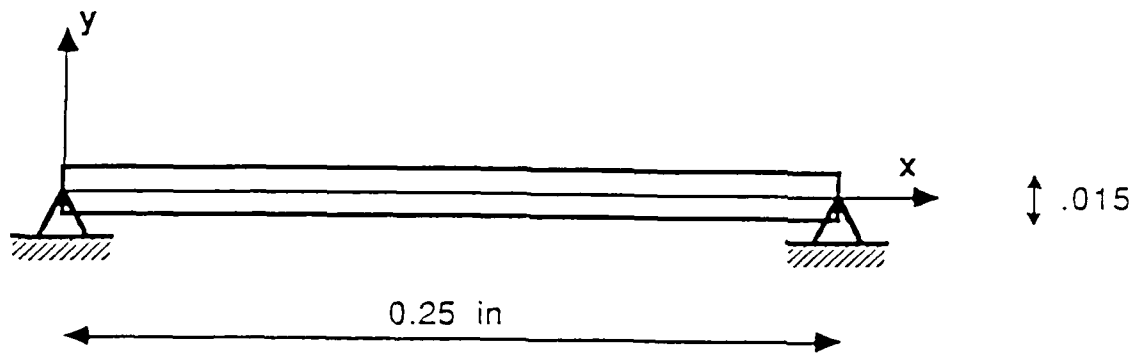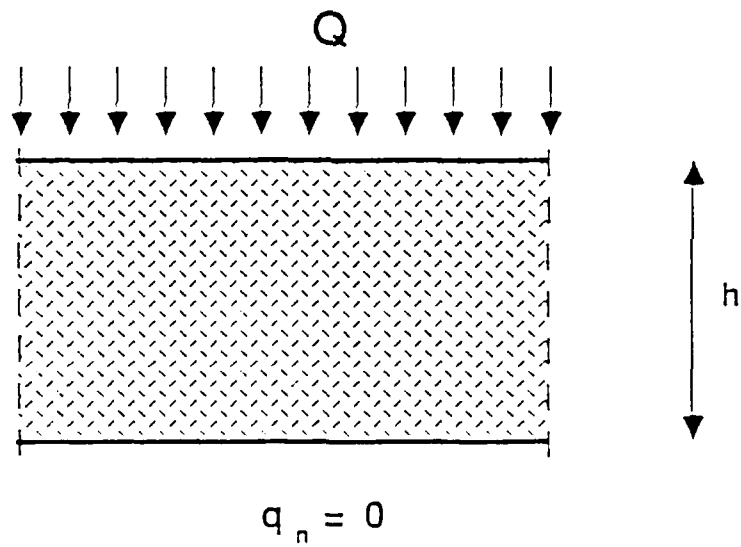
(b) 1-D thermal model.

Figure 25: Beam-column—problem statement.
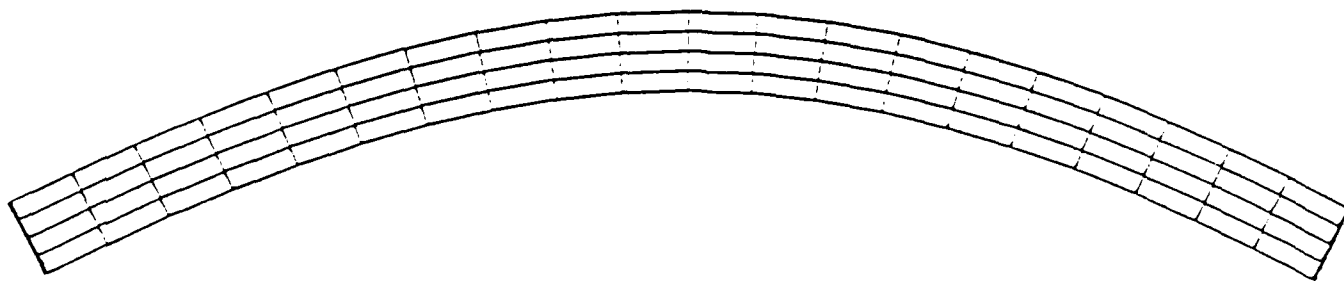
(a) 20 × 4 elements.
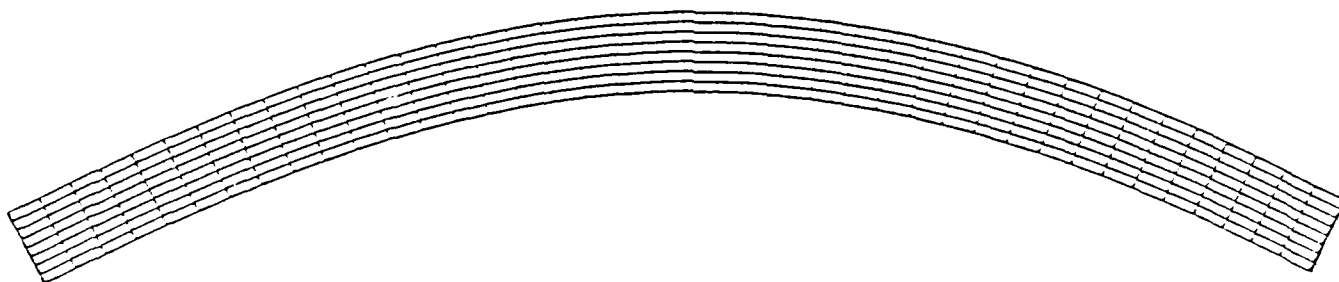
(b) 40 × 3 elements.
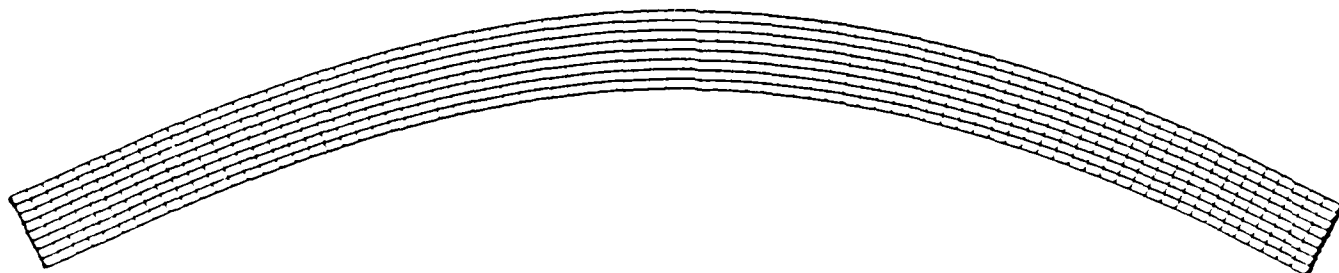
(c) 80 × 3 elements.

Figure 26: Restrained panel. Deformed configurations at $t = .1$ sec for various finite element models.
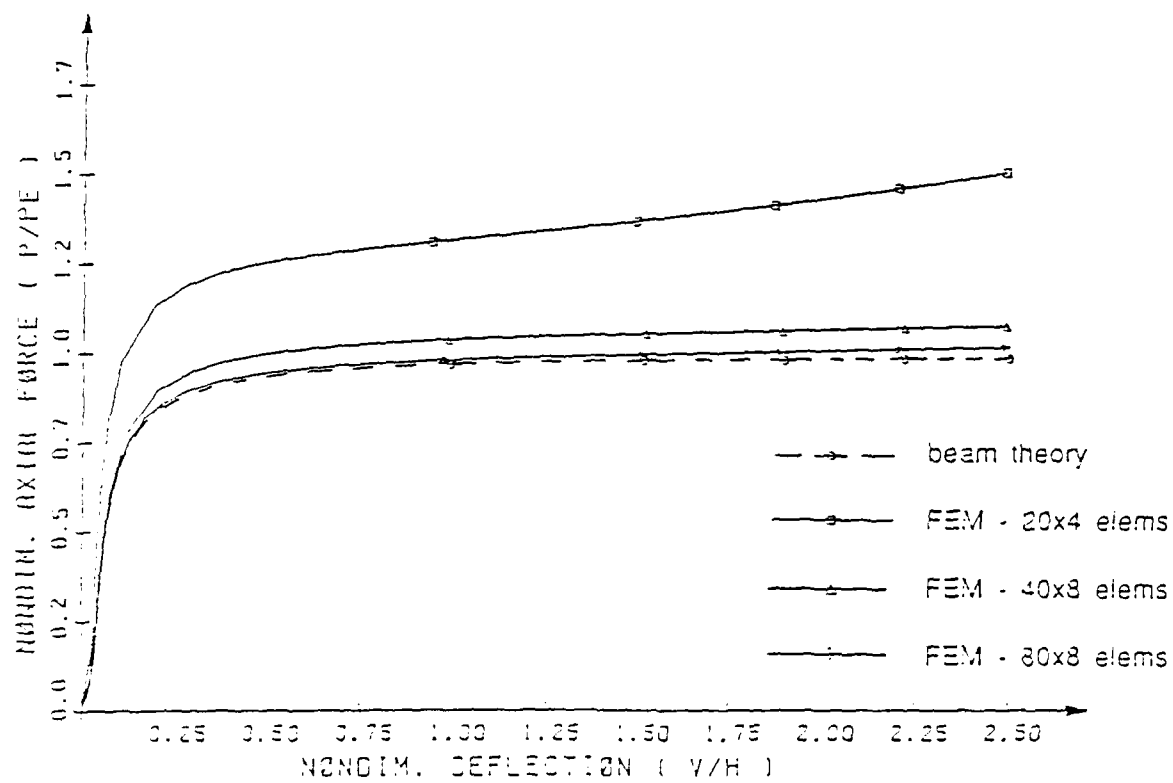
Figure 27: Restrained panel. Comparison of beam theory solution with finite element solutions on different meshes.
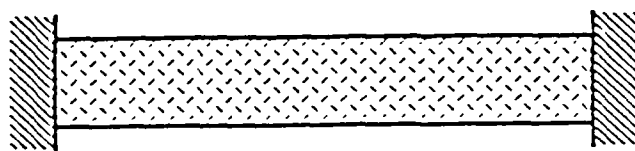
T = 760 $^{\circ}$C

871 $^{\circ}$C

1090 $^{\circ}$C

(a) Mechanical model.
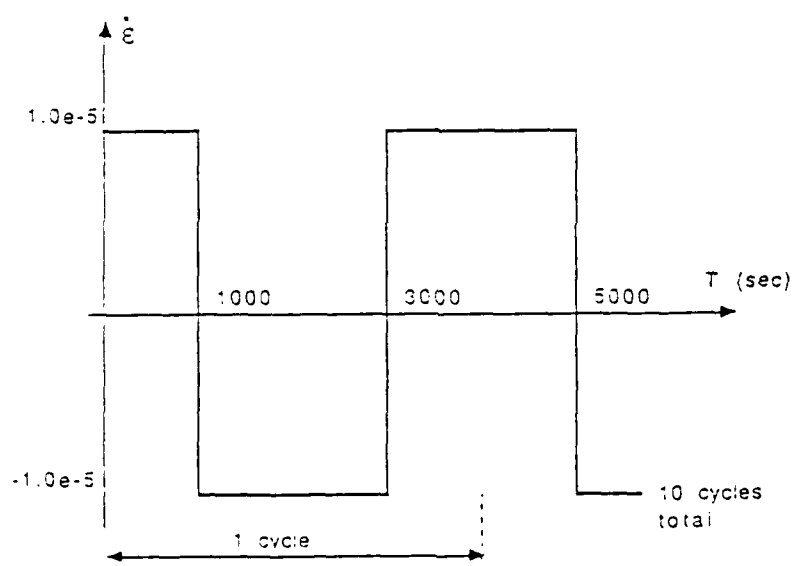
(b) Prescribed strain rate history.

Figure 28: Problem statement for a test of damage.
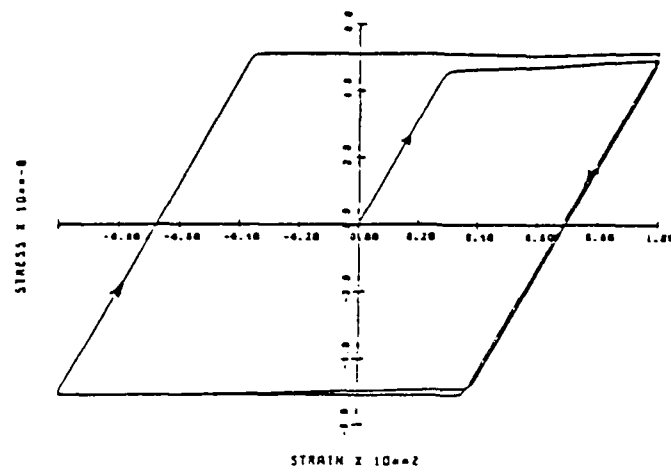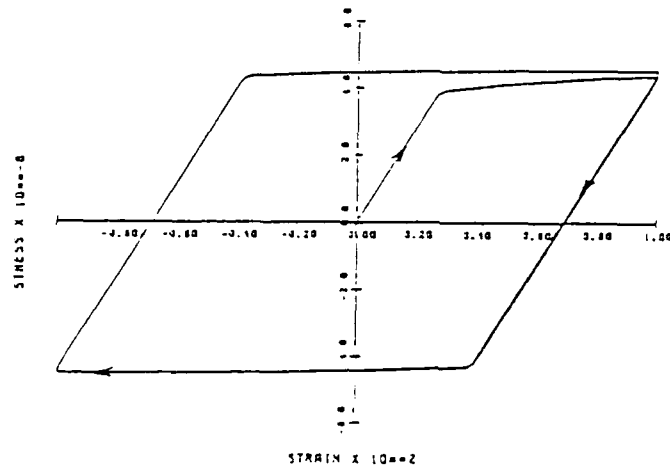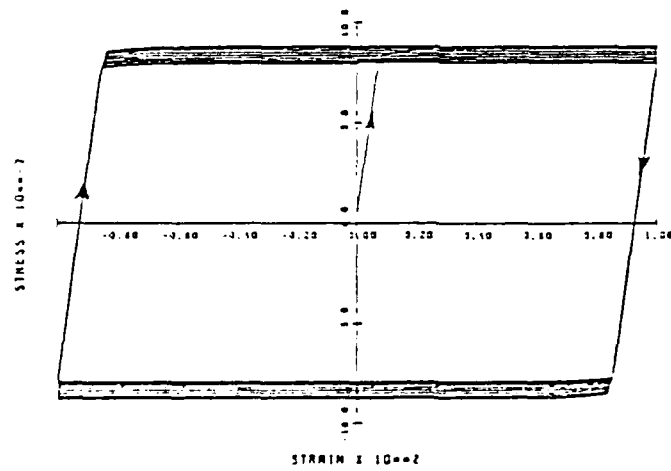
Figure 29: Stress–strain curves with damage evolution at different temperatures.
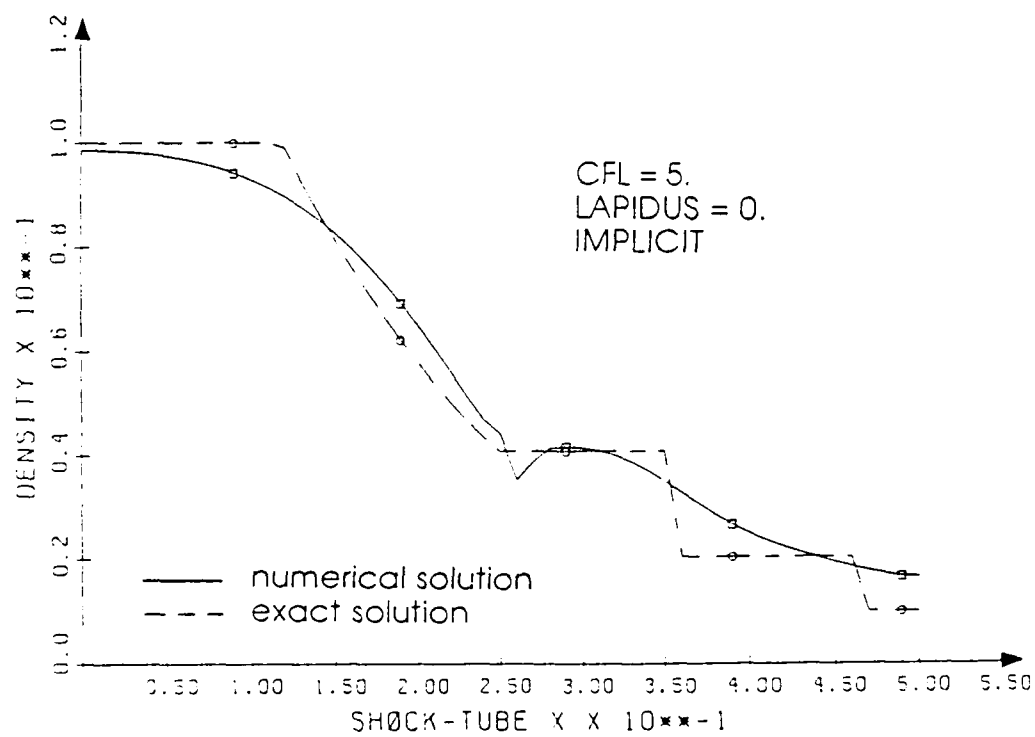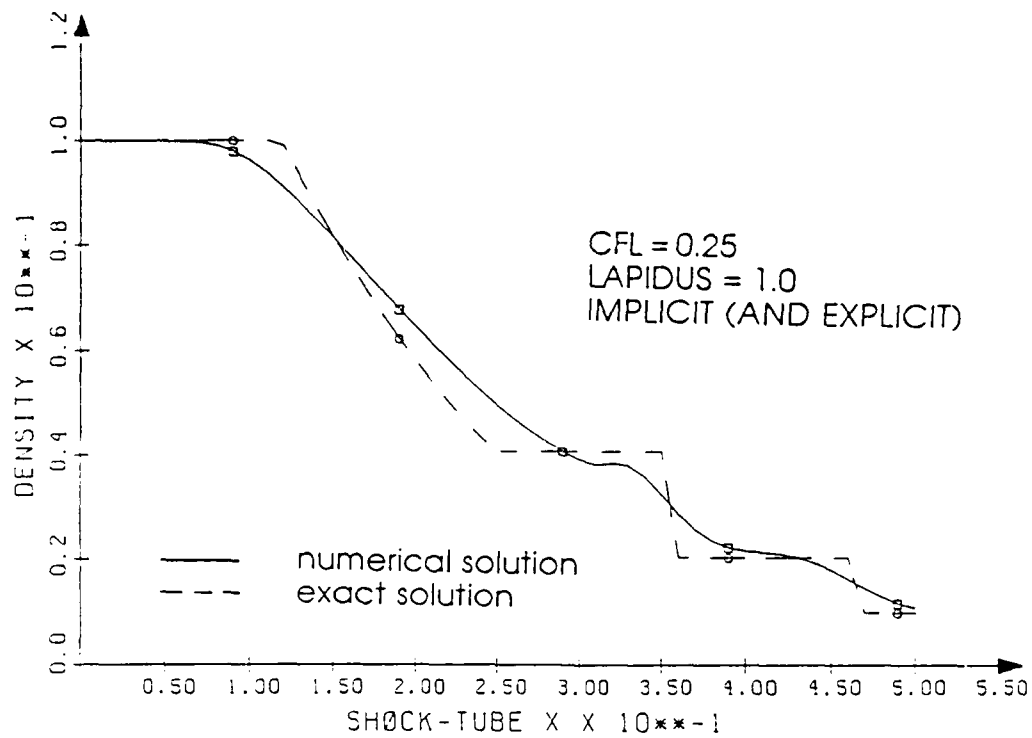
Figure 30: Results for a shock tube problem.
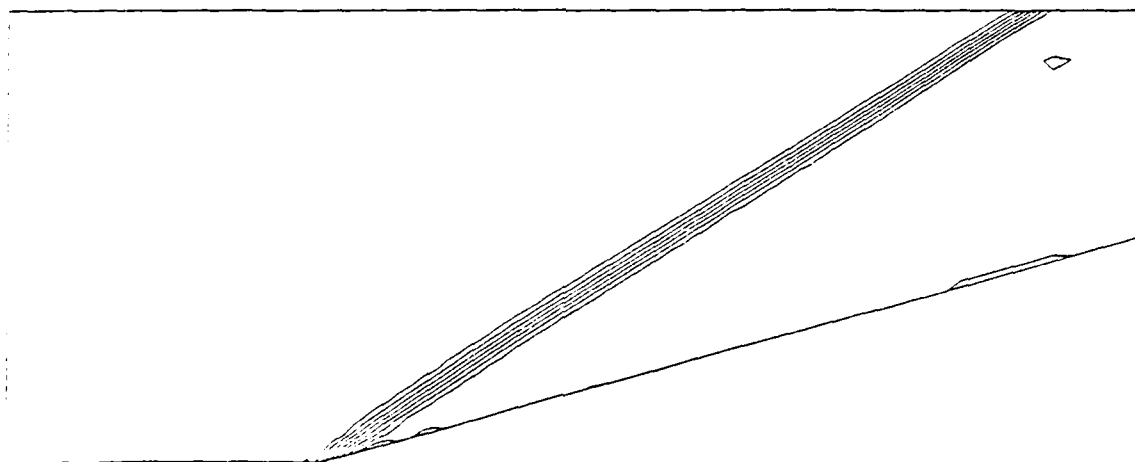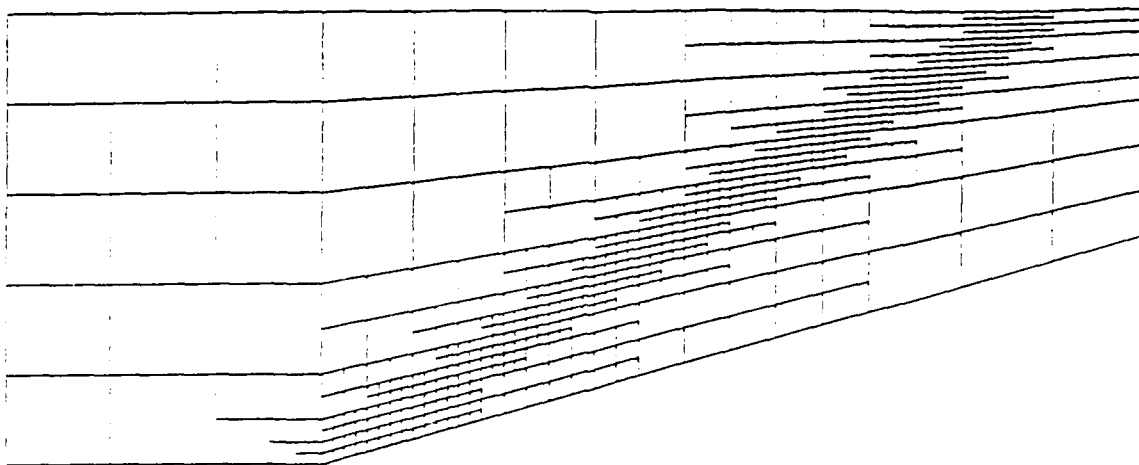
DENSITY CONTOURS   MIN = 0.950E-00   MAX = 0.230E+01   INTERVAL= 0.150E-00

Figure 31: Flow over a 16° compression corner (Mach 3).
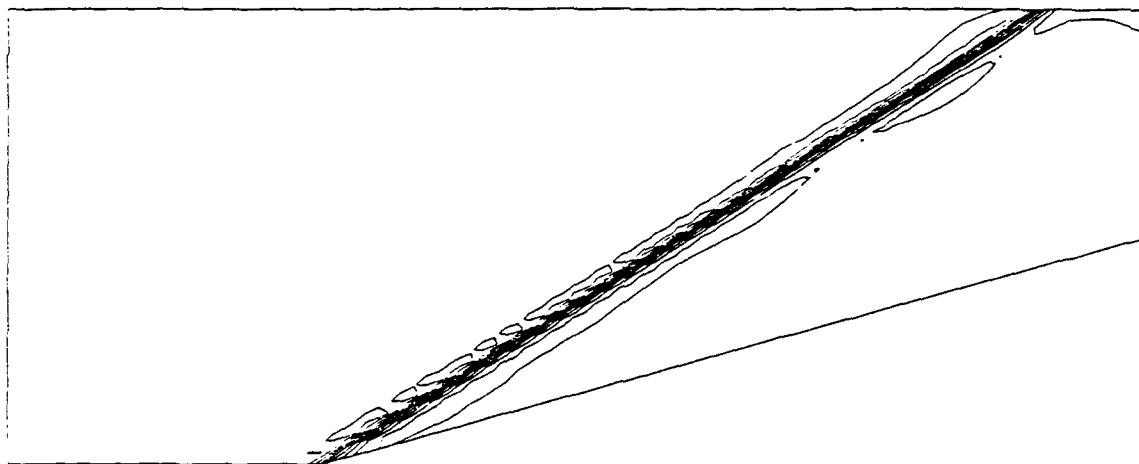
DENSITY CONTOURS MIN = 0.950E+00 MAX = 0.230E+01 INTERVAL= 0.150E+00

Figure 32: Solution of a compression corner with no artificial dissipation and large time step (CFL = 10).
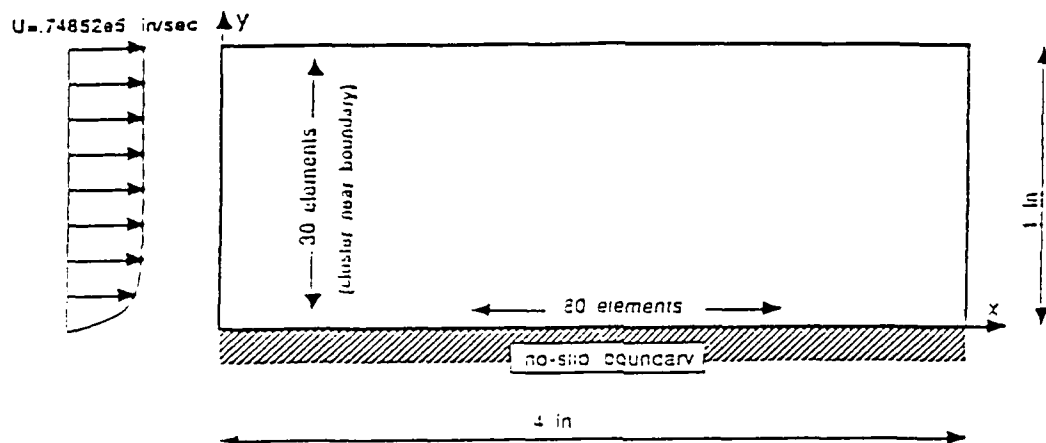
Figure 33: Problem statement for a supersonic boundary layer problem.
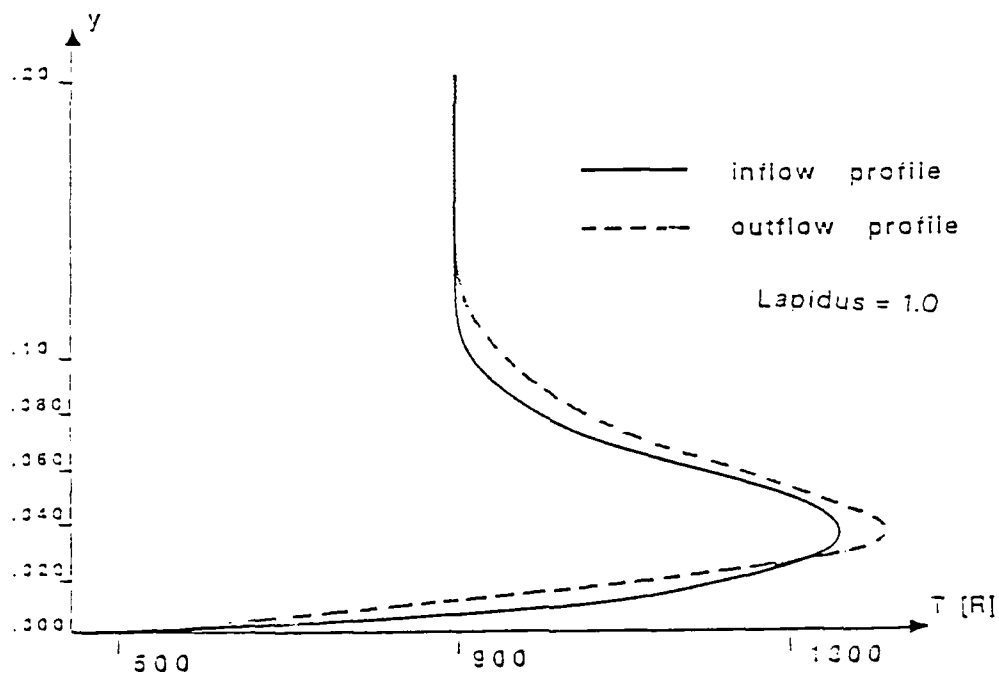
Figure 34: Temperature profiles for a supersonic boundary layer problem.

91
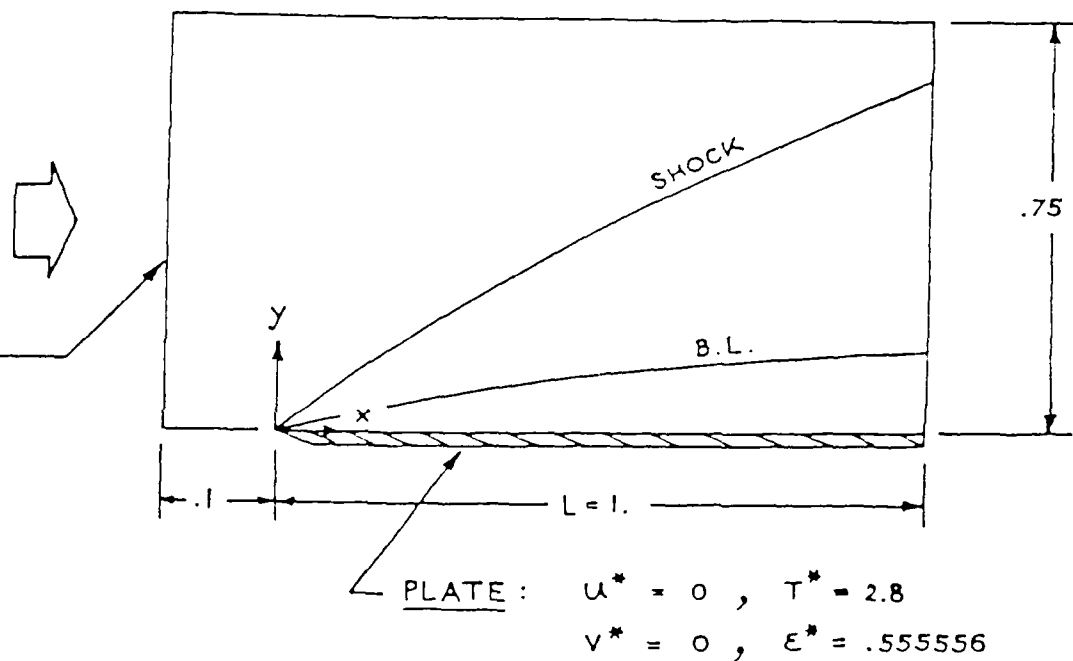
Figure 35: Problem statement for a flat plate problem.
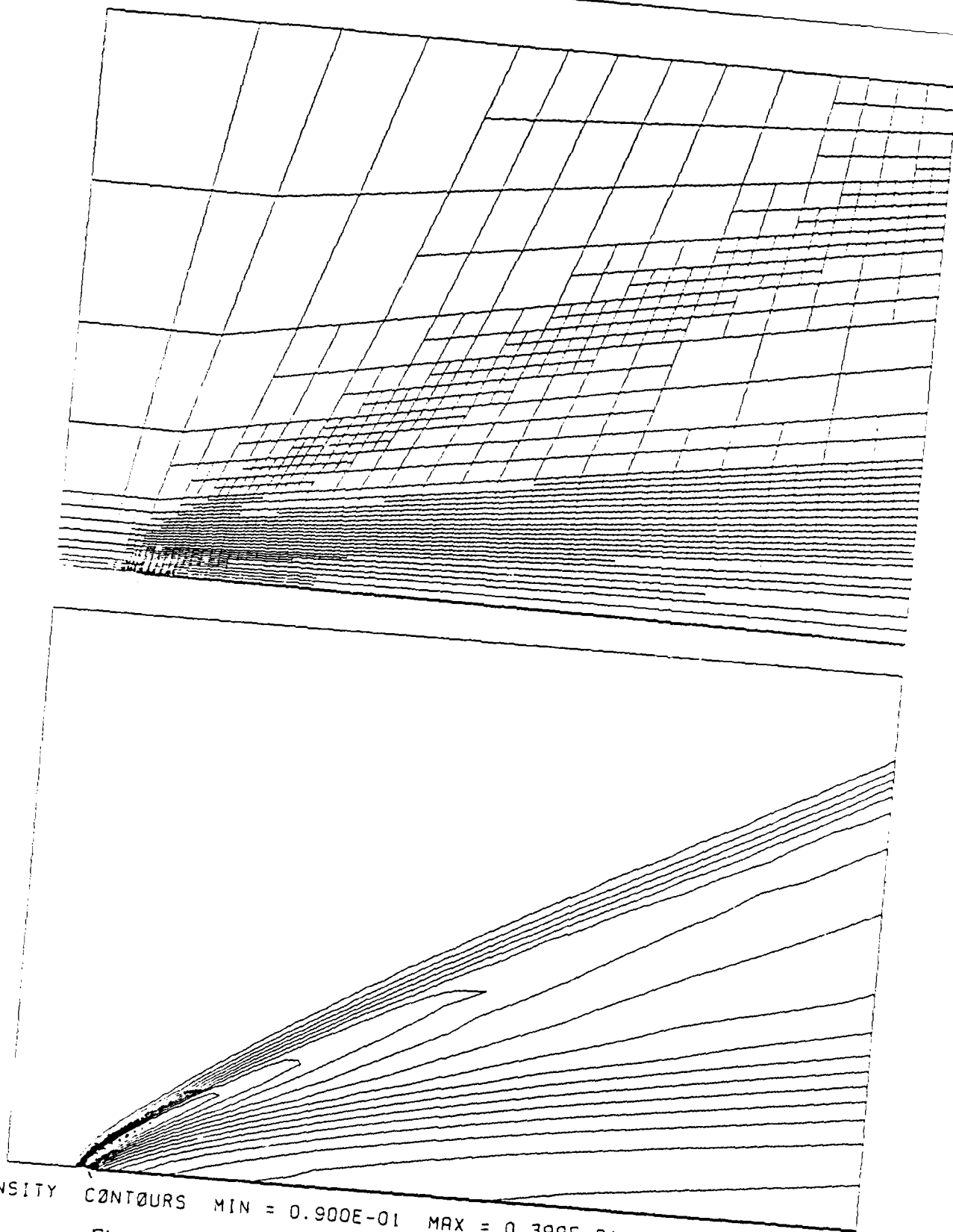
DENSITY CØNTØURS   MIN = 0.900E-01   MAX = 0.399E+01   INTERVAL= 0.100E+00

Figure 36: Mesh and density contours for a flat plate problem.
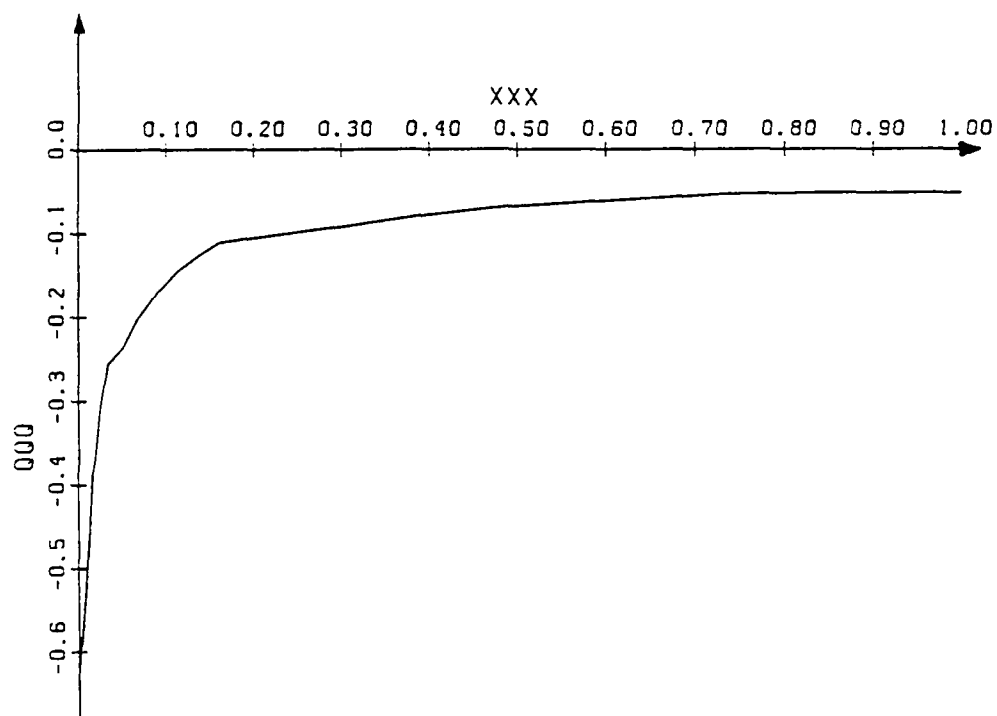
Figure 37: Heating rates for a flat plate problem.
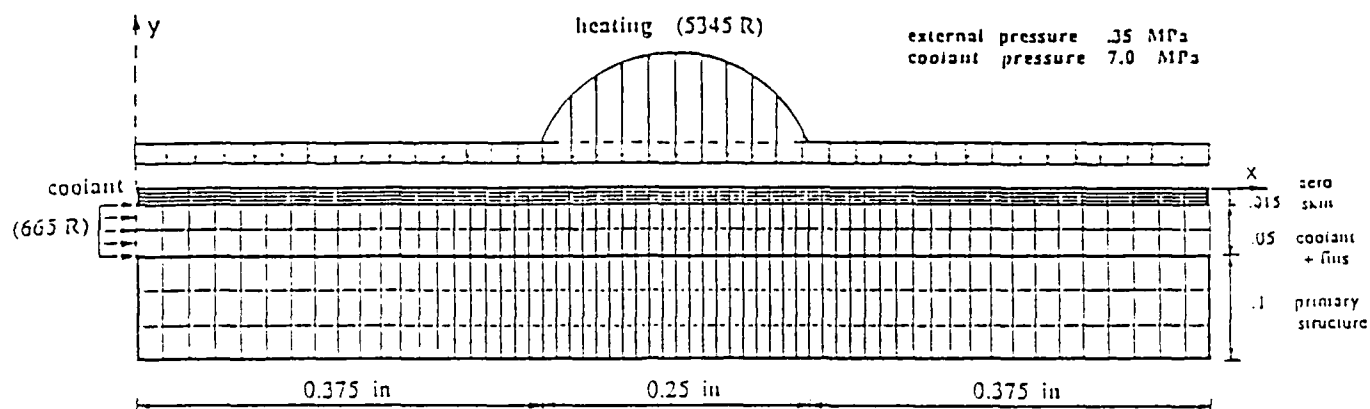
(a) thermal–structural model
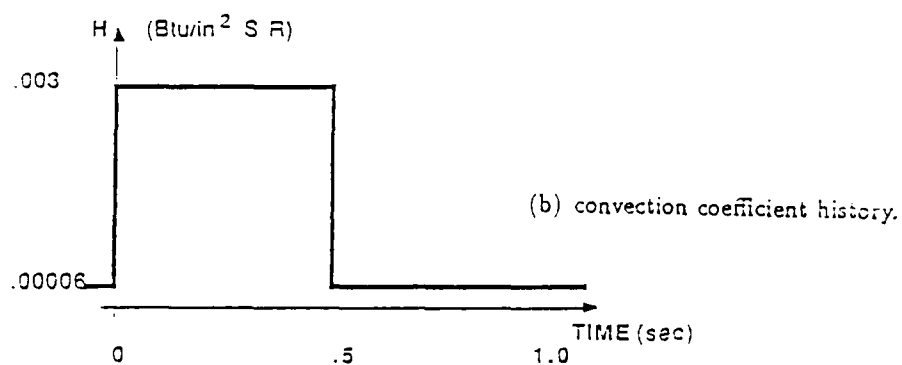
(b) convection coefficient history.

Figure 38: Problem statement for a convectively cooled structure.

95

$T_{max} = 2254\ R$

665 R

736 R
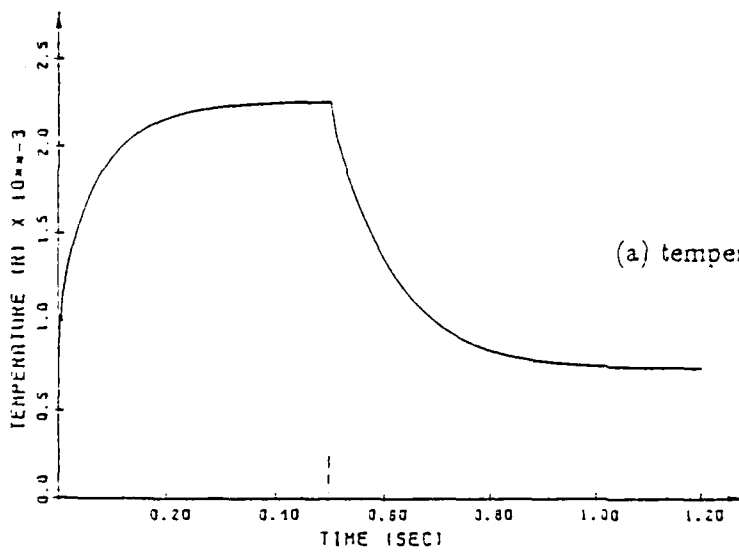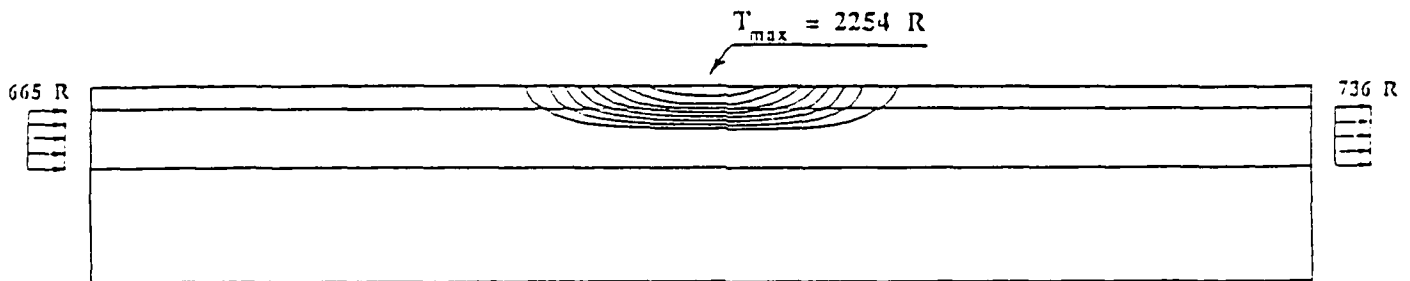
(b) temperature contours at $t = 0.5s$.

(a) temperature history at $x = 0.5\ in,\ y = 0$

TEMPERATURE (R) X 10**-3

2.5

2.0

1.5

1.0

0.5

0.0

0.20   0.40   0.60   0.80   1.00   1.20

TIME (SEC)

Figure 39: Thermal response of a convectively cooled structure.
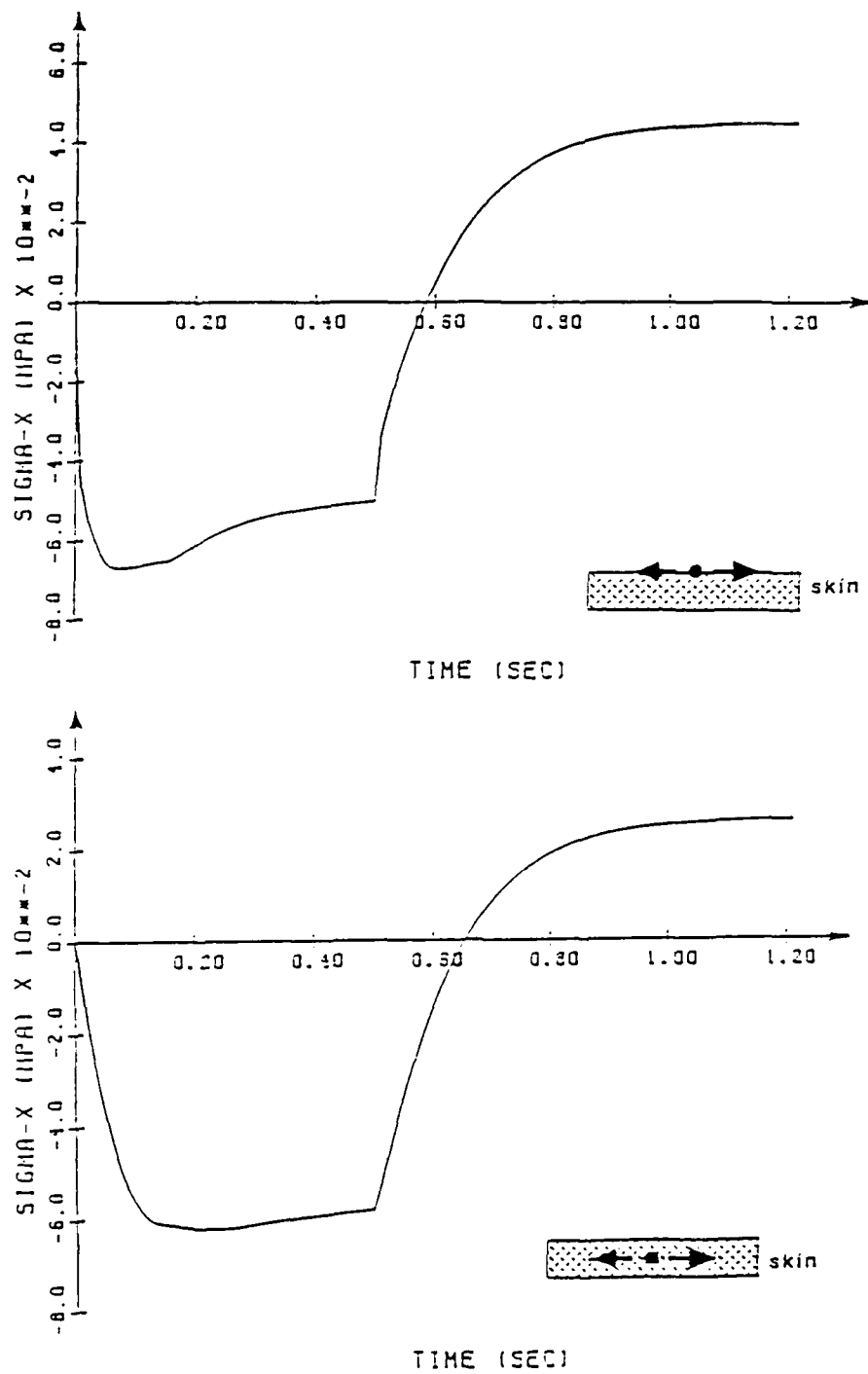
Figure 40: Viscoplastic stress histories in the aerodynamic skin.
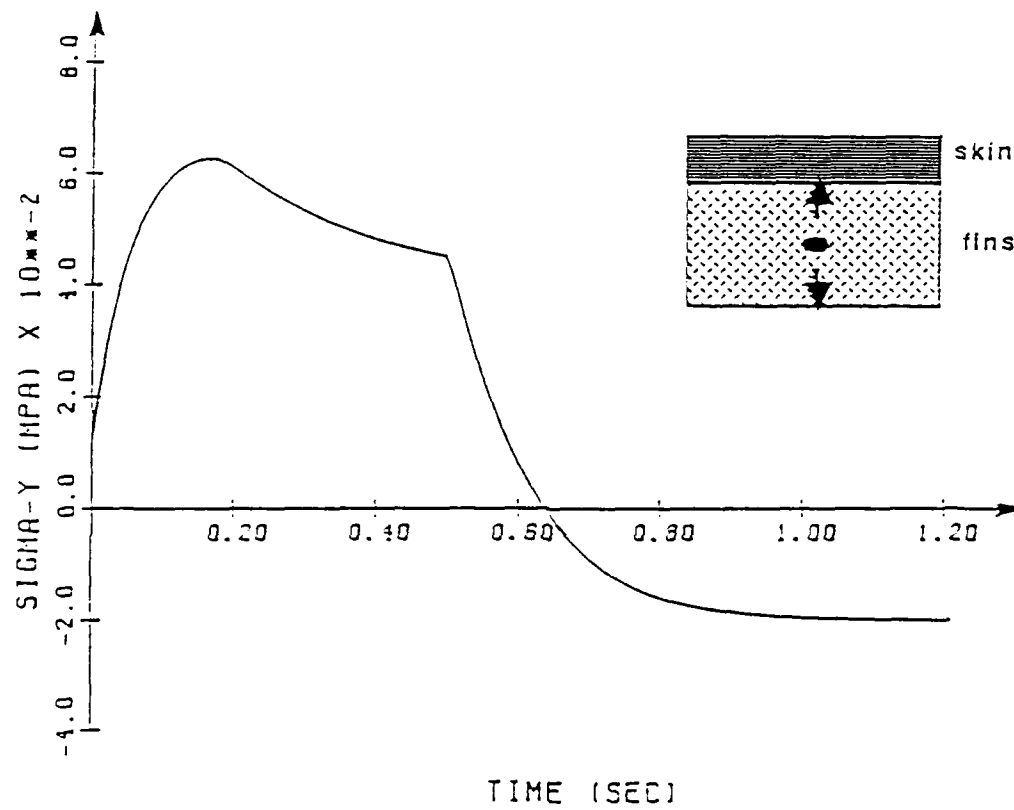
Figure 41: Viscoplastic stress histories in the heat exchanger fins.

98
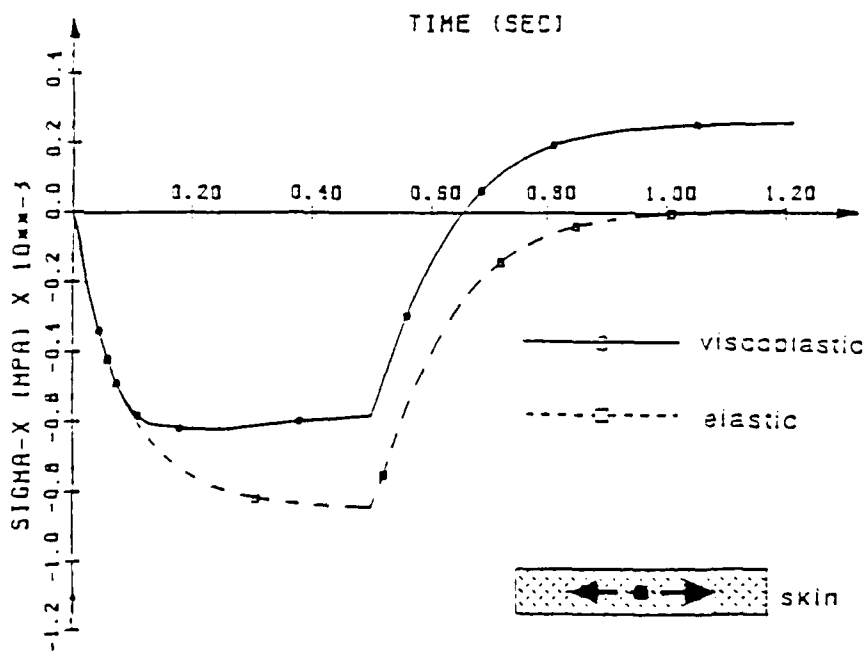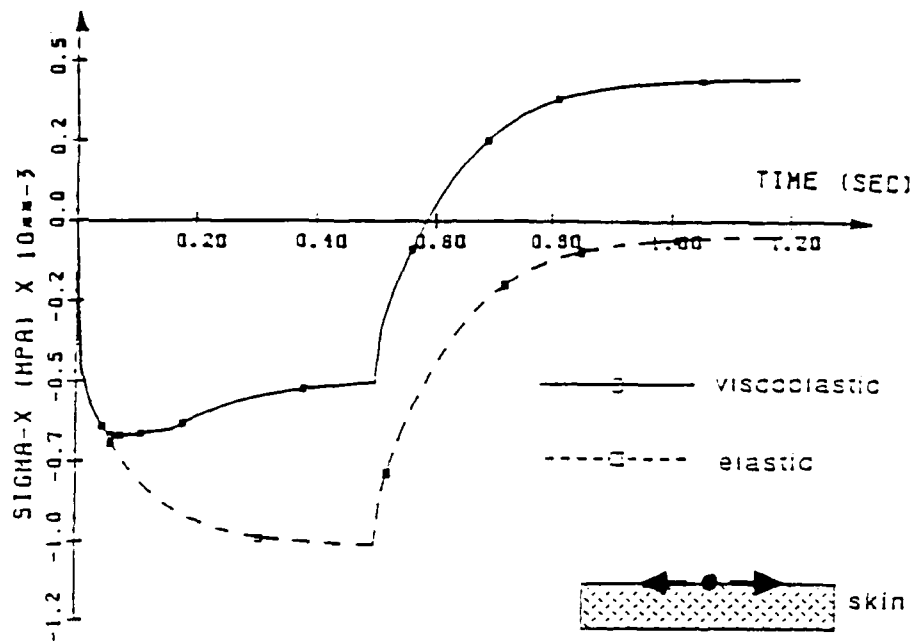
Figure 42: Comparison of viscoplastic and elastic stress histories in aerodynamic skin.

99
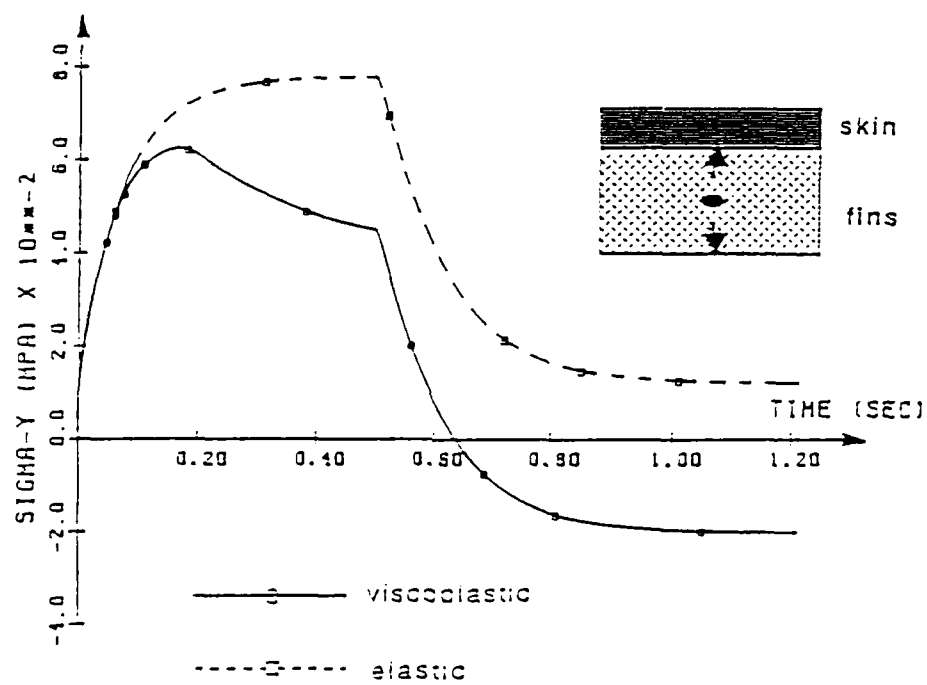
Figure 43: Comparison of viscoplastic and elastic stress histories in heat exchanger fins.
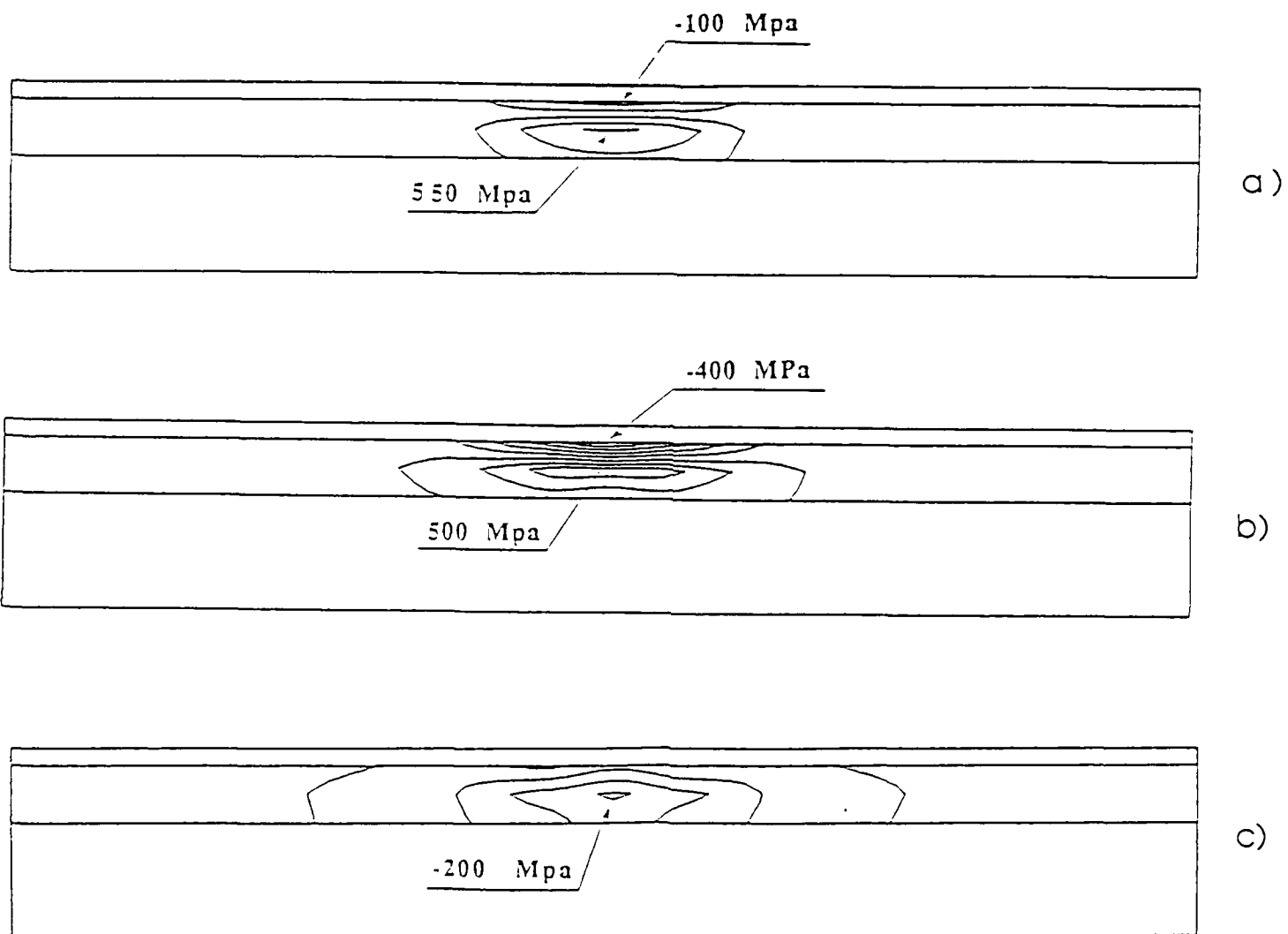
100

STRESS σ_x (MPa)
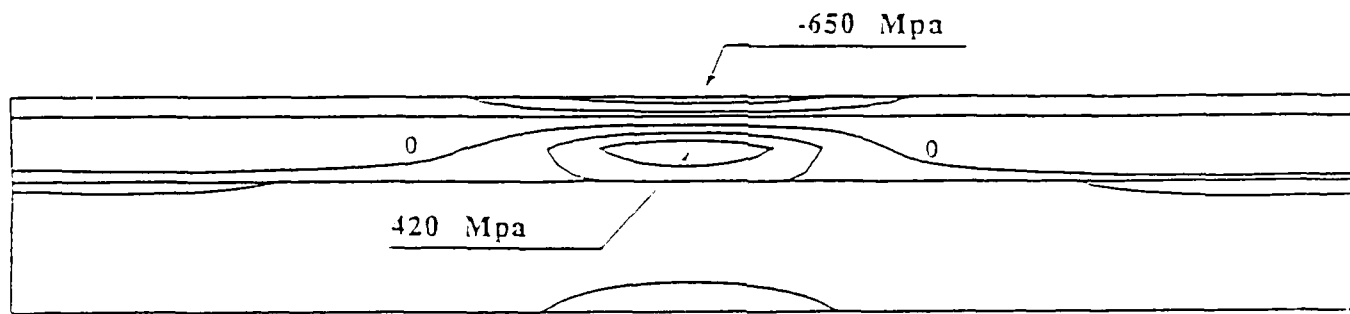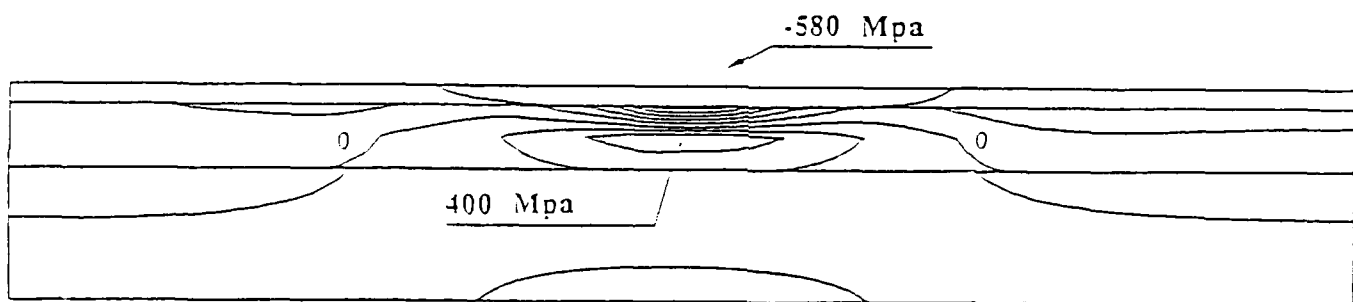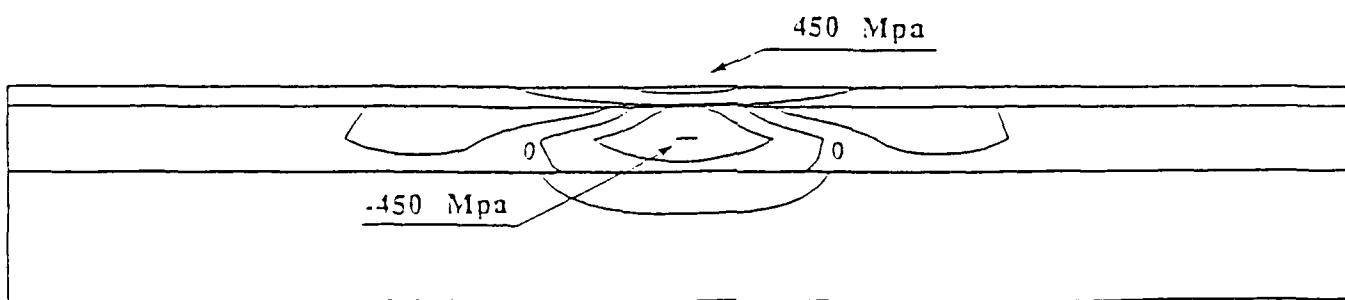
Figure 44: Contours of σ_x stress (a) $t = 0.05s$, (b) $t = 0.5s$, (c) $t = 1.2s$.

STRESS σ_y (MPa)

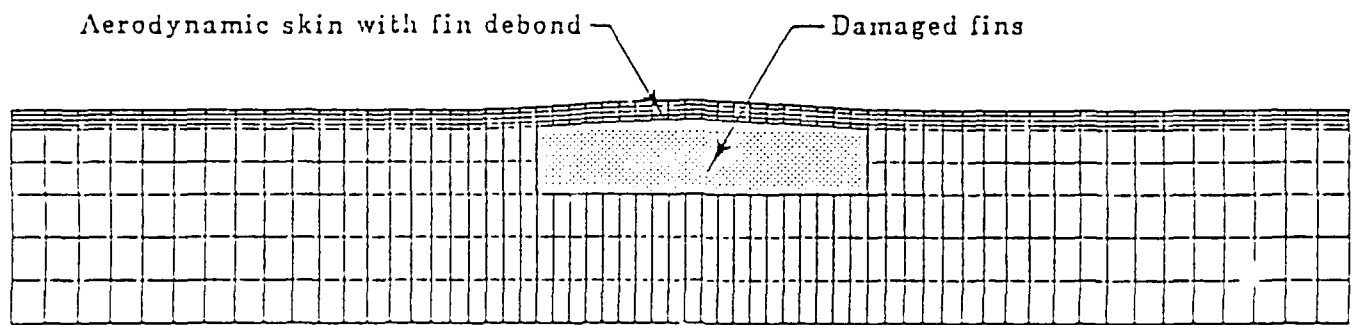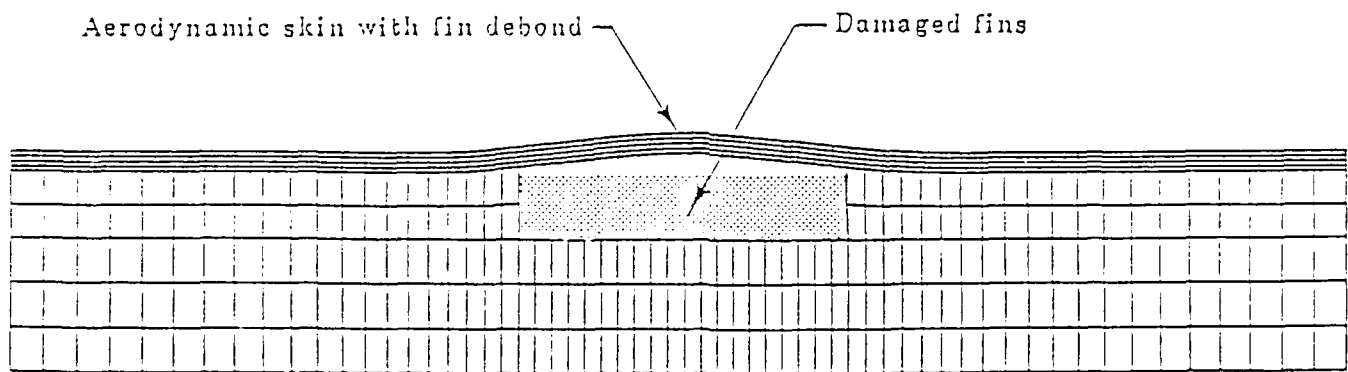Figure 45: Contours of σ_y stress (a) $t = 0.05s$. (b) $t = 0.5s$. (c) $t = 1.2s$.
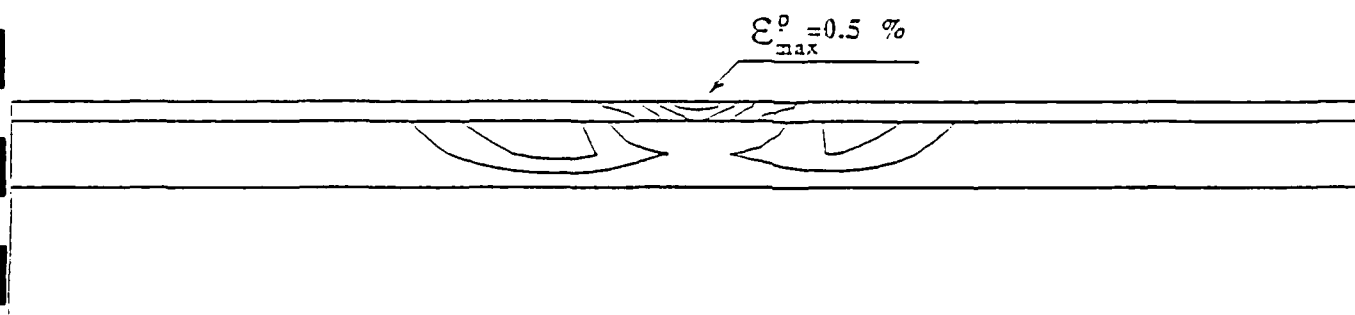
Figure 46: Principal plastic strain at $t = 0.5s$.

(a) Solution obtained with infinitesimal theory.

(b) Solution obtained with large displacement theory.

Figure 47: Maximum deformation of structure ($t = 0.5s$) with damaged heat exchanger fins. Deformation is shown to scale.
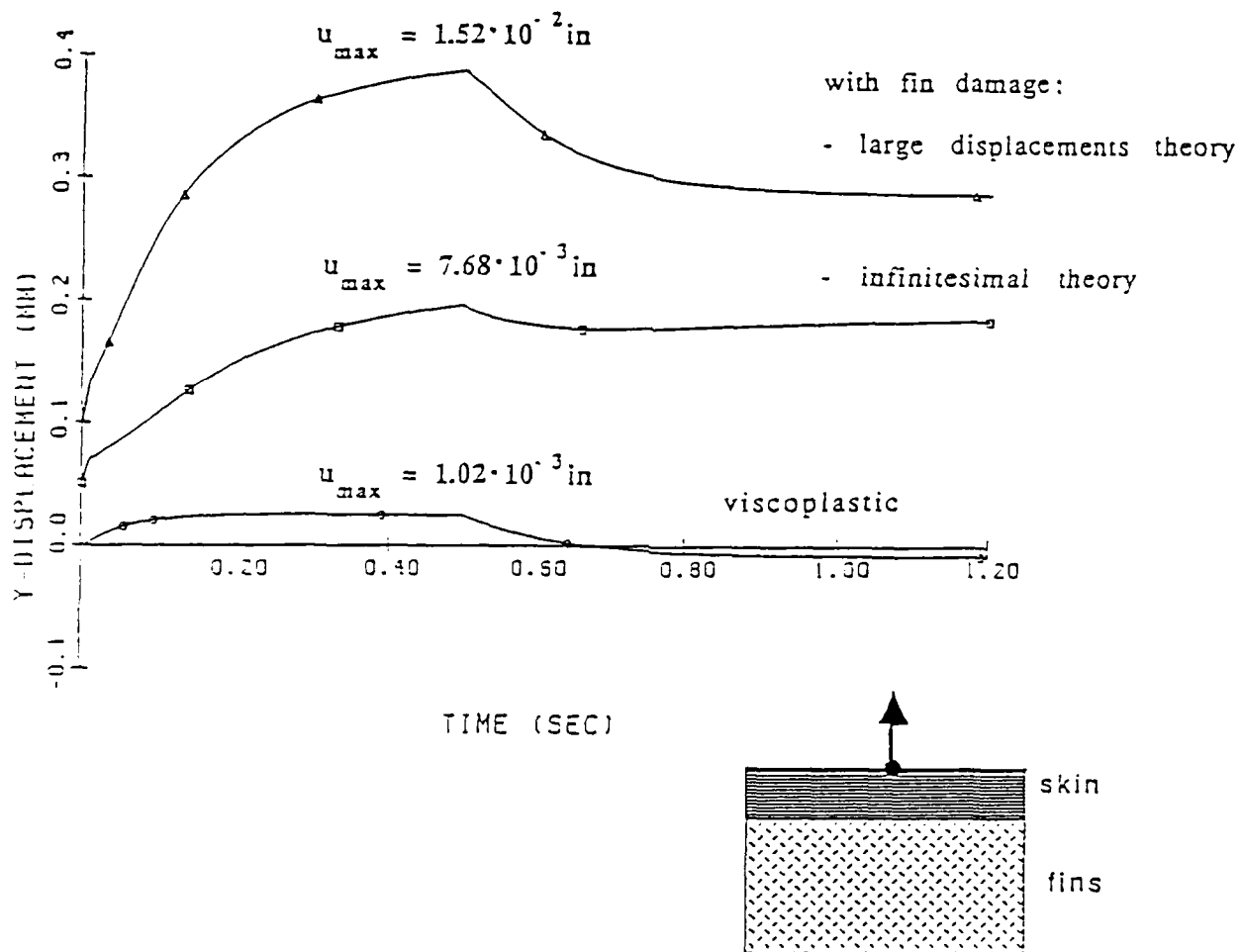
104

Figure 48: Viscoplastic deformation of aerodynamic skin for undamaged and damaged heat exchanger fins.